Deceleration Stage Rayleigh-Taylor Instability Growth in Inertial Confinement Fusion Relevant Configurations

Camille C. Samulski

Thesis submitted to the Faculty of the

Virginia Polytechnic Institute and State University

in partial fulfillment of the requirements for the degree of

Master of Science

in

Aerospace Engineering

Bhuvana Srinivasan, Chair

Colin Adams

Stefano Brizzolara

May 10, 2021

Blacksburg, Virginia

Keywords: Rayleigh-Taylor instability, seeded magnetic field, laser-driven implosion, inertial confinement fusion, Omega, NIF

Deceleration Stage Rayleigh-Taylor Instability Growth in Inertial Confinement Fusion Relevant Configurations

Camille C. Samulski

(ABSTRACT)

Experimental results and simulations of imploding fusion concepts have identified the Rayleigh-Taylor (RT) instability as one of the largest inhibitors to achieving fusion. Understanding the origin and development of the RT instability will allow for the development of mitigating measures to dampen the instability growth, thus improving the chance that fusion concepts such as inertial confinement fusion (ICF) are successful. A study of 1D and 2D simulations are presented for investigating RT instability growth in deceleration stage of imploding geometries. Two cases of laser-driven implosion geometry, Cartesian and cylindrical, are used to study late stage deceleration-phase RT instability development on the interior surface of imploding targets. FLASH's hydrodynamic (HD) and magnetohydrodynamic (MHD) modeling capabilities are used for different laser and target parameters in order to study the RT instability and the impact of externally applied magnetic fields on their evolution. Several simulation regimes have been identified that provide novel insight into the impact that a seeded magnetic field can have on RT instability growth and the conditions under which magnetic field stabilization of the RT instability is observable. Finally, future work and recommendations are made.

Deceleration Stage Rayleigh-Taylor Instability Growth in Inertial Confinement Fusion Relevant Configurations

Camille C. Samulski

(GENERAL AUDIENCE ABSTRACT)

The direction for the future of renewable energy is uncertain at this time; however, it is known that the future of human energy consumption must be green in order to be sustainable. Fusion energy presents an opportunity for an unlimited clean renewable energy source that has yet to be realized. Fusion is achieved only by overcoming the earthly limitations presented by trying to replicate conditions at the interior of stellar structures. The pressures, temperature, and densities seen in the interior of stars are not easily reproduced, and thus human technology must be developed to reach these difficult stellar conditions in order to harvest fusion energy. There are two main branches of developmental technology geared towards achieving the difficult conditions controlled nuclear fusion presents, magnetic confinement fusion (MCF) and inertial confinement fusion (ICF)[17]. Yet in both approaches barriers exist which have thwarted the efforts toward reaching fusion ignition which must be addressed through scientific discovery. Successfully reaching ignition is only the first step in the ultimate pursuit of a self sustaining fusion reactor. This work will focus on the experimental ICF configuration, and on one such inhibitor toward achieving ignition, the Rayleigh-Taylor (RT) instability. The RT instability develops on the surfaces of the fusion fuel capsules, targets, and causes nonuniform compression of the target. This nonuniform compression of the target leads to lower pressures and densities through the material mixing of fusion fuel and the capsule shell, which ultimately leads to challenges with reaching fusion ignition. The work presented here was performed utilizing the University of Chicago's FLASH code,

which is a state-of-the-art open source radiation magneto-hydrodynamic (MHD) code used for plasma and astrophysics computational modeling [11]. Simulations of the RT instability are performed using FLASH in planar and cylindrical geometries to explore fundamental Rayleigh-Taylor instability evolution for these two different geometries. These geometries provide easier access for experimental diagnostics to probe RT dynamics. Additionally, the impact of externally applied magnetic fields are explored in an effort to examine if and how the detrimental instability can be controlled.

Dedication

To family and my uncles Eddie and Richard.

Acknowledgments

I would like to acknowledge the support, advice, and encouragement I have received from many people during the course of this research. First, I would like to thank my advisor Professor Bhuvana Srinivasan, for her continued support, advice, and guidance in my research. I would also like to thank the members of my committee, Professor Colin Adams and Professor Stefano Brizzolara for their valuable time and feedback. I have received wonderful support from General Atomics, specifically from Dr. Mario Manuel, whose patient guidance and advice made this research possible. I would also like to thank the members of my research group, Dr. Petr Caga, Dr. Chirag Rathod, Matt Carrier, Kolter Bradshaw, and John Rodman for their revisions of this thesis. In particular I'd like to thank Robert Masti and Megan McCracken for their friendship, their feedback on this thesis, and their continued help and support working through research problems over the years. I would also like to thank my parents, Joe Samulski and Cynthia Hammond, for their support through the entirety of my academic pursuits. Finally, I would like to thank my husband, Haiwen Zhang, for his patience, love, and unwavering support as I continue my research.

This work is supported by Los Alamos National Laboratory under subcontract 463281 and US Department of Energy grant SC0020055. I would like to also acknowledge Advanced Research Computing at Virginia Tech for providing computational resources and technical support, and the FLASH Center for Computational Science for there constant feedback and access to the FLASH code developed by the DOE NNSA-ASC OASCR Flash Center at the University of Chicago

Contents

List of Figures

Chapter 1

Introduction

1.1 Background

It is increasingly evident that there is a need for a sustainable green energy source for the future progress of humanity and one such form of energy is fusion based. The realization of fusion energy would mean a source of large scale energy production without the radioactive waste found in a nuclear fission reactor. This would give way to a platform of realized sustainable green energy to power humanity going forward. The ability to achieve a fusion reaction on Earth has been proven in instances such as the hydrogen-bomb, however, those are single instance fusion reactions that do not lead to a controllable reaction that would produce usable power for consumption. In order for a fusion reaction to be a sustainable green energy option, a fusion reactor will need to be developed that will take a provided fuel source and reach ignition. Fusion occurs naturally in the interiors of stellar structures, and since we do not have stellar conditions naturally occurring on Earth, so reaching safe and sustainable ignition is a significant feat.

Two approaches have been born of the attempts at replicating the required conditions for fusion on Earth, magnetic confinement fusion (MCF) and inertial confinement fusion (ICF). MCF proposes the use of magnetic fields to confine hot ionized plasma. One such configuration is toroidal and commonly called a tokamak. The ICF approach involves reaching extremely high density plasma, on the order of $10 \times 10^{25}\,\mathrm{cm}^{-3}$, to achieve the necessary

probability for fusion reaction collisions. These high densities are achieved by compressing fusion fuel over very short time scales, on the order of $\leq 10 \times 10^{-10}$ s [17]. Both these confinement fusion concepts require the fusion fuel to be in the plasma state. Plasma is the fourth state of matter consisting of ions and electrons in a quasi-neutral state, and whose motion is dependant on local and remote plasma conditions [6]. One common application of the ICF approach is through the compression of small spherical or cylindrical capsules filled with deuterium-tritium (D-T) gas as the fuel source [17]. These capsules are then compressed through irradiation of their surfaces by either direct drive or indirect drive lasers. This thesis is primarily focused on the direct laser driven ICF concept. In the direct drive methodology, a capsule is hit directly by a brief laser pulse on the order of 1 to 3 ns. This triggers an implosion of the capsule which heats and compresses the D-T fuel.

Experiments have shown disruption of the implosion symmetry, spherical or cylindrical, which can inhibit the chances of the D-T fuel being effectively heated and confined to reach ignition [4, 7, 8, 16]. Thus, it has been demonstrated that the presence of a seed magnetic field in an ICF capsule can relax the ignition criterion due to enhanced confinement time and reduction of thermal conduction away from the hot-spot [16]. Experiments first conducted at Omega [28] demonstrated an increase in the ion temperature and neutron yield by 15% and 30%, respectively. These findings sparked the development of new platforms at the National Ignition Facility to study these performance enhancements. However, the presence of instabilities during ICF implosions still present hurdles to achieving fusion ignition. One of the largest inhibitors of the implosion symmetry is the Rayleigh-Taylor (RT) instability, which grows when a light fluid supports a heavy fluid under the influence of an acceleration and a perturbation is applied to the interface between the fluids. Therefore, seeded magnetic fields could have the benefit of potentially stabilizing RT instability growth during implosion, thus relaxing ignition criteria. The work presented here will focus on the RT instability

growth during the deceleration stage of laser driven capsules. The primary focus will be on the classical sinusoidal perturbation as well as preliminary results on the thin-layer-theory of RT instability growth. The parameters used here to model the capsules were adapted from existing experiments on the Omega laser at the Laboratory for Laser Energetics and at the National Ignition Facility (NIF).

1.2 Rayleigh Taylor Instability

The RT instability is commonly understood via the classical description of two fluids with differing densities (ρ_1 and ρ_2, where $\rho_2 > \rho_1$) subject to a constant acceleration (g) opposing the density gradient. A perturbation of the densities with wave number k ($k = 2\pi/\lambda$) results in a RT instability growth rate of $\gamma_c^2 = gkA_t$, where $A_t = (\rho_2 - \rho_1)/(\rho_2 + \rho_1)$ is the Atwood number, and subsequently in the presence of tangential magnetic fields, the growth rate becomes [5, 13]

$$\gamma_B^2 = gkA_t - \frac{2B^2k^2cos^2\theta}{(\rho_2 - \rho_1)} \tag{1.1}$$

where θ is the angle between the magnetic field and the wave vector $\mathbf{k}$. The immediate impact of the magnetic field on the RT instability is seen in that there is a critical wavelength, $\lambda_c = \frac{B^2cos^2\theta}{g(\rho_2-\rho_1)}$, such that perturbations with a wavelength smaller than λ_c are stabilized. Experiments exploring the mitigating impact of magnetic fields on RT instability spike morphology are commonly focused on identifying the λ_c and observing the impact on wavelengths shorter than λ_c.

The classical form of the RT instability is commonly associated with ablative and exterior features of ICF implosions, however the RT instability does have the potential to occur on the interior face of a capsule during the deceleration phase of an ICF implosion. The initial laser-driver sets in motion the implosion of an ICF capsule, but the fuel, as it compresses, reaches

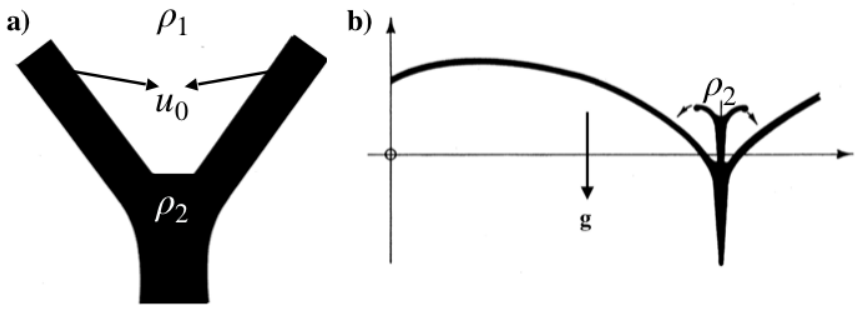

Figure 1.1: Reproduction of figures from Ott [9] demonstrating a) the collapse of the high density walls of an isolated feature in a thin layer of high density, and b) the resultant RT instability growth from the inward motion of the high density material.

high enough pressure to force the implosion to decelerate. At this point of deceleration, the high density capsule liner is propagating inwards towards the low density target, thus setting up a second RT unstable surface at the interior of the capsule. This RT unstable surface provides another opportunity for the implosion to be disrupted and presents a second situation in which the RT instability needs to be dampened in order to achieve uniform convergence and reduced mixing for ignition.

The RT instability is also theorized to rapidly develop non-linearly in the configuration of a thin layer of high density material supported by a thicker low density material [9]. The presence of a small perturbation that has a wavelength longer than the thickness of the high density layer (an isolated feature) can be seen dominating instability growth at later times. Figure 1.1a shows how the isolated feature perturbation will develop as the fluid layers of ρ_2 collide. This subsequently forms a downward vertical layer, that falls under the influence of gravity, and an upward jet of fluid, which will splay outward before also falling back down under the gravitational influence, illustrated in Figure 1.1b.

Magnetic fields are predicted to impact RT instability morphology during nonlinear evolution. Thus, given the nonlinear nature of the thin-layer-theory RT instability evolution and the classical RT instability, the potential mitigating impacts of an applied magnetic

field may arise. The required magnetic field to achieve noticeable impacts in a high energy density (HED) system would be upwards of ∼100T, which is a field strength that is potentially reached via the amplification of seeded magnetic fields in local regions of plasma [16]. The impact of such locally amplified fields can be seen in the reduction of Kelvin-Helmholtz (KH) vortices and subsequent mixing of materials. The study of magnetic field effects on RT instability growth and KH has been numerically investigated in a 2D geometry by Srinivasan and Tang [23], which explored a multimode perturbation in an ICF-relevant regime, see Figure 4.1.

The magnetic field suppresses short-wavelength modes and secondary KH growth when the field is parallel to the perturbation wave vector. However, there is little impact on instability growth in 2D simulations when the field is out of this plane. Additional numerical studies, like the ones found in Perkins [16], have studied the impact magnetic fields have on seeded instabilities of ICF capsules during deceleration. This study also predicts effective mitigation of short-wavelength RT instability growth and the relaxation of ignition criteria for ICF. Experimental studies are only now beginning to validate these numerical predictions, all in the context of a wavelength that is short compared to the dense layer thickness.

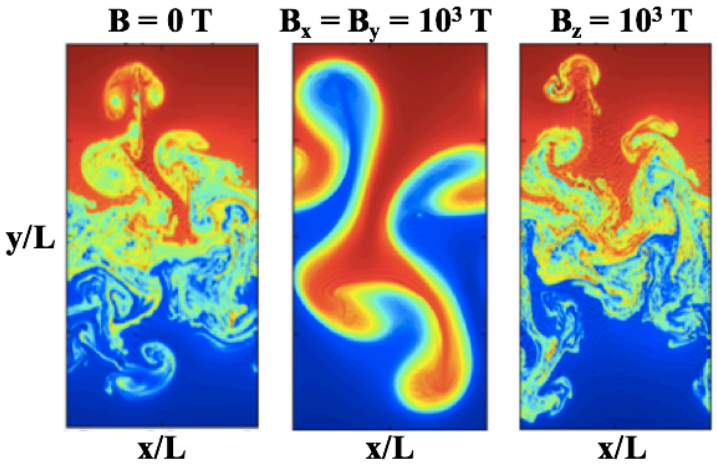

Figure 1.2: Reproduction figure of mass density plots from Srinivasan and Tang [23] demonstrating the effects of background B-fields on late-time RT growth in three different B-fields configurations.

The use of magnetic fields in ICF is of great interest, and identifying the best methods to model impacts from seeded background magnetic fields is necessary to understand the anticipated effects and design experiments [16, 23]. The primary experimental model for cylindrical and Cartesian direct drive setups is one of a solid density shell or pusher and a target foam of varying densities. With the current NIF and Omega capabilities of reaching seeded background magnetic fields of approximately 30 T, a solid density cylindrical configuration and a foam NIF scale Cartesian configuration are studied with comparable seeded magnetic fields. The simulations demonstrated the predicted stabilizing effect that a seeded magnetic field would have on RT instability growth. Achieving a sufficiently large magnetic Reynolds numbers, the ratio of induction to diffusion, requires sufficient temperatures and sustained velocities that are difficult to achieve during the HED implosions studied here. The standard model of using Spitzer resistivity[22] for an HED implosion requires that the resistivity be sufficiently small such that the diffusive effects are limited. Due to the fact that Spitzer resistivity has an inverse temperature dependence, achieving sufficiently large plasma temperatures is necessary for a magnetized HED implosion [22]. Here we explore a series of simulations in Cartesian and cylindrical coordinates that demonstrate a measurable deceleration stage RT instability growth.

1.3 Modeling in FLASH

FLASH is a multi-physics radiation-hydrodynamics code developed by the University of Chicago, which utilizes an Eulerian representation of the fluid [11]. An Eulerian representation involves the use of a stationary spatial mesh which allows for fluid to move into and out of a cell. Unlike in a Lagrangian code, where the mesh moves with the fluid, an Eulerian code has the advantage of avoiding mesh entanglement, where presence of complex fluid

vortex-like structures could produce extensive mesh deformation. Additionally, FLASH has adaptive mesh refinement (AMR) capabilities. This means that the mesh consists of individual blocks which can be broken down further into smaller blocks, providing better resolution in desired regions of the domain. The refinement can be triggered by a chosen variable, such as temperature or density, meaning a change in density in the domain would trigger the mesh to refine in order to capture the fluid features developing in that region.

The HED configurations presented in this thesis have been modeled with the Euler equations, the ideal-MHD equations, and the resistive-MHD equations using FLASH. FLASH solves the Euler equations which are [1]

$$\frac{\partial \rho}{\partial t} + \nabla \cdot [\rho \mathbf{u}] = 0, \tag{1.2}$$

$$\frac{\partial \rho \mathbf{u}}{\partial t} + \nabla \cdot (\rho \mathbf{u}\mathbf{u}) + \nabla P = \rho \mathbf{g}, \tag{1.3}$$

$$\frac{\partial \rho E}{\partial t} + \nabla \cdot \big((\rho E + P)\, \mathbf{u} \big) = \rho \mathbf{u} \cdot \mathbf{g}, \tag{1.4}$$

where ρ, $\mathbf{u}$, and P are the fluid density, velocity, and pressure respectively, and E is the internal energy, $\mathbf{g}$ is acceleration, and t is the time coordinate. For the MHD systems FLASH solves the dimensionless MHD equations as follows [1],

$$\frac{\partial \rho}{\partial t} + \nabla \cdot (\rho \mathbf{u}) = 0, \tag{1.5}$$

$$\frac{\partial \rho \mathbf{u}}{\partial t} + \nabla \cdot \big(\rho \mathbf{u}\mathbf{u} - \mathbf{B}\mathbf{B} \big) + \nabla p_* = \rho \mathbf{g} \tag{1.6}$$

$$\frac{\partial \rho E}{\partial t} + \nabla \cdot \big(\mathbf{u}\,(\rho E + p_*) - \mathbf{B}\,(\mathbf{u} \cdot \mathbf{B}) \big) = \rho \mathbf{g} \cdot \mathbf{u} + \nabla \cdot (\sigma \nabla T) + \nabla \cdot \big(\mathbf{B} \times (\eta \nabla \times \mathbf{B}) \big), \tag{1.7}$$

and

$$\frac{\partial \mathbf{B}}{\partial t} + \nabla \cdot (\mathbf{uB} - \mathbf{Bu}) = -\nabla \times (\eta \nabla \times \mathbf{B}), \tag{1.8}$$

where,

$$p_* = p + \frac{B^2}{2}, \tag{1.9}$$

$$E = \frac{1}{2}\mathbf{u}^2 + \epsilon + \frac{1}{2}\frac{B^2}{\rho}, \tag{1.10}$$

T is the temperature, the magnetic field is given by $\mathbf{B}$, $\mathbf{g}$ is the acceleration, μ is the dynamic viscosity, $\mathbf{I}$ is the identity tensor, p is the thermal pressure, σ is the heat conductivity, and η is the resistivity. FLASH uses tabulated equation-of-state (EOS) to close the system, in the form of tables that are denoted using the terminology of ionmix tables. For the ideal-MHD cases the diffusive effects of resistivity are neglected in equation 1.8. In all equation systems the internal energy, E, is calculated separately in FLASH using,

$$\frac{\partial \rho E}{\partial t} + \nabla \cdot ((\rho E + P)\,\mathbf{u}) - \mathbf{u} \cdot \nabla P = 0. \tag{1.11}$$

The term on the right-hand-side of Eq.(1.8) is the resistive-MHD terms, which has been useful for explaining experimentally observed phenomena [21]. Lastly, FLASH includes radiative transfer through the following,

$$\frac{1}{c}\frac{\partial I}{\partial t} + \hat{\mathbf{\Omega}} \cdot \nabla I + \rho \kappa I = \eta \tag{1.12}$$

where $I(\mathbf{x}, \hat{\mathbf{\Omega}}, \nu, t)$ is the radiation intensity, c is the speed of light, ρ is the mass density, $\kappa(\mathbf{x}, \nu, t)$ is the opacity, $\eta(\mathbf{x}, \nu, t)$ is the emissivity, ν is the radiation frequency, and $\hat{\mathbf{\Omega}}$ is the unit direction vector. This equation is coupled within FLASH to the electron internal energy. The MHD equations are critical to simulating magnetized phenomenon accurately

within the limitations of their assumptions. The ideal-MHD cases presented ignore diffusive effects, thus providing a regime of maximum background magnetic field amplification and its effect on RT instability growth. The resistive-MHD cases presented utilize FLASH's Spitzer anisotropic resistivity formulation,

$$\eta_{perp} = \frac{m_{ele}}{e^2 n_{ele} \tau_{ele}} \tag{1.13}$$

$$\eta_{par} = \frac{\eta_{perp}}{1.96} \tag{1.14}$$

where m_{ele}, e, n_{ele}, and τ_{ele} are mass, charge, number density and collision time of the electrons respectively. η_{perp} and η_{par} represent the resistivity perpendicular and parallel to the magnetic field. All three equation systems are solved using user designated specified Riemann solvers, orders, and other hydrodynamic solver parameters. The Riemann solver designates which method FLASH will use to calculate the flux across discontinuities in the domain; Harten-Lax-van Leer-Contact (HLLC), which restores the shear wave and contact surface [25], is used for the simulations presented. The simulations performed here use a second order accurate MUSCL-Hancock algorithm in FLASH [26, 27].

An example FLASH input file, referred to as a par file, for a Cartesian ideal-MHD case can be found in Appendix A.1, from which the purely Euler case, called hydrodynamic (HD) going forward, can be created by setting the magnetic field to zero. The par file consists of plotting parameters, like output frequency and variables, the aforementioned HD parameters (Riemann solver, cfl, etc.), domain boundary conditions (like reflecting or outflow), the MHD parameters (like resistivity, time-step limitations), conduction requirements (like diffusion boundary conditions and diffusion time step limitations), EOS designations (assigning EOS table for materials in the domain), mesh parameters (i.e, number of cells and refinement level), radiation and opacity designation for simulated materials (like multigroup radiation),

and initial conditions and laser parameters. The resistive-MHD par file can be located in Appendix A.2, where the distinctive flags for resistivity and diffusion are applied in the MHD and "Time parameters" sections.

FLASH has extensive laser modeling capabilities which allow for many different laser configurations to be modeled. The configurations presented utilize a single laser beam with one pulse, meaning the laser is "on" only once for a length of time between 1 and 3 ns depending on the experimental requirements. The laser is comprised of a number of individual rays arranged within a beam in a chosen configuration, "statistical1D" chosen for 2D beams to ensure uniform distribution. This "statistical1D" designation ensures that the individual rays are distributed uniformly throughout the laser regardless of dimension or coordinate system. Modeling the effect of a 3D laser in 1D or 2D cylindrical or Cartesian coordinate systems requires scaling factors for the laser power. Conveniently, FLASH has an conversion parameter "ed_adjustBeamsTargetIntensity" which internally converts the 3D cylindrical laser power to either 1D or 2D Cartesian equivalent laser powers. However for 1D cylindrical laser powers a manual adjustment of [1],

$$P_{1D}^{cyl} = 2\pi r_t I_l, \tag{1.15}$$

where P_{1D}^{cyl} is the adjusted 1D cylindrical laser power in W/cm, r_t is the radial position of the target, and I_l is the laser intensity in W/cm^2. This power adjustment is crucial in ensuring simulations of the same experimental configuration are modeled accurately in 1D HD and MHD, as well as in 2D HD and MHD regimes.

1.4 Work Presented

Computational models using the cylindrical coordinates in FLASH to more accurately represent a cylindrical laser-driven HED implosion are initially explored. These simulations are performed in radial 1D HD and ideal-MHD first to benchmark with existing non-magnetized cylindrical experimental data [18]. Next, the same setup is expanded to 2D, where significant RT instability growth has been shown to develop on the interior of an HED experimental capsule during the deceleration stage. The addition of a background magnetic field is studied in ideal-MHD and resistive-MHD in an effort to demonstrate whether the addition of a magnetic field could push ICF experiments one step closer to surmounting the RT instability and reaching ignition. These results are discussed in Chapter 2 at length.

A series of simulations are performed for Omega and NIF targets that were shot in 2020 and 2021. These targets are designed to study the growth and potential stabilization of RT instabilities seeded with a sinusoidal perturbation in a blast wave configuration, meaning a rectangular target driven by a laser incident on one face of the rectangle. Consequently, these simulations are performed in a Cartesian coordinate system. These simulations and some comparative experimental data are presented Chapter 3, providing results for ideal-MHD and resistive-MHD cases.

Chapter 4 presents an initial exploration into the growth of the RT instability under thin-layer-theory conditions. These simulations serve as preliminary designs for future 2021 NIF shots and anticipated Omega experiments. A discussion on the potential effects of hot electrons on RT instability morphology is tentatively explored under the preliminary setup conditions. Lastly, Chapter 5 provides a summary of the results from the cylindrical, Cartesian, and single-feature models presented. Additionally, a recommendation by the author on the future work and development is presented. The work the author has completed thus far

provides grounds for additional research into the mitigating impacts of background magnetic fields on RT instability growth in HED experiments.

Chapter 2

Cylindrical Compression Rayleigh Taylor Growth

This chapter addresses a series of simulations performed to validate and extend upon a preexisting configuration developed using Los Alamos National Laboratory's X-Rage Hydro code [12]. The configuration is one of a cylinder that is driven inwards by a laser pulse, where an artificially manufactured perturbation is on the interior face of the annulus. This configuration is modeled in HD on X-Rage without any added magnetic fields. In this work, FLASH simulations are used for any simulations involving a seed magnetic field for ideal-MHD and the addition of diffusive effects in resistive-MHD. The X-Rage configuration described in this chapter is designed with the intent to study non-magnetized experimental results on the Omega laser. The Omega laser and Omega-EP laser represent the two primary research lasers available at the Laboratory for Laser Energetics (LLE) at the University of Rochester. Omega has been operational since 1995 and comprises of 60 beams able to focus 40 000 J onto a 1 mm spot within a billionth of a second [2]. The Omega-EP laser has been operational since 2008 and is designed with the National Ignition Facility (NIF) architecture as its foundation, with 4 beams and picosecond operation times [2]. These experimental parameters applied to the following cylindrical configuration are chosen because they provide the potential for simulating deceleration stage RT instability growth and applied seed magnetic fields.

2.1 Experimental Parameters and 1D Validation

The conditions used for our cylindrical simulations are derived from the aforementioned Omega laser experiments. In particular, the configuration for the simulations consisted of a 51 μm CH ablator at 1.25 g/cm^3, an interior 12 μm aluminum marker at 2.7 g/cm^3, and a 430 μm radial CH target foam at 0.3 g/cm^3 [19]. Using a laser drive of 18 kJ over 3 ns, 2D FLASH simulations are verified against existing X-Rage and experimental data from Omega shots [20]. The laser incident on the target package surface heats the material causing a shock front which compresses and heats the target foam. Figure 2.1 represents a non-magnetized measure of the radial position of the shock as function of time. FLASH data is shown with the blue dashed line and X-Rage with the solid red line. The experimental data is analyzed with a Bayesian Inference Engine (BIE) approach [24] and shown the green squares, and raw experimental measurements are shown in the purple diamonds. Across both X-Rage and FLASH results and the different interpretations of the raw experimental data, there is general uniformity in the shock propagation of the imploding cylinder. The minor differences between them are likely due to different algorithmic choices in the simulation such as shock resolution from the use of AMR. FLASH and X-Rage stand in agreement with the comparable experimental data.

The cylindrical parameters from the verification are then adjusted for a new deceleration stage RT unstable configuration derived from Sauppe et al. [18], where the target foam is dropped to 0.06 g/cm^3 and the laser drive is dropped to 8 kJ [18], a schematic of this configuration can be seen in Figure 2.3. A measure of the shock location as a as a function of time for each of the simulations corresponding to 1D HD, 2D HD, 2D ideal-MHD, and 2D resistive-MHD is presented in Figure 2.2. The implosion location is chosen because it ensures consistency across both 1D and the 2D HD and MHD schemes for this configuration. Since the implosion dynamics agree between the 1D and the unperturbed 2D simulations, the next

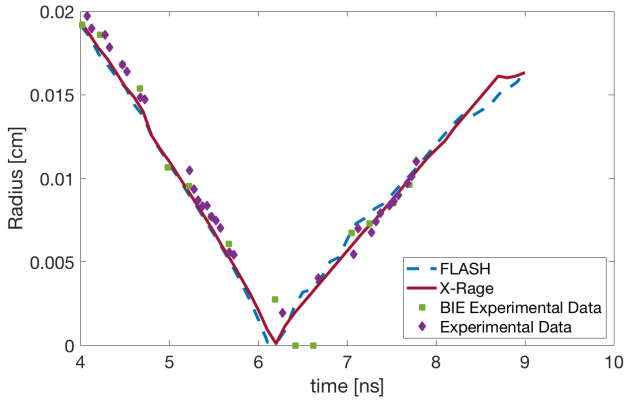

Figure 2.1: FLASH simulation benchmarked against X-Rage data and experimental data for the configuration with a target foam of $0.3\,\mathrm{g/cm^3}$. The FLASH data is represented by the blue dashed line, while the X-Rage data is the red line. The purple markers are derived from experimental data analyzed by hand, while the green square markers are the same experimental data analyzed through a BIE approach [20].

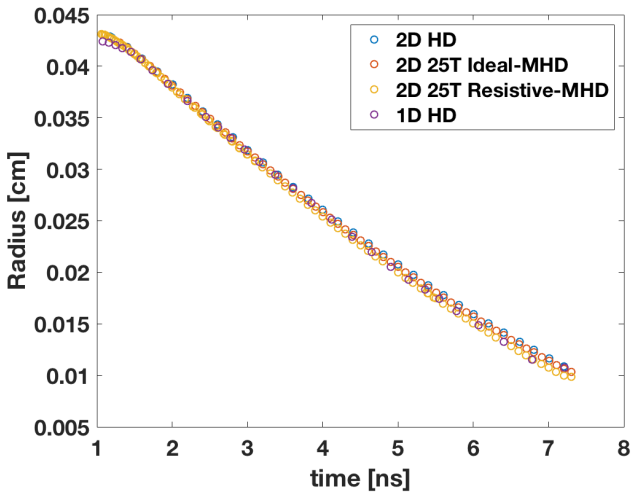

Figure 2.2: A measure of interior implosion as a function of time and radius of FLASH simulations in 1D and 2D geometry. They are benchmarked against each other to demonstrate a change in dimension from 1D HD, in purple, and 2D HD, in blue, does not impact the convergence. Also, the transition to 2D MHD, both ideal, in red, and resistive, in yellow, does not impact the convergence.

step is to include a perturbation which is required for RT growth. The perturbation used in modeling has a wavelength of $40\,\mu$m with an amplitude of $5\,\mu$m along the interface between the foam target and aluminum marker. Since FLASH is verified in this configuration, we

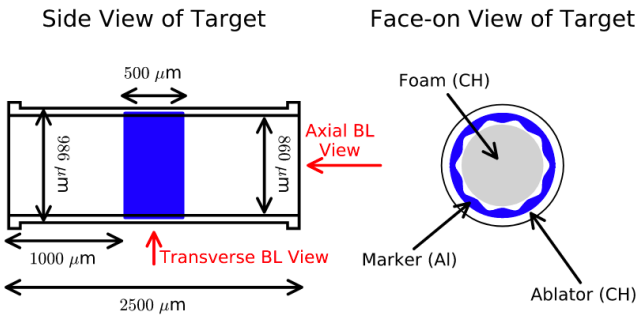

Figure 2.3: A reproduction of the cylindrical target from Sauppe et al. 2020 [18]. The dimensions of the target a given and the position of the aluminum marker interior to the solid density CH, and the presence of the perturbation between the solid density liner and interior foam.

wanted to extend the simulations to study the impact a seeded magnetic field would have on RT growth. The simulations that follow use the 2D cylindrical FLASH capabilities to solve the HD, ideal-MHD, and resistive-MHD equation sets. The seeded background magnetic field for the MHD cases oriented parallel to the perturbation are of magnitude 10 T, 25 T, and 50 T.

2.2 Single Mode Sinusoidal Perturbation

Distinct RT instability growth is on the interior surface of the implosion during deceleration, seen in Figure 2.4. The peak initial magnetic field experimentally achievable on NIF and Omega is on the order 30 T at this time. In order to investigate the range of presently achievable and future achievable magnetic fields, a solid density liner is simulated with a range of seeded magnetic fields, that spanned 10 T, 25 T, and 50 T. Using these magnetic fields, the simulations investigate the impact presently achievable seeded magnetic fields would have on RT instability growth, seen in Figures 2.5, 2.6, and 2.7. Figure 2.8 illustrates this solid density liner configuration modeled in a HD, ideal-MHD, and resistive-MHD regime

at 5.4 ns into the implosion. These density plots show that, as predicted from Equation 1.1, a larger seeded background field of 50 T has a greater impact on RT instability morphology and growth in an ideal-MHD scheme because of the smaller growth rate when compared to simulations with smaller magnetic fields. The ideal-MHD simulation at 10 T has minimal differing morphology when compared to the HD, while the 25 T case illustrates the RT instability bubble morphology being diminished. Lastly, the 50 T case displays a complete mitigation of bubble morphology with the interface nearly remaining intact.

When comparing the resistive-MHD and the ideal-MHD simulations, the ideal-MHD simulation shows a more clear reduction in RT growth and morphology. This distinction in the reduction of RT growth is because the diffusion in the resistive-MHD nearly eliminates the mitigating impact that the seeded magnetic fields have on the RT instability growth. In the resistive-MHD simulations, the addition of the diffusive effects from resistivity in Equation 1.8 reduces the magnetic field growth during the implosion, producing an insignificant impact of resistivity on the RT instability growth. In an ideal plasma, the magnetic field is inherently tied to the motion of the plasma, so as the plasma deforms the magnetic field follows suit, resulting in the accumulation of magnetic field at the interface. This accumulation of the magnetic field at the interface acts like a surface tension limiting the growth of this instability. Adding resistivity removes allows the plasma to move without the magnetic field resulting in a smaller accumulation of magnetic field at the interface. As a result, the magnetic field is not as effective at mitigating growth as compared to the ideal-MHD simulations.

In the resistive scheme, the presently achievable magnetic field strengths have little impact on the RT instability growth. This can clearly be seen in Figure 2.9 which presents an estimate of the RT instability growth by measuring the distance between the peak of the RT instability bubble to the valley of the RT instability spike growing over the course of the

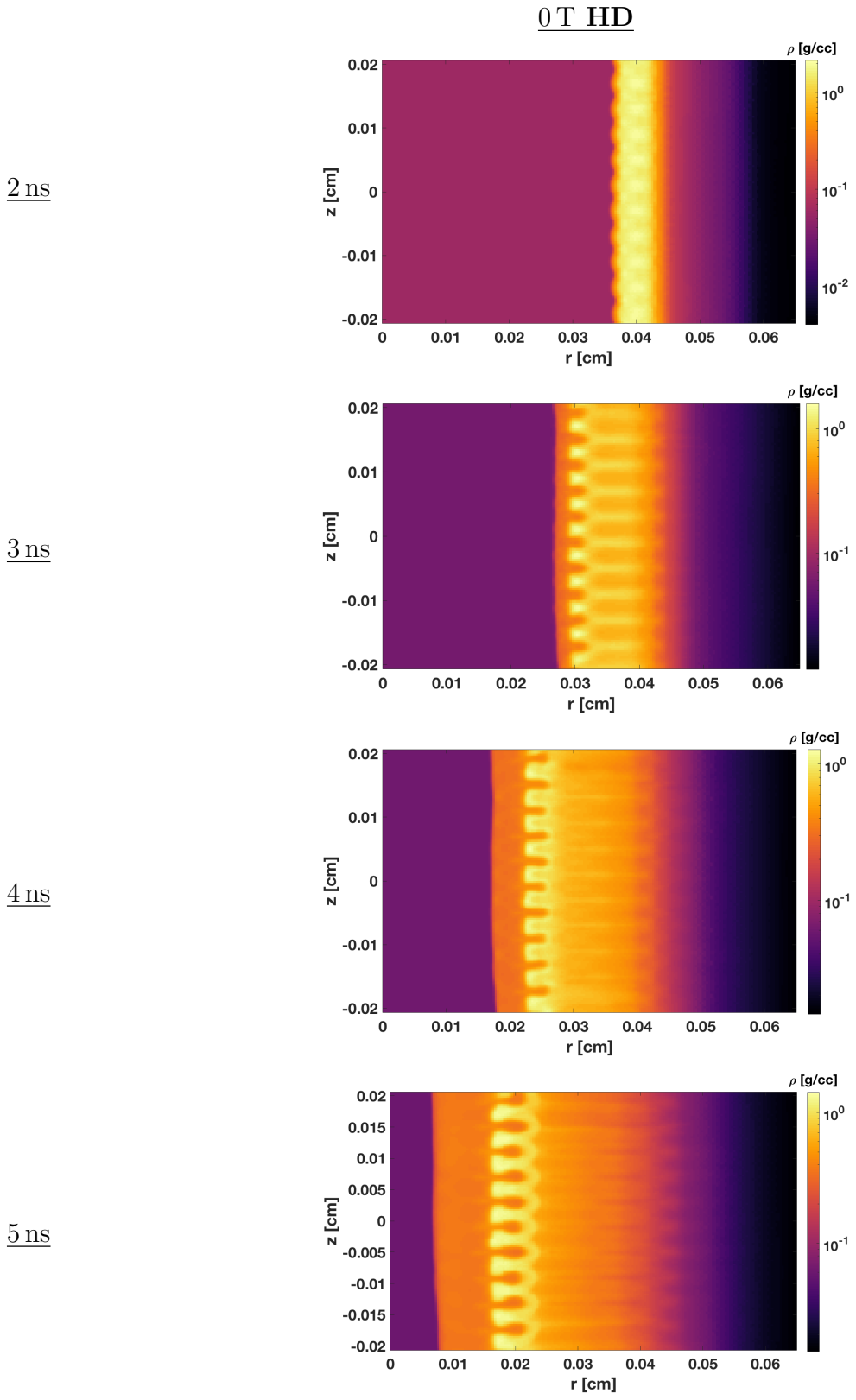

Figure 2.4: Density plots at 2 ns, 3 ns, 4 ns, and 5 ns of the RT instability growth during deceleration, modeled in HD both without a background fields. The RT instability growth is shown to develop prominently on the interior of the solid density shell.

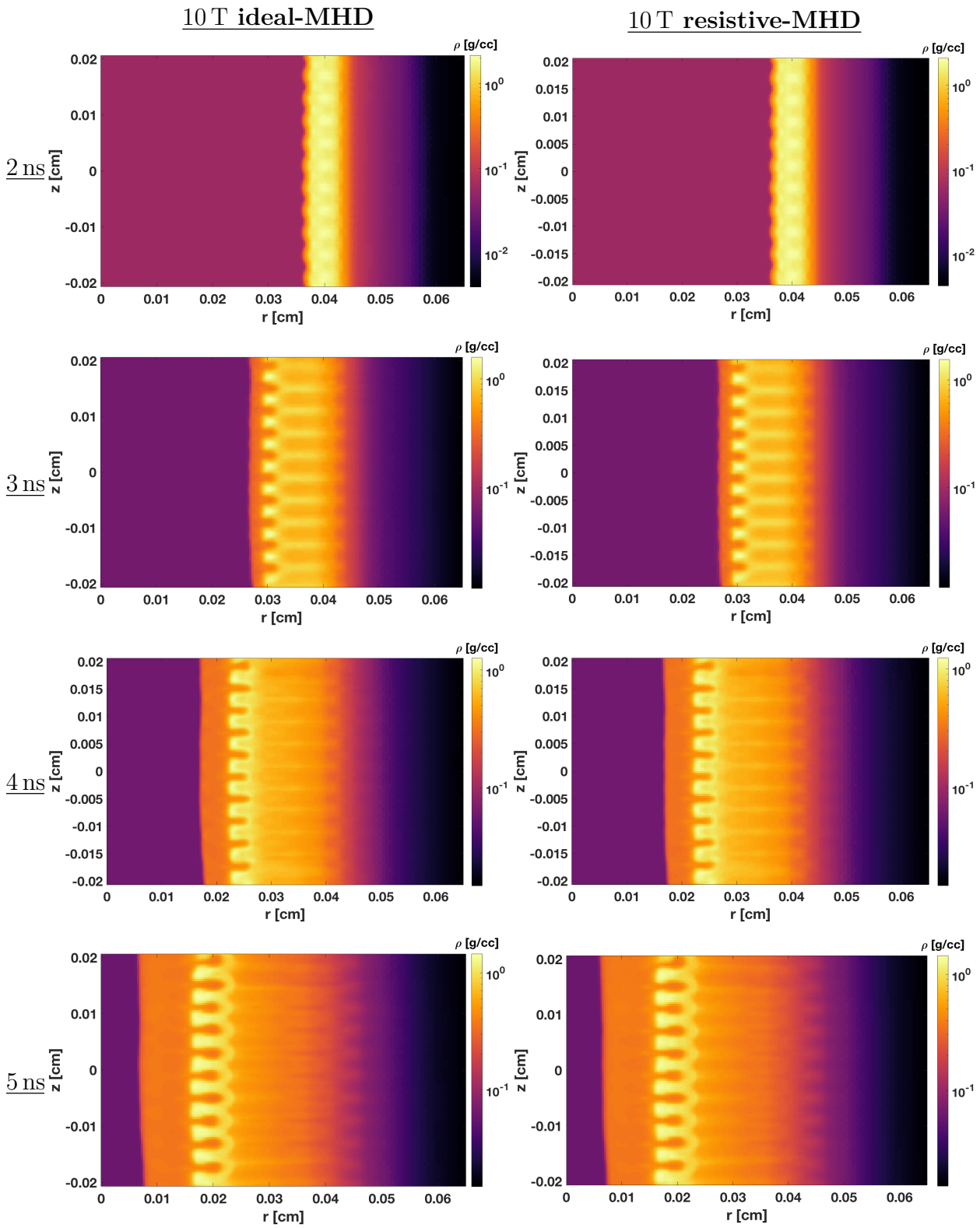

Figure 2.5: Density plots at 2 ns, 3 ns, 4 ns, and 5 ns of the RT instability growth during deceleration, modeled in ideal-MHD and resistive MHD both with a 10 T background fields. The damping impact of the magnetic field is not obviously seen in the ideal-MHD morphology or the resistive-MHD cases.

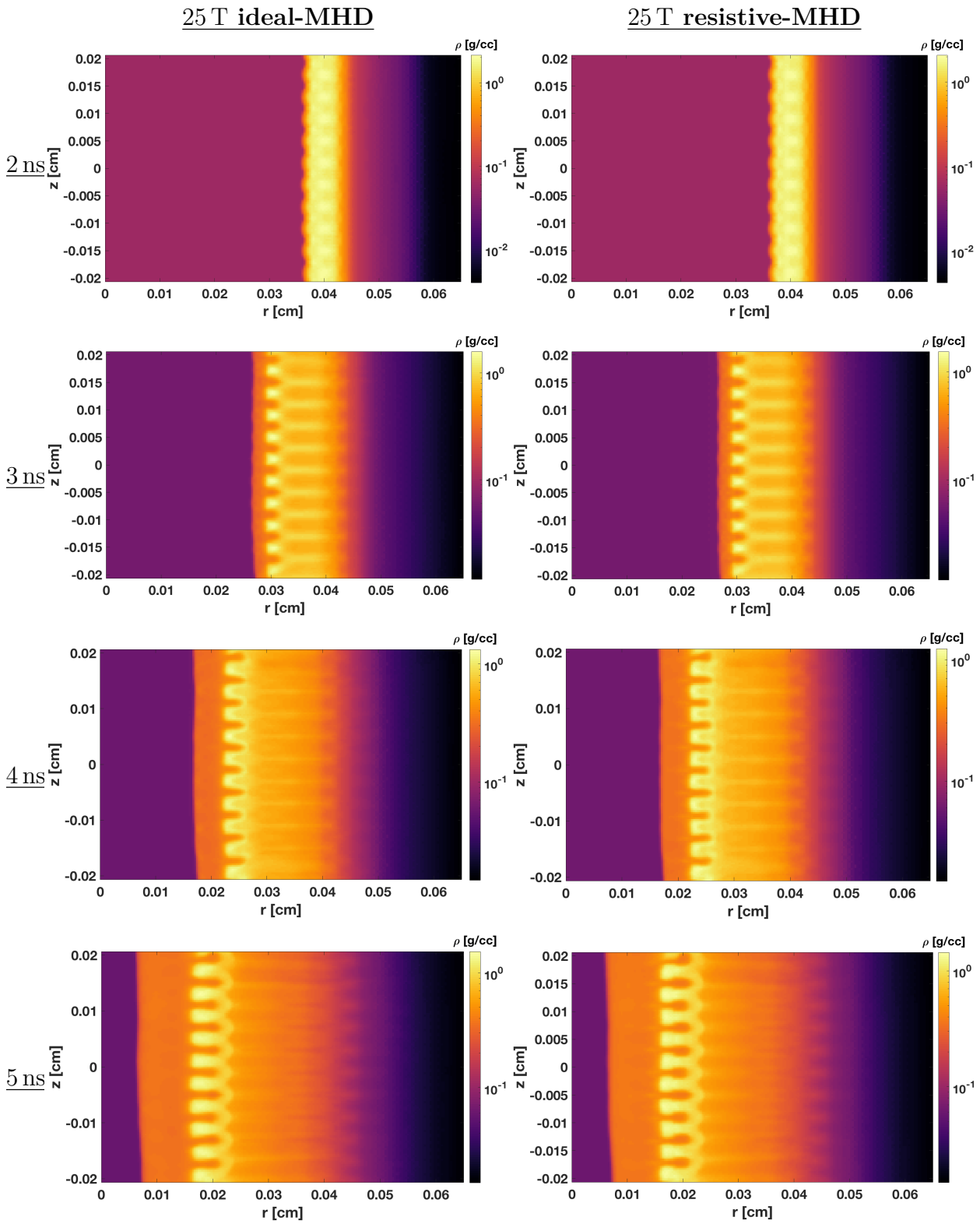

Figure 2.6: Density plots at 2 ns, 3 ns, 4 ns, and 5 ns of the RT instability growth during deceleration, modeled in ideal-MHD and resistive MHD both with a 25 T background fields. The damping impact of the magnetic field is seen in the ideal-MHD case where the RT instability growth and morphology differs from the resistive-MHD case.

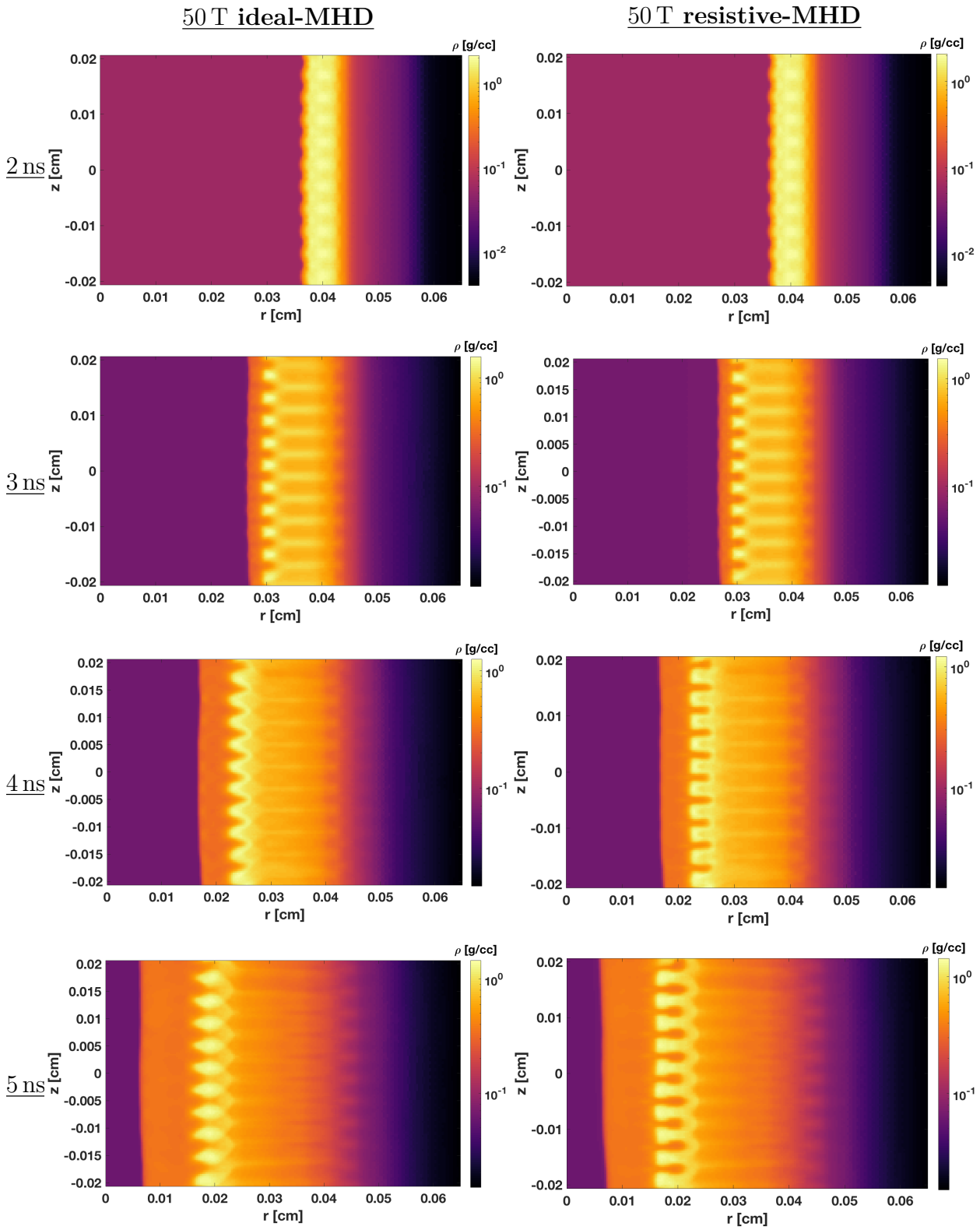

Figure 2.7: Density plots at 2 ns, 3 ns, 4 ns, and 5 ns of the RT instability growth during deceleration, modeled in ideal-MHD and resistive MHD both with a 50 T background fields. The damping impact of the magnetic field is clearly seen in the ideal-MHD case where the RT instability growth and morphology is greatly reduced in comparison to the resistive-MHD case.

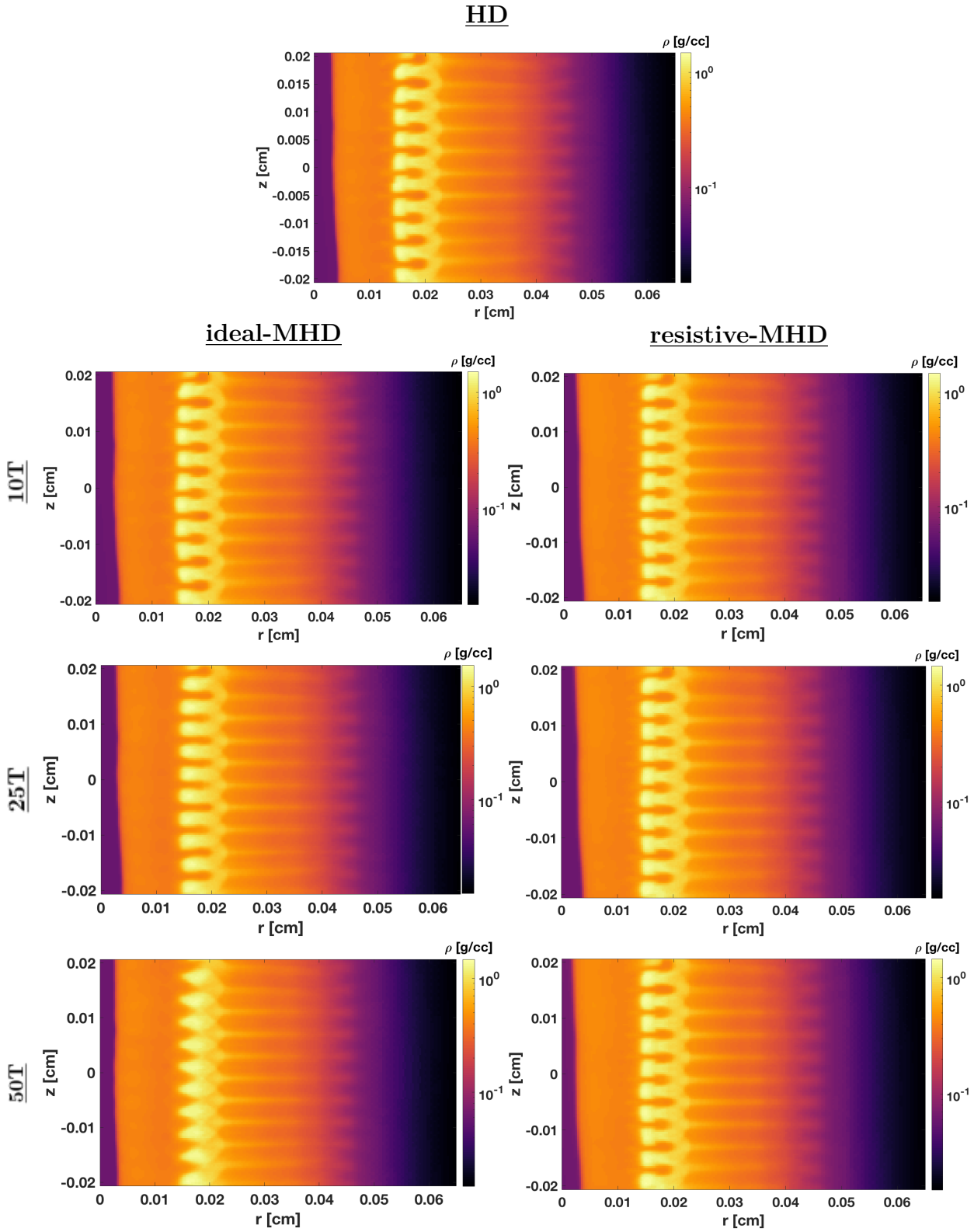

Figure 2.8: Density plots at 5.4 ns of the RT instability growth during deceleration, modeled in an HD, MHD and resistive MHD both with 10 T, 25 T, and 50 T background fields. The damping impact of the magnetic field, especially as the strength of the field increases, is clearly seen in the ideal-MHD cases where the RT instability growth and morphology gets progressively more damped. The resistive-MHD cases demonstrate that in the presence of magnetic field the RT instability growth morphology experience little damping effects.

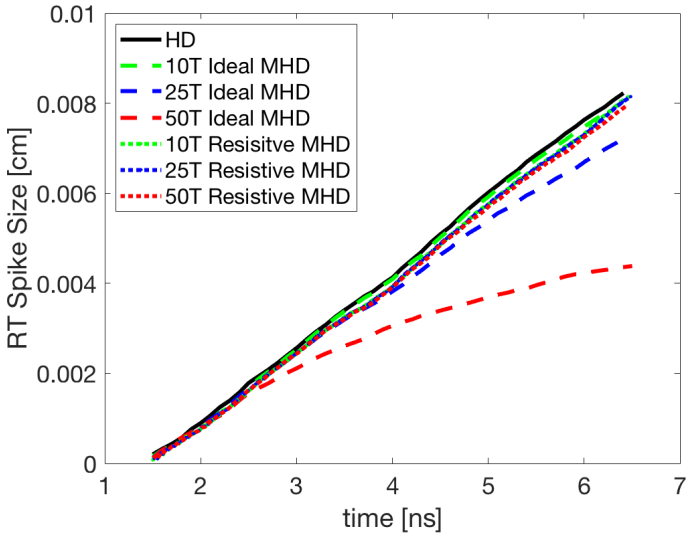

Figure 2.9: Measured growth of the Rayleigh-Taylor instability spike in HD, ideal-MHD, and resistive-MHD cases for the cylindrical Omega-based experimental configuration. The HD simulation RT growth is seen in the black solid line, while ideal-MHD can be found in the dashed lines, and resistive-MHD is seen in the dotted lines. The differing seed magnetic fields are distinguished with green representing 10 T cases, blue 25 T, and red 50 T. This demonstrates that the addition of resistivity reduces the impact that the magnetic field has on the RT instability growth, resulting in growth comparable to that found in the HD regime.

implosions. As such it clearly demonstrates that the ideal-MHD regime provides up to 400 μm of measurable reduction in RT instability growth. The HD and resistive-MHD schemes presents a difference in the RT instability growth on the order of only a few microns. This small difference demonstrates that, in the case of solid density liners, small seed background fields would show no differences between HD and resistive-MHD simulations because of the large resistivity that solid liners present. This is notable given that even in the resistive cases there is magnetic field amplification during the implosion. However, the presence of resistivity inhibits flux compression of the magnetic field, and while plasma experiences much higher magnetic fields than the original seeded 10 T, 25 T, and 50 T, the field strengths are diminished in the presence of resistivity.

It is clear that where the magnetic field is embedded in the flow matters to how the RT

instability grows; when embedded around the RT spike growth, there is a reduction in growth, which is the case for the ideal-MHD setup. The case of the ideal-MHD with a 50T starting magnetic field results in a peak magnetic field of strength 461 T. Comparably, in the resistive-MHD cases, the 50 T case also has the largest peak magnetic field at 1013 T. However, only the 10 T resistive case has a lower maximum magnetic field when compared to the ideal 10 T case. In the resistive-MHD cases, the highest magnetic field, despite being demonstrably larger than the ideal-MHD cases, occurs in the material in front of the shock. Therefore, a smaller magnetic field amplification occurs around the RT instability, $\sim$ 70 T, and little effect is seen on the growth.

The ideal-MHD cases produce temperatures around the RT instability growth on the order of 25 eV and 15 eV within the RT instability spikes themselves, and the resistive-MHD cases produced comparable plasma temperatures, seen in Figure 2.10. Both the resistive-MHD and ideal-MHD simulations, despite the morphology differences, are also within the same temperatures seen in the HD case, thus the addition of the magnetic field has little effect on the temperatures reached in the system during implosion.

Another measure of the impact of the magnetic field may have on a plasma is the magnetic Reynolds number. This is the measure of the ratio of induction to diffusion in the plasma, meaning a ratio of the velocity times the scale length of the plasma flow to, in this case, the resistive diffusivity, R_m = UL/D. L is set to the wavelength of the RT instability seed perturbation, λ= 40 μm, the local velocity, U, is extracted from FLASH's output data and in the resistive-MHD case the diffusivity, D, is set to diffusivity over resistivity, μ_0/η, extracted from FLASH as shown in Equations 1.13 and 1.14. Since the ideal-MHD and HD cases do not use a resistivity term, the diffusivity is estimated for these cases using a resistivity formula given by,

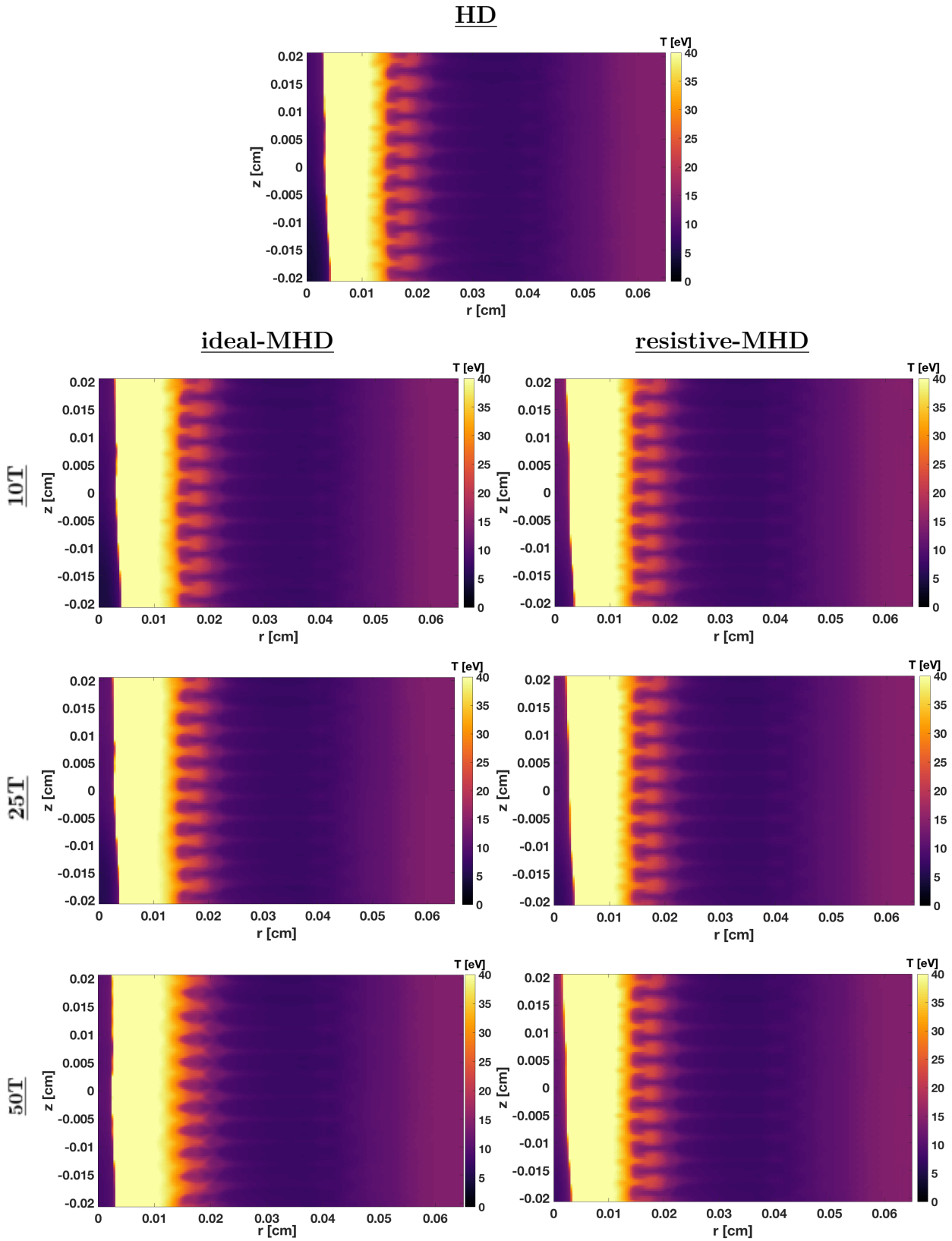

Figure 2.10: Temperature at 5.4 ns during deceleration in an HD, 10 T, 25 T, and 50 T ideal-MHD and resistive-MHD case. The temperature is ∼25 eV around the RT instability growth and is at about 15 eV within the instability in all the cases.

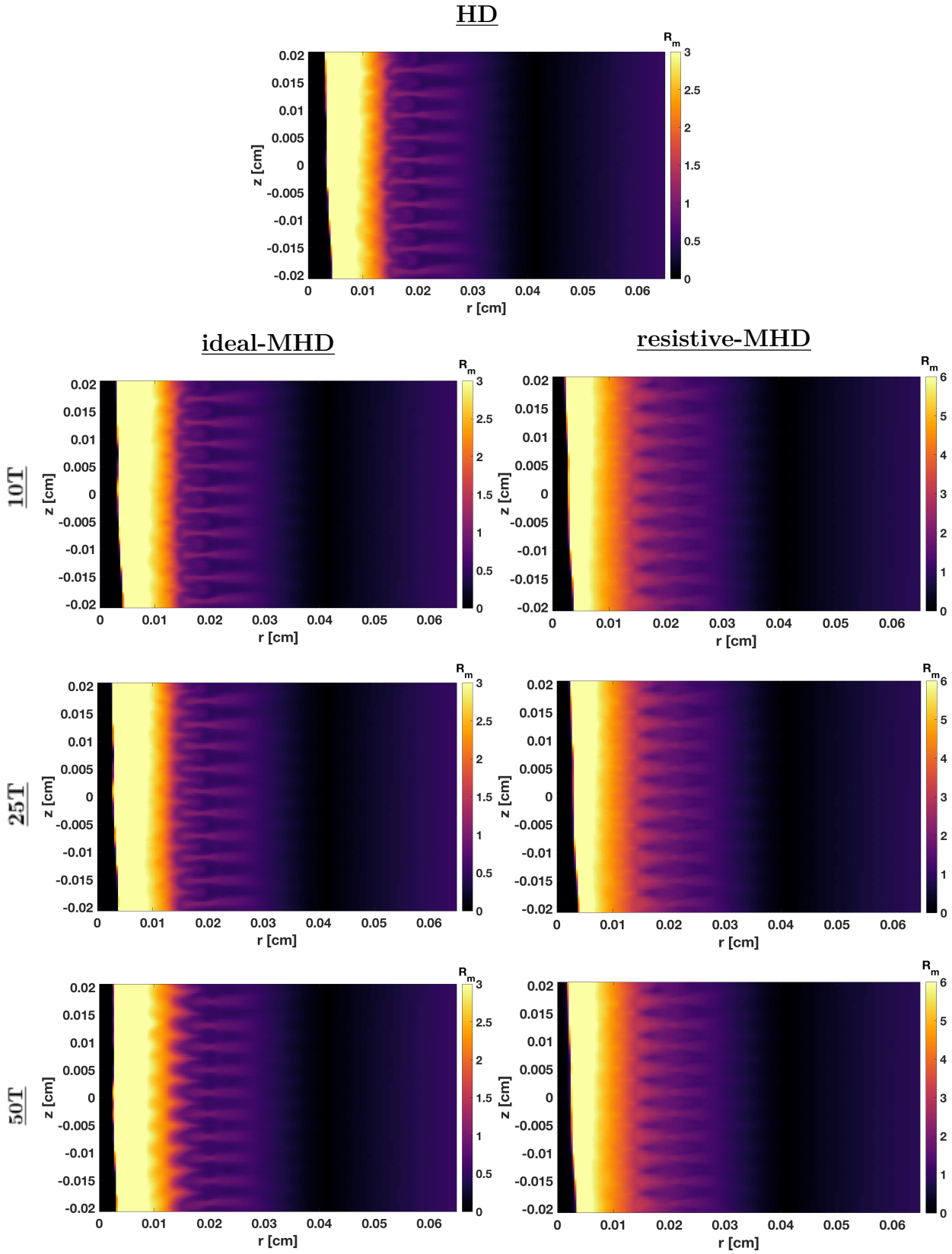

Figure 2.11: Magnetic Reynolds number at the same time step, 5.4 ns, plotted for HD, all the ideal-MHD and resistive-MHD cases. The magnetic Reynolds number is twice as large in the resistive-cases, yet in all the simulations it is between 1 and 3 in the RT instability growth, indicating little measurable impact from an externally applied magnetic field.

$$\eta_{est} = 3.3 \times 10^{-9} \frac{Z_i ln\Lambda}{T_e^{\frac{3}{2}}}, \tag{2.1}$$

where $ln\Lambda$ estimated to be 2, Z_i is the local average ionization (found in FLASH) and T_e is the local temperature in eV (from FLASH). Equation 2.1 demonstrates the temperature dependence of the magnetic Reynolds number; thus, the low temperatures seen in Figure 2.10 result in the low magnetic Reynolds numbers seen in Figure 2.11. In the ideal-MHD and HD cases, a low magnetic Reynolds numbers of approximately 2 to 2.5 is seen in the plasma surrounding the RT instability growth, and is as low as 0.5 in some places within the RT instability itself. This suggests that ideal-MHD is not appropriate for these regimes as the role of resistivity is significant and cannot be neglected. Hence resistive-MHD simulations may provide a more accurate representation of the evolution in these regimes. In comparison, the resistive-MHD cases shown in Figure 2.11 demonstrate a two-fold increase of the magnetic Reynolds number in the shock front but not in and around the RT instability. However, a magnetic Reynolds number of 5 is not large enough for the seeded magnetic field to have a measurable impact on the RT instability growth, which is clearly seen in the morphology similarities of the RT instability growth in HD and resistive-MHD. These lower temperatures and magnetic Reynolds numbers could be improved by increasing the laser drive, which would require shifting to a NIF platform, and possibly adjusting the cylinder densities from solid density liners to foam liners. This would allow for higher temperatures and larger implosion velocities to be achieved, thus increasing the magnetic Reynolds number and potential for a magnetic field to mitigate the RT instability growth.

2.3 Multi-Mode Sinusoidal Perturbation

In the case of RT instability growth on a machined ICF capsule, there is not likely to be a single consistent sinusoidal perturbation, but small scale imperfections at various wavelengths. Therefore, a case with multiple perturbation wavelengths are used to more clearly replicate what a surface with random imperfections would look like during deceleration stage RT instability growth. The setup from Section 2.2 is used but with a 40 μm, a 50 μm, an 80 μm, and a 100 μm perturbation, all with an amplitude of 5 μm applied to the interior surface. As can be expected in a multi-mode configuration, the mixing caused by the RT growth and the small scale structures is much more pronounced, seen in Figure 2.12, and the presence of a magnetic field increasing in strength across the different cases changes the RT instability morphology in the ideal-MHD cases verses the resistive-MHD cases, seen in Figure 2.13, 2.14, and 2.15. A comparison of the RT instability growth at 5.4 ns can be seen in Figure 2.16, which clearly depicts the reduction in RT instability growth in the ideal-MHD cases and the similarity between the resistive-MHD cases and the HD case.

Again, the damping effects of a background magnetic field is distinctly more obvious in the ideal-MHD regime, where the KH vortexes developing in the HD case are much, if not completely, damped as the seed magnetic field increases with strength from 10 T to 50 T. The RT instability growth is distinctly globular and unmixed, again seen in Figure 2.16. Additionally, the resistive-MHD cases, again, do not depict any notable RT instability morphology or growth damping, seen in the single mode case. In the presence of a magnetic field for the ideal-MHD and resistive-MHD cases, we see comparable results to what the 40 μm perturbation showed. In the ideal-MHD cases, the magnetic field is highest in the region of the RT growth, while the resistive-MHD cases' dominant magnetic field amplification is in the shock front, with fields on the order of 10x the initial seed field strength. The magnetic

field amplification is present, but due to low temperatures and magnetic Reynolds number, its effect on the RT instability growth is not observed.

The temperatures reached in the multi-mode regime are higher than those seen in the 40 μm configuration. The plasma surrounding the RT instability in the HD, ideal-MHD, and resistive-MHD cases are all hotter, on the order of 40 to 50 eV, while the temperatures in RT instability growths themselves are still on the order of 15 to 25 eV, seen in Figure 2.17. Since the temperature is higher, the magnetic Reynolds number is higher, as seen in Equation 2.1. The magnetic Reynolds number is still the best indicator of the mitigation from the magnetic field on RT instability growth in an experiment. The HD and the ideal-MHD cases all demonstrate that the magnetic Reynolds number is between 2 and 5 in and around the region of RT instability growth, as seen in Figure 2.18. These values double with the addition of background magnetic fields in the resistive-MHD case, where the magnetic Reynolds number can be seen to be up to 10 in the plasma surrounding the RT instability growths in Figure 2.18. This shows that the resistive-MHD regime indicates a more effective conduction of magnetic fields through the plasma. However, like in the single mode configuration, these temperatures and magnetic Reynolds number values are not large enough for the resistive-MHD cases to demonstrate a damping effect on RT instability growth in the presence of background magnetic fields. Given the solid densities used in these cylindrical configurations and the lower Omega laser powers, an effort to explore laser powers on the scale of the National Ignition Facility and foam targets in Cartesian coordinates to achieve the necessary temperatures and magnetic Reynolds numbers is described in Chapter 3.

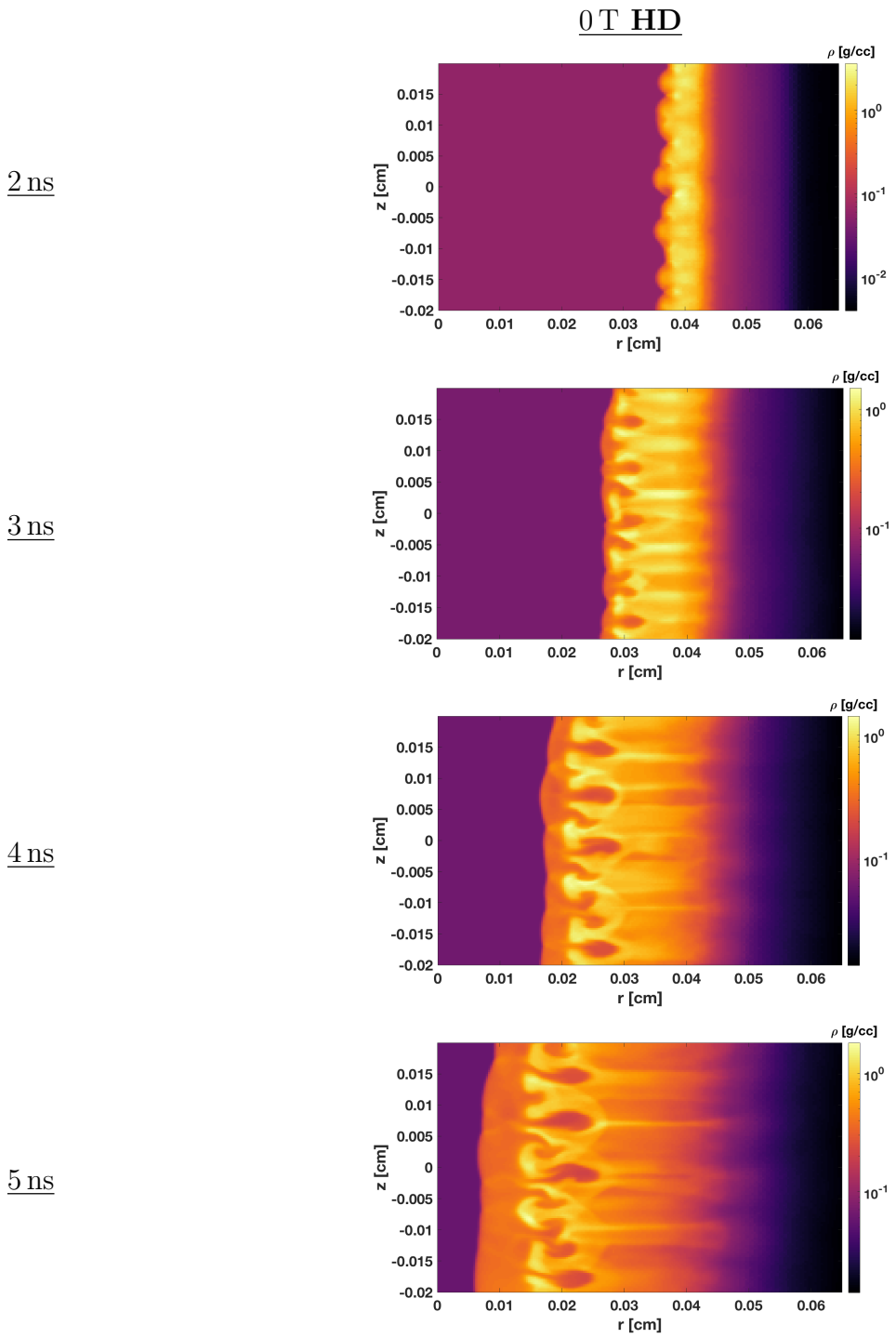

Figure 2.12: Density plots at 2 ns, 3 ns, 4 ns, and 5 ns of the multimode RT instability growth during deceleration, modeled in HD both without a background fields. The RT instability growth is shown to develop prominently on the interior of the solid density shell.

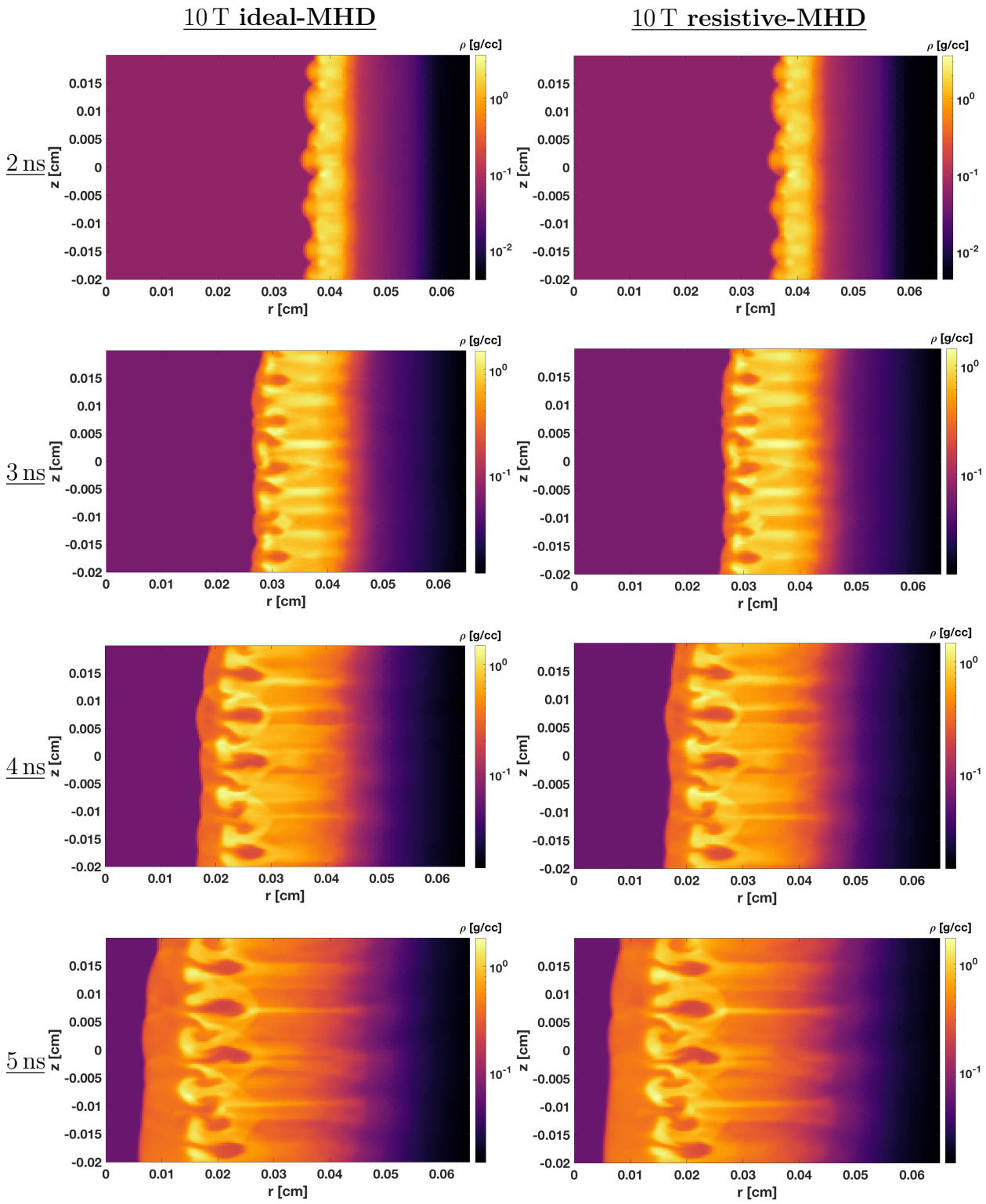

Figure 2.13: Density plots at 2 ns, 3 ns, 4 ns, and 5 ns of the multimode RT instability growth during deceleration, modeled in ideal-MHD and resistive MHD both with a 10 T background fields. The damping impact of the magnetic field is not obviously seen in the ideal-MHD morphology or the resistive-MHD cases.

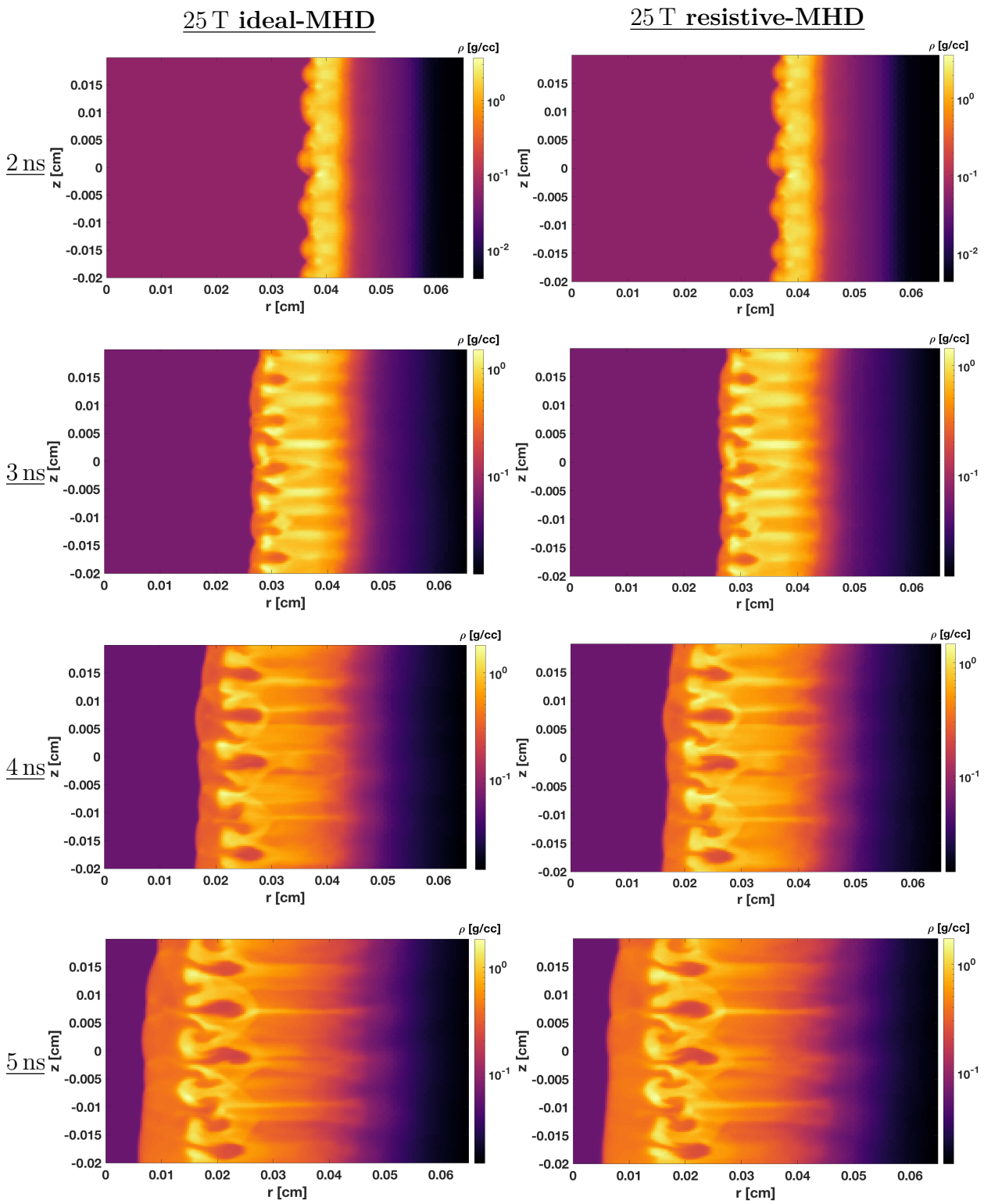

Figure 2.14: Density plots at 2 ns, 3 ns, 4 ns, and 5 ns of the multimode RT instability growth during deceleration, modeled in ideal-MHD and resistive MHD both with a 25 T background fields. The damping impact of the magnetic field is seen in the ideal-MHD case where the RT instability growth and morphology differs from the resistive-MHD case.

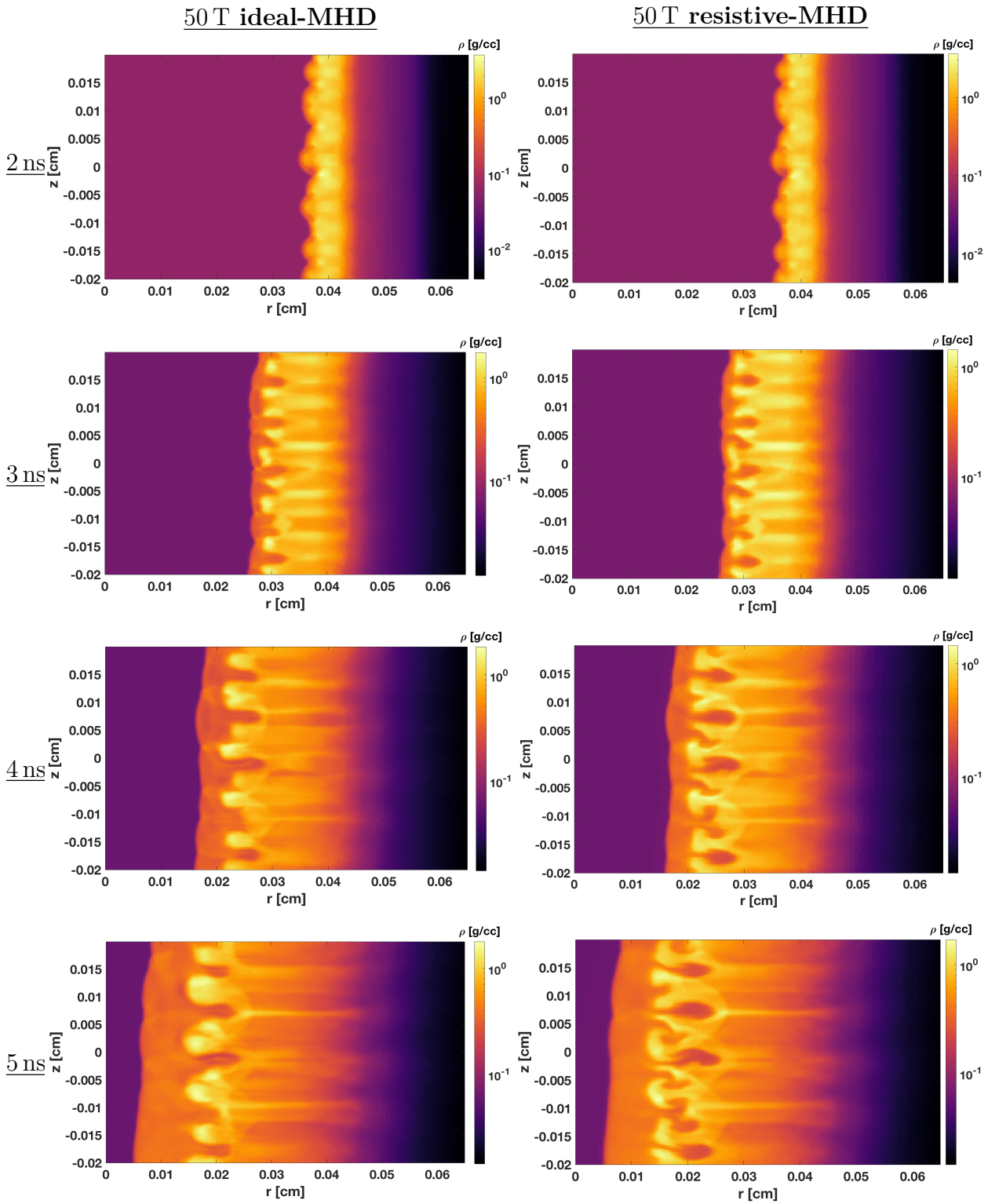

Figure 2.15: Density plots at 2 ns, 3 ns, 4 ns, and 5 ns of the multimodeRT instability growth during deceleration, modeled in ideal-MHD and resistive MHD both with a 50 T background fields. The damping impact of the magnetic field is clearly seen in the ideal-MHD case where the RT instability growth and morphology is greatly reduced in comparison to the resistive-MHD case.

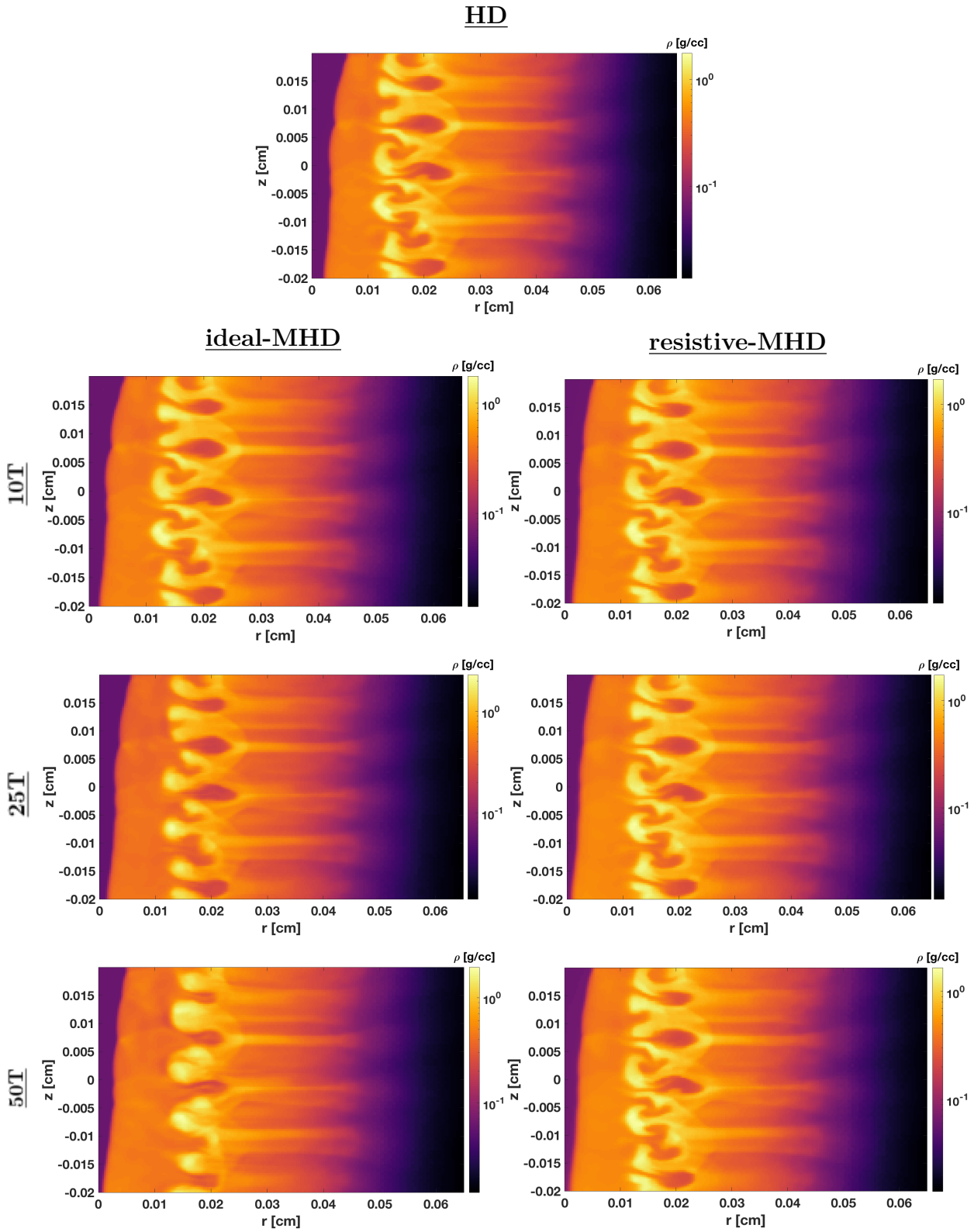

Figure 2.16: Density plots at 5.4 ns of the multi-mode configuration, simulated in HD, ideal-MHD, and resistive-MHD, the latter two simulated with 10 T, 25 T, and 50 T background magnetic fields. The damping effect of the magnetic field is seen progressively getting strong in the ideal-MHD cases, while the resistive-MHD cases bare little difference to the HD case.

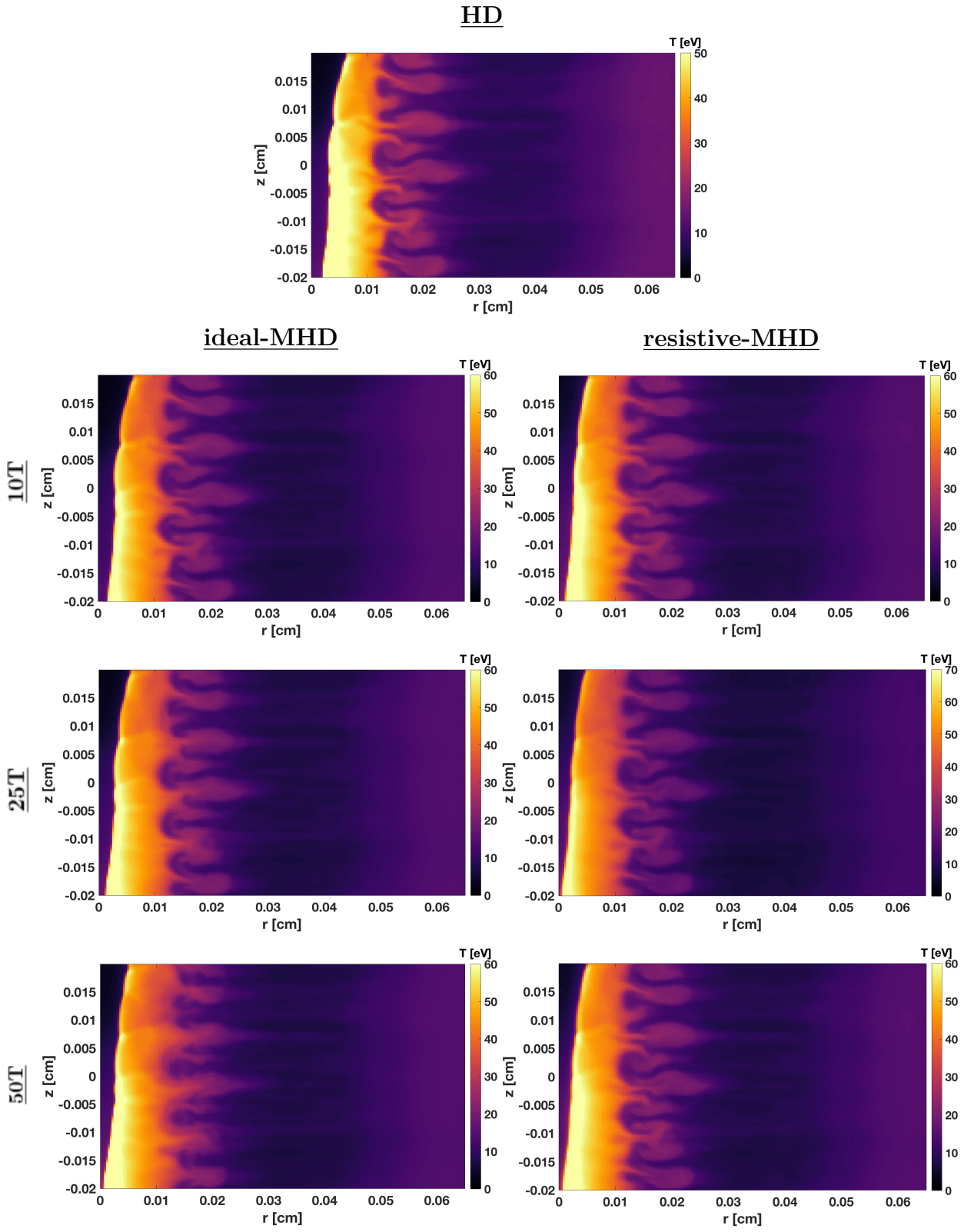

Figure 2.17: Temperature plots at 5.4 ns of the multi-mode configuration, in HD, 10 T, 25 T, and 50 T ideal-MHD and resistive-MHD. The temperatures reached in all the cases, regardless of equation system or magnetic field, are comparable and do not go above 30 eV in and around the RT instability growth.

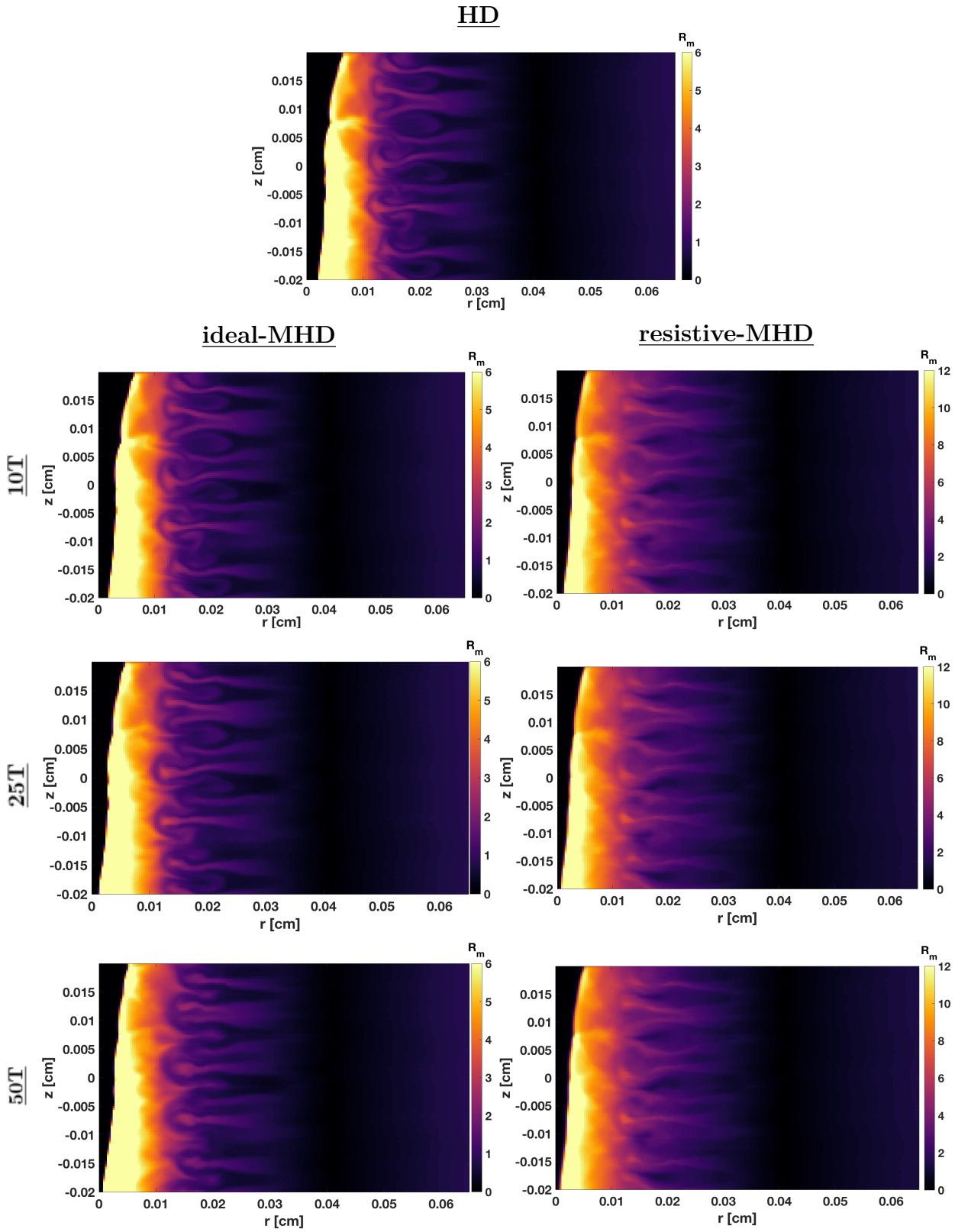

Figure 2.18: The magnetic Reynolds number at 5.4 ns of the multi-mode configuration, demonstrating that again the introduction of resistive-MHD nearly doubled the value; however in and around the RT instability the magnetic Reynolds number does not get higher than ∼7.

Chapter 3

Blast-Wave Driven Deceleration Rayleigh Taylor Growth

This chapter will address a series of simulations performed with the intent to validate and prepare for laser experiments on Omega-EP and the National Ignition Facility (NIF). The configuration for these experiments are designed to study a blast-wave driven declaration stage RT instability growth, meaning a laser is used to drive an implosion of a rectangular target in which a higher density pusher foam is machined with a perturbation and is driven into a low density target foam. These experiments and subsequent simulations aim to develop a new platform on laser-driven configurations for this new type of target, intended to demonstrate that there is a measurable effect on RT instability growth in the presence of a magnetic field.

3.1 Experimental Parameters for Omega

The Omega-EP simulation parameters used are based on an early-stage experimental campaign from the summer of 2020, with the intent to determine the effectiveness of three potentially novel target configurations. Typically foam targets used in experiments are made of a solid density material, the pusher, that is driven into a foam, the target foam. The novelty of the target configuration in this work is in the inclusion of low density foam

pusher material in addition to the foam target materials. The foam pusher uses the density of typical foam targets whereas the low density target foam is at a density of 20 mg/cm^3. The new targets require some baseline testing to determine which pusher foam would be optimal for an experiment designed to measure the effect a background magnetic field would have on the seeded RT instability growth. Therefore, three foams are explored. The first configuration is a 156 mg/cm^3 high density acrylic like foam doped with 5-10% bromine for X-ray radiography contrast referred to a HDBR from here on. The second is a 85 mg/cm^3 low density bromine doped foam, called LDBR. Lastly, a similar 215 mg/cm^3 low density acrylic foam doped with nickel, hence forth referred to as LDNI. These foam pushers are then incident on a low-density carbon-based foam target at 24 mg/cm^3. A schematic of the general target configuration can be seen in Figure 3.1, which demonstrates how the targets are setup with the high density foam pusher material with a perturbation is driven by a laser into the low density target foam.

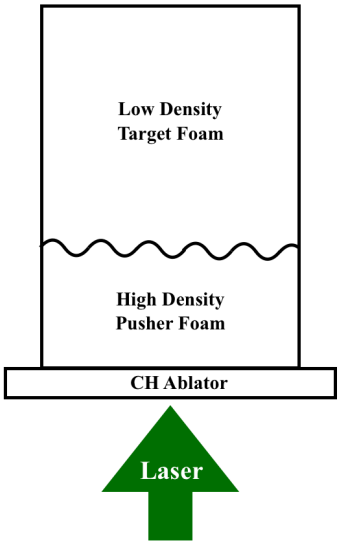

Figure 3.1: A schematic of the rectangular target configuration for the foam-foam setup. The laser is incident on a think ablator material. The high density foam material with a machined sinusoidal perturbation is propagated inwards towards the low density target foam.

Each higher density pusher foam has an approximate thickness of 200 μm and a perturbation

wavelength of λ= 80 μm. Due to machining tolerance there are differences in the perturbation amplitudes for the three types of foam. Specifically, the HDBR foam has an amplitude of 41 μm, while the LDBR has an amplitude of 43 μm, and the LDNI has an amplitude of 20 μm. A seed background magnetic field of 12 T is applied to all three cases for the ideal-MHD runs, and the LDNI target study also included a resistive-MHD simulation with the same 12 T seed background field. All three cases are simulated with a 2350 J laser drive for 2 ns, using Omega-EP's 750 μm DPP phase plate, which gives the intensity as a function of radius as

$$I(r) = I_0 e^{[-2\frac{r}{w_0}]^n}, \tag{3.1}$$

where I_0 is the laser intensity, n is the super Gaussian exponent selected to be 8.92 in this configuration, r is the radius, and a w_0 is the Gaussian radius for the laser drive set to be 336 μm. The designation of the phase plate and subsequent laser Gaussian parameters are important because the shape of the laser spot determines how the energy being used to drive the implosion is deposited on the target. A larger phase plate, like the 750 μm DPP means the intensity as a function of radius is lower on the target, seen in Equation 3.1. The importance of the laser's intensity, its subsequent effects on the RT instability growth and measurable difference in the presence of a magnetic field, are explored in the next sections.

3.2 Computational Results for Omega-EP

All three types of foam are run using the configurations described in Chapter 2 for HD and ideal-MHD, while the LDNI foam is the only setup run to use resistive-MHD. As expected from the ideal-MHD cases, there are distinctive differences in the morphology and growth of the RT instability between the HD and ideal-MHD cases for HDBR, LDBR, and LDNI, which can be seen in Figure 3.3. The first row in Figure 3.3 shows that the HDBR case

demonstrates a reduction in RT induced spike size. Figure 3.3 also shows a reduction in the bubble morphology, specifically the tendrils seen down the sides of the spike in the HD case are reduced in growth in the ideal-MHD case. Similarly, the first two rows of Figure 3.3 show the same morphology change in the LDBR as seen in the HDBR, while in LDBR the distinct size difference in the RT instability spike growth is much more easily discerned. Lastly, Figure 3.3 shows that the small scale features on the top of the LDNI spike bubbles are entirely damped in the presence of a magnetic field. The measurable difference in the HD and ideal-MHD growth is demonstrated in Figure 3.2, where for HDBR, LDBR, and LDNI, the ideal-MHD case diverges from the HD and results in the RT instability growth amplitude measuring up to a difference of 100 μm in the case of the LDNI foam. The presence of the small scale features growth on top the RT instability spikes, and the non-uniformity of the RT instability bubbles causes the LNDI peak to valley measurement to have a margin of error. The error is measured as the potential to measure the RT instability height peak at the top of small growths or at the base of the growths on the RT bubbles.

Additionally, the temperatures achieved in these test foam configurations for the Omega-EP laser are not as hot as necessary. Figure 3.4 shows the temperature in each foam target at 13 ns into the implosion, where temperature did not surpass 20 eV in any of the foams, with the LDNI foam having the lowest temperatures in and around the RT instability growth. Similarly the magnetic Reynolds number in each system, shown in Figure 3.5, doesn't get higher than 1.4 in any of the systems. The LDBR foam achieves the highest magnetic Reynolds on the order of 1.4, which is not at the level needed to observe magnetic stabilization. A magnetic Reynolds number would need to be 40 in order to see the impact that magnetic fields have on the evolution, as described in Section 3.4. Although there is magnetic field amplification during the implosion the small seeded magnetic field is not high enough to observe any differences in RT growth. Lastly, an additional metric used for understanding

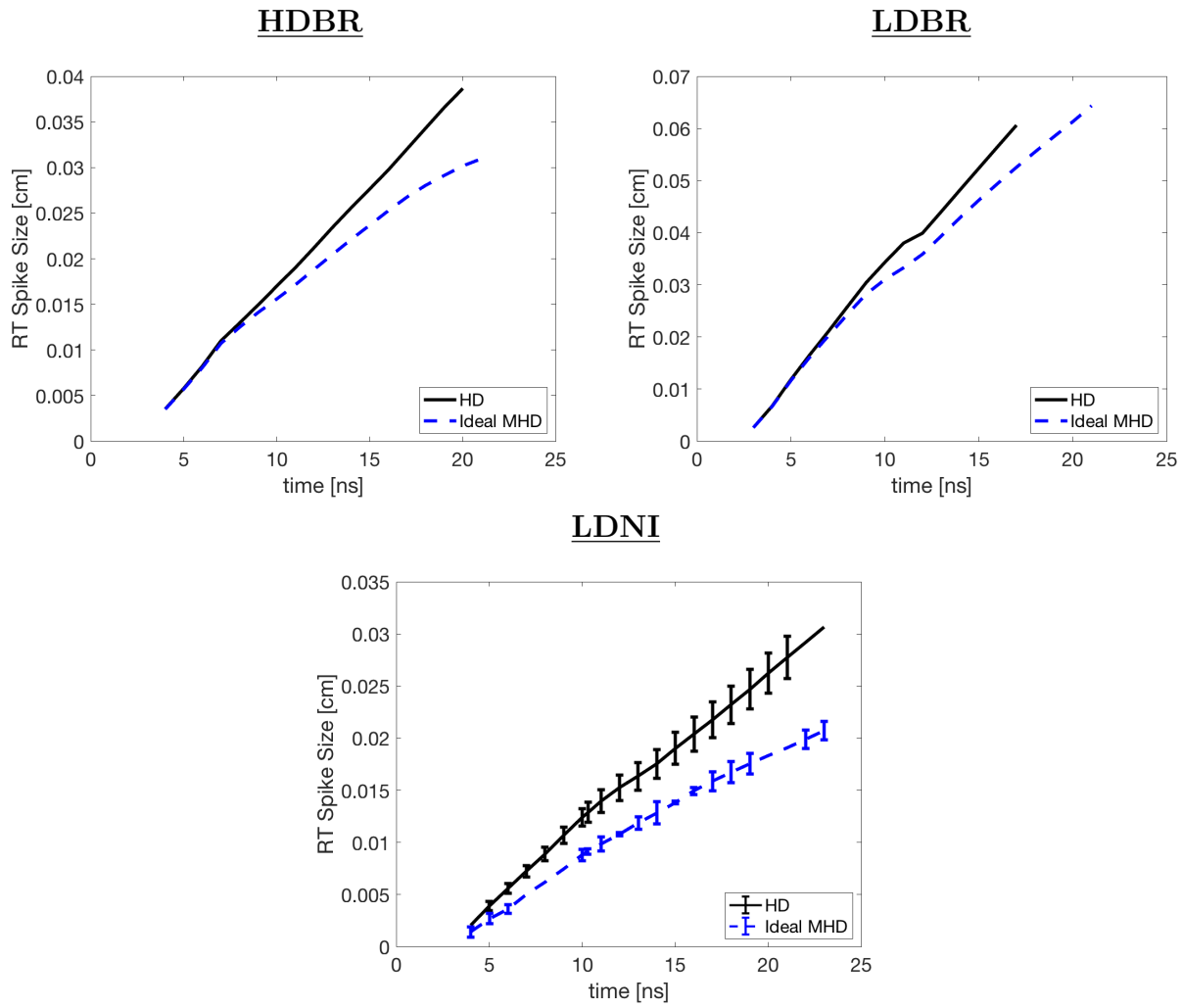

Figure 3.2: Plots of the measurement from the bottom of the RT instability growth to the top of the RT instability bubble, resulting in a spike size measurement of the growth in the HDBR, LDBR, and LDNI foams for both HD and ideal-MHD cases. The clear damping of the RT instability growth is seen in the difference in size between the two types of runs.

the impact of a magnetic field on a system is the ratio of the hydrodynamic pressure to magnetic pressure, β, such that $\beta = 2\mu_0\rho u^2/\mathrm{B}^2$. In these test foams, β in the ideal-MHD cases lies between 10^1 and 10^4 in and around the RT instability growth, Figure 3.6, which is large enough to indicate that the plasma will see little impact from extended-MHD term like the Hall term. Additionally, this indicates the magnetic field would not have a noticeable impact on the instability growth in the plasma. Thus, resistive-MHD runs present little difference in

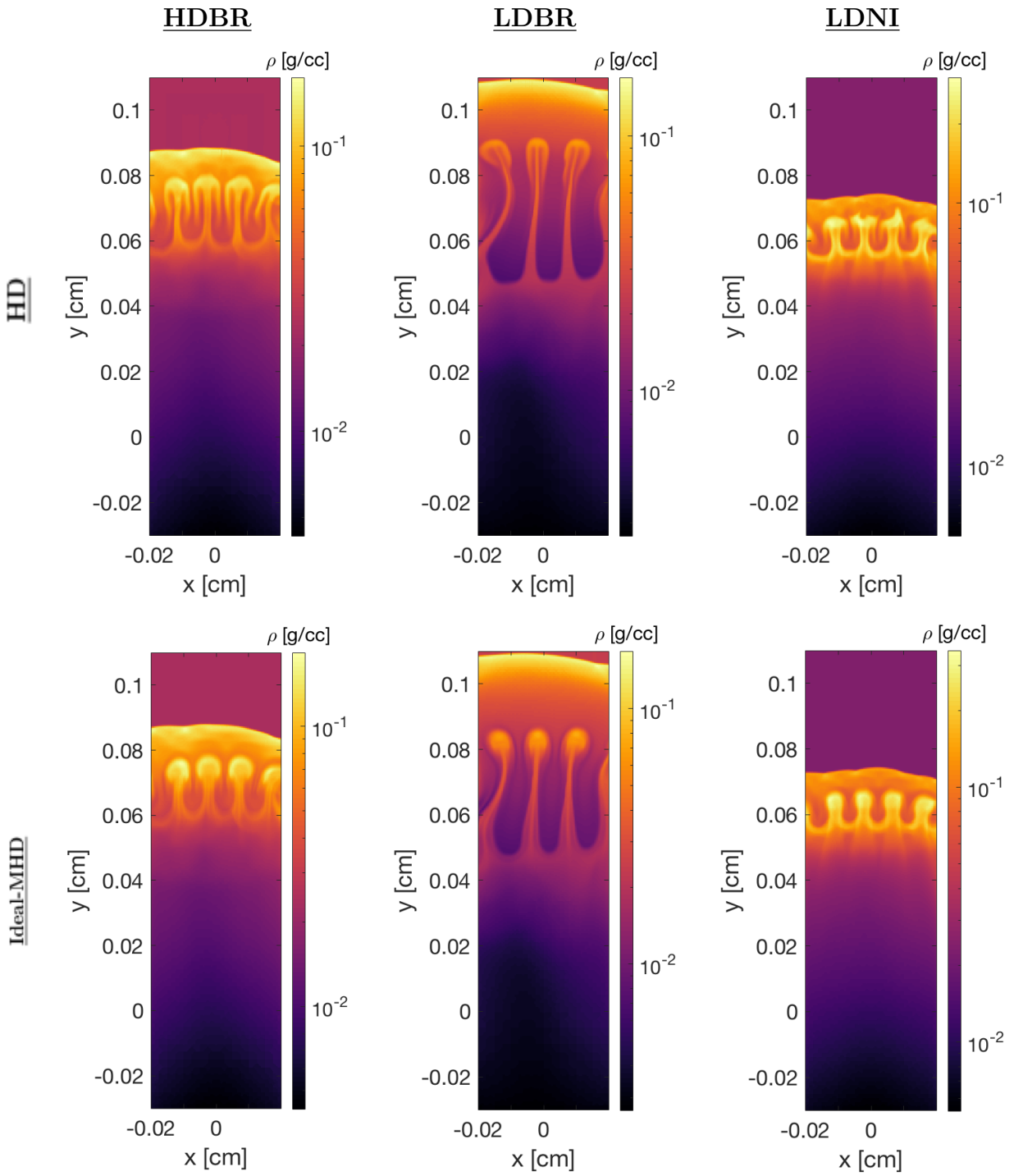

Figure 3.3: Density plotted at 13ns into the implosion for the HDBR, LDBR, and LDNI test foams. The HD cases are in the top row and the ideal-MHD, in which a 12 T background magnetic field is applied, are seen in the second row. Comparing the HD runs to the ideal-MHD runs for each test foam demonstrates how the applied magnetic field damped the RT instability growth.

the RT instability's growth during the implosion when compared to a non-magnetized case.

A resistive-MHD case is constructed for the LDNI foam test case and the density, temperature, magnetic Reynolds number, and plasma β results are displayed in Figure 3.7. As can be observed in this figure, the resolution at which the mesh for this case is run is much lower than the latter cases. The addition of resistivity in FLASH results in further numerical constraints using a semi-implicit scheme. Since the scheme is not fully implicit, parabolic equations are computationally expensive because of their highly restrictive time scales. Resolving large resisitivities at small spatial scales becomes computationally unfeasible with current computing resources which is seen through a time step reduction of several orders of magnitude. This low resolution LDNI case ran for 5 days before completing and other resistive cases discussed later in this chapter have run for upwards of 28 days. Therefore, for these early-stage tests a lower mesh refinement is used in an effort to increase the time-step by having a larger Δx. Despite the low refinement the results are markedly similar to the HD and ideal-MHD cases described previously.

The Omega-EP experiment resulted in one image of the LNDI test configuration being captured of the non-magnetized RT instability growth seen in Figure 3.8. As can be seen the imaging plate that is used had existing scratches and imperfections which arbitrarily increased the signal to noise of the image, thus making analysis extremely difficult. Additionally, due to a power scaling error in the original FLASH simulations, the initial simulations evolved much slower than what is observed on Omega-EP during the experiments. Fortunately, the RT instability growth is distinguishable in the x-ray radiograph, designated by the colored features seen between the dotted lines in Figure 3.8. This allows for a benchmarked LDNI foam case to be developed.

The benchmarked LDNI simulations are developed by properly scaling the laser drive to match the RT instability growth at 7 ns with the x-ray radiograph from the experiment. The

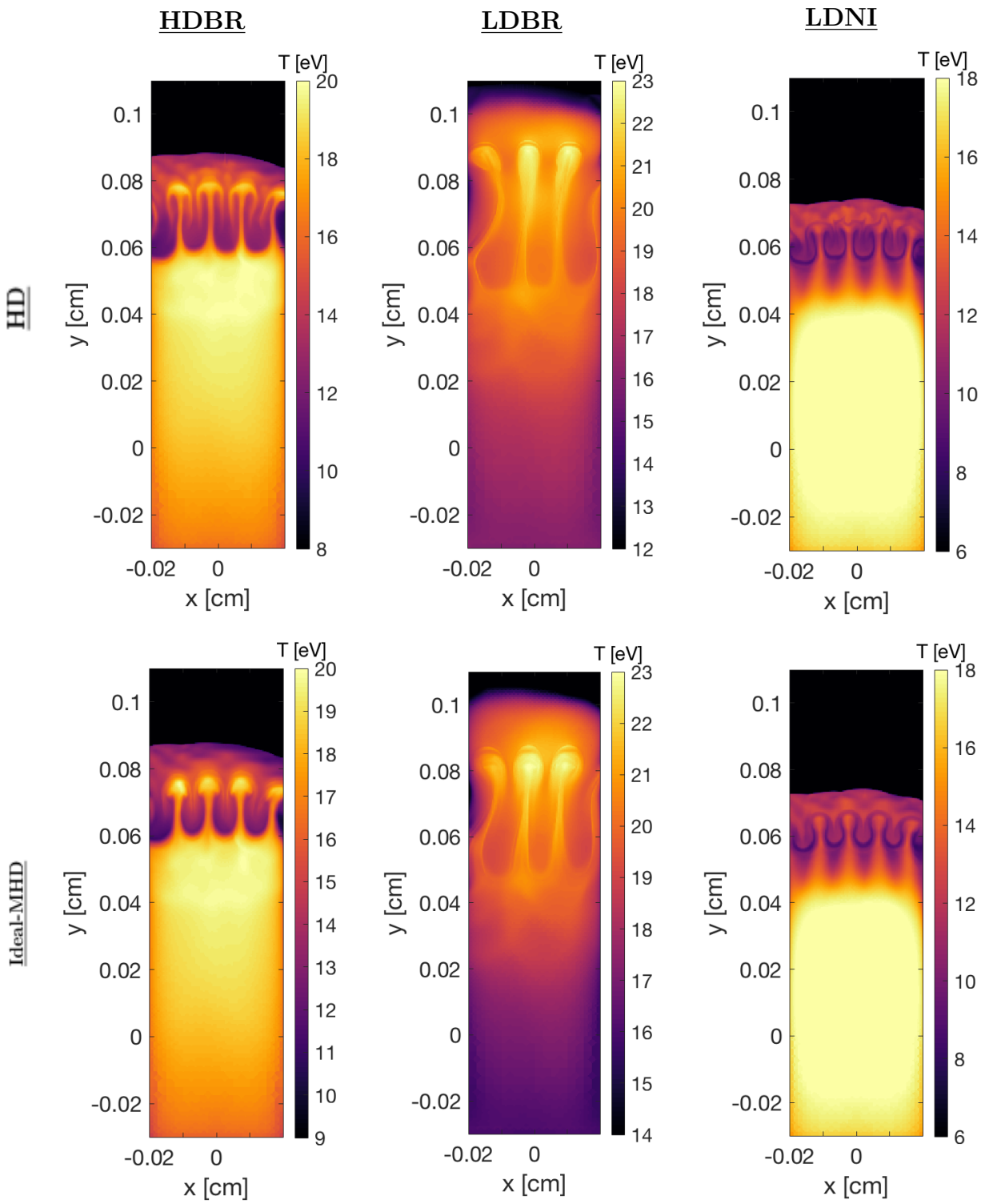

Figure 3.4: Temperature in eV plotted at 13ns into the implosion for the HDBR, LDBR, and LDNI test foams, with the HD cases in the top row and the 12 T ideal-MHD in the second row. The temperature in all cases does not get above 25 in any of the runs.

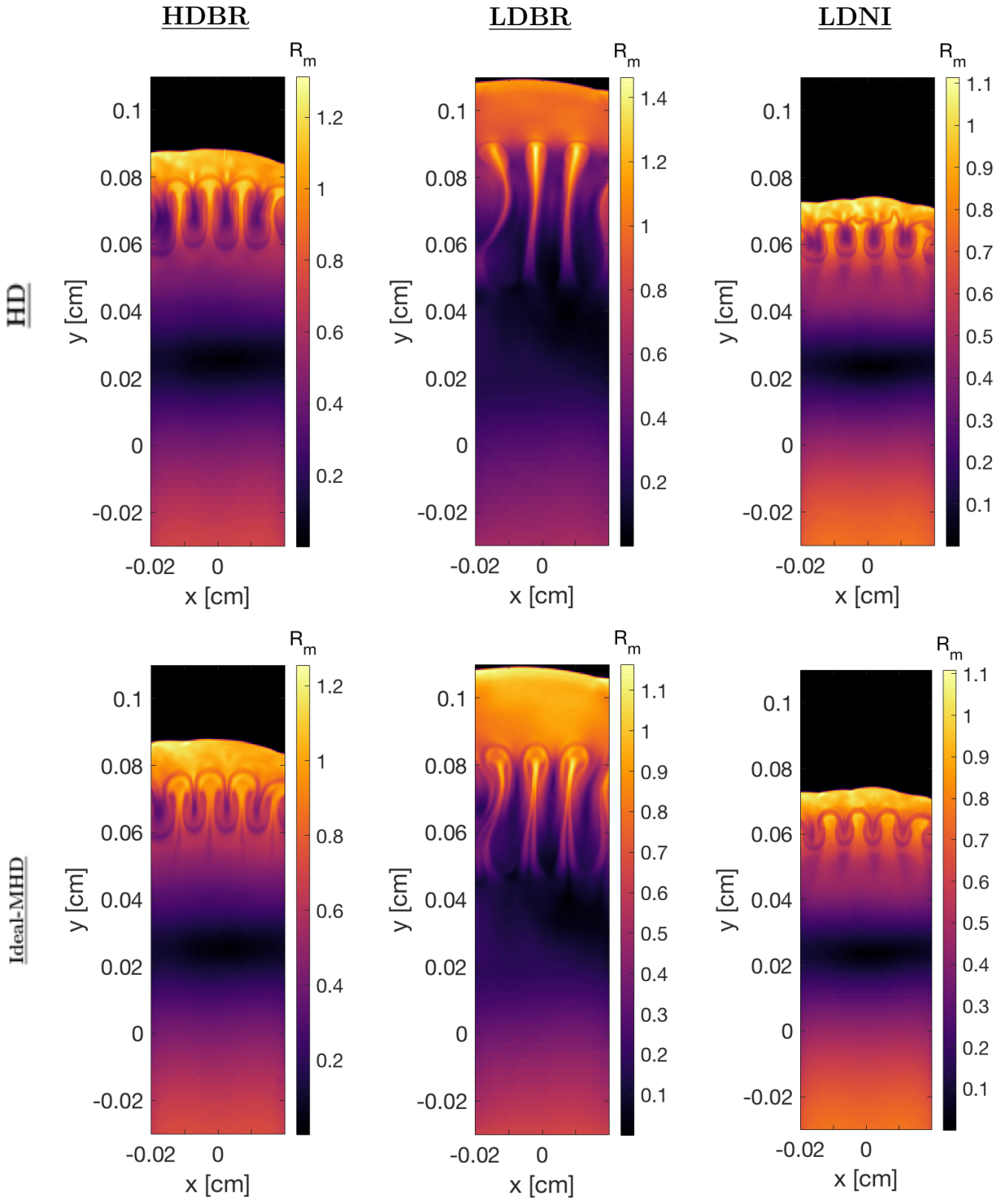

Figure 3.5: Magnetic Reynolds numbers of the plasma plotted at 13ns into the implosion for the HDBR, LDBR, and LDNI test foams. The HD cases are in the top row and the 12 T ideal-MHD are in the second row. The magnetic Reynolds number achieved in both HD and ideal-MHD clearly never get above 1.3, thus indicating that in the presence of resistivity the plasma will not demonstrate any impact on the RT instability growth.

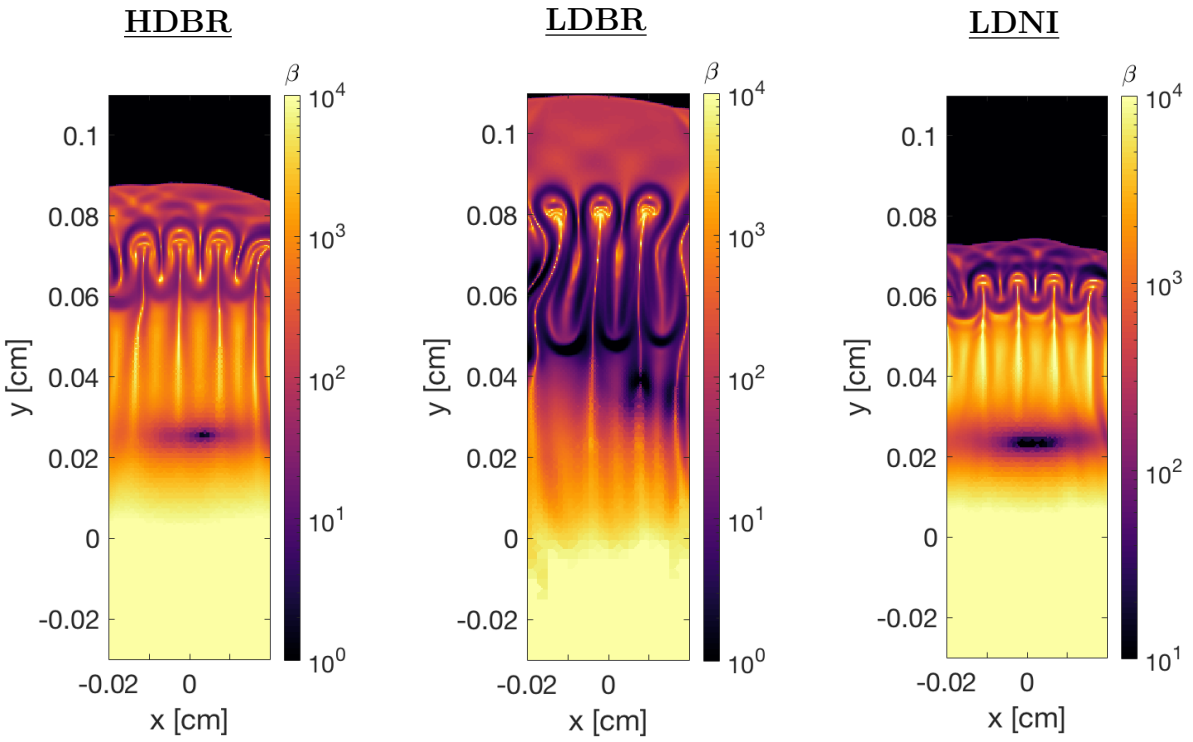

Figure 3.6: Plasma β plotted at 13ns into the implosion for the HDBR, LDBR, and LDNI test foams. The HD cases are in the top row and the 12 T ideal-MHD are in the second row. The plasma β clearly sits between 10^1 and 10^3, thus demonstrating that magnetic applied magnetic fields would have little impact on the plasma and RT instability growth.

results can be seen in Figure 3.9, where the HD and ideal-MHD cases are presented. As can be seen in density plots, the distinct small scale features are still present in the HD cases and damped in the ideal-MHD along with the RT instability growth being damped. Additionally, the temperatures observed in Figure 3.9 are on the order of 40-45 eV in and around the RT instability growth, which is twice as hot as previously predicted. Consequently, the magnetic Reynolds number is higher in both the HD and ideal-MHD cases; however it is still only on the order of 5-7, thus is still too small for the impact of the 12 T seeded background magnetic field to be measurable in a resistive-MHD case. Lastly, the plasma β, seen in Figure 3.10, is still on the order of 10^2 to 10^4, which offers little difference from the original simulations of the LDNI foam. The damping of the RT instability growth is obvious in the case of the

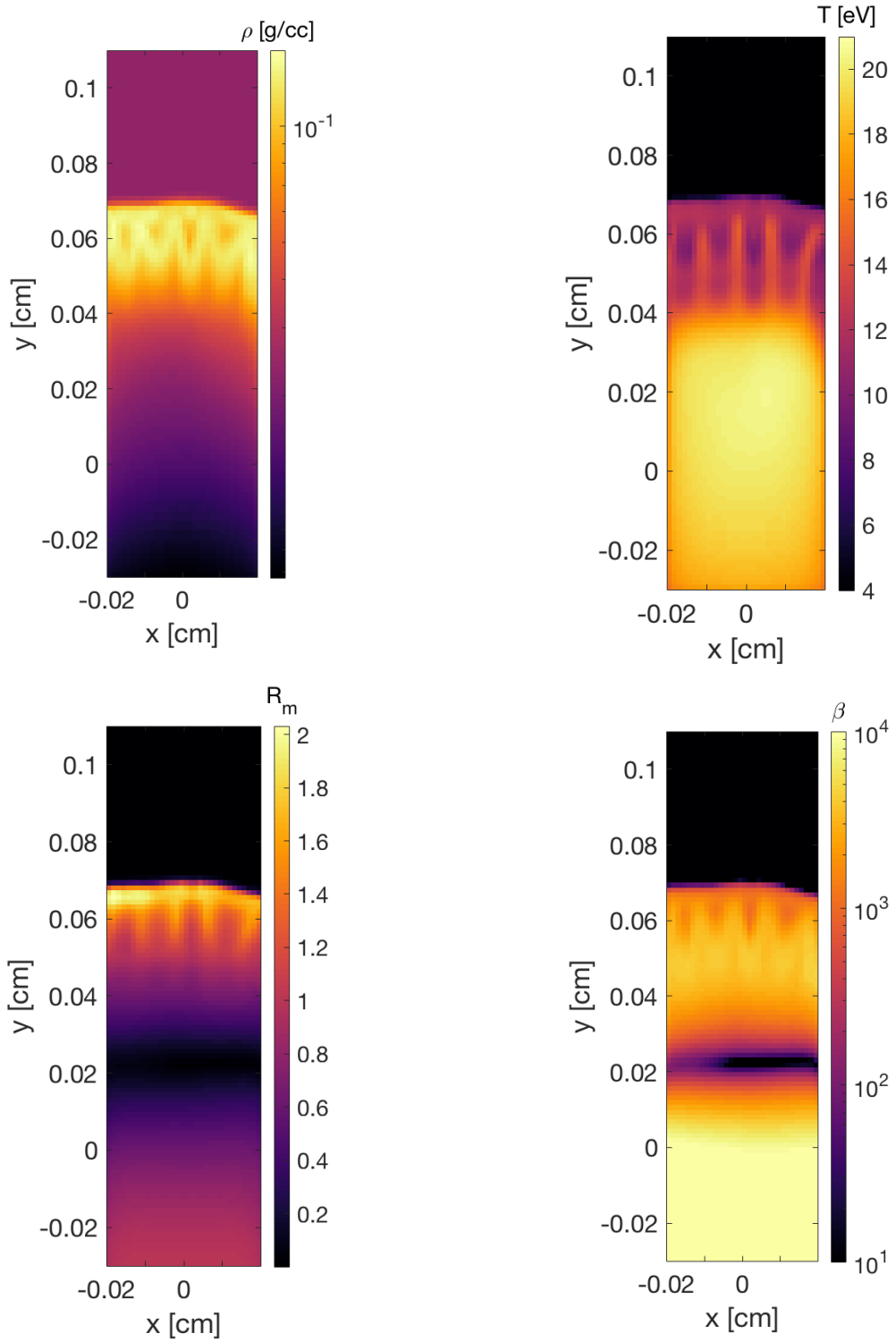

Figure 3.7: Density, temperature, magnetic Reynolds number, and plasma β plots of the low resolution LDNI resistive-MHD case also plotted at 13ns into the implosion.

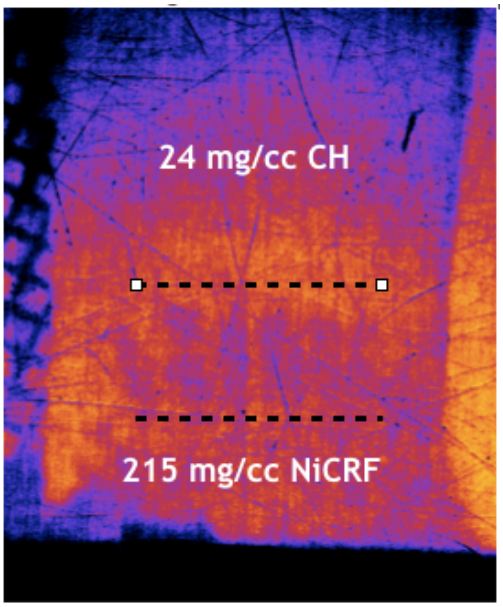

Figure 3.8: An X-ray radiograph of the LDNI foam from the Omega-EP experiment, where the target foam is designated as CH and the LDNI as NiCRF. The estimated RT instability growth is highlighted between the two black dashed lines.

ideal-MHD case where it consistently is 20 μm smaller than the HD RT instability growth, seen in Figure 3.11.

As a result of these simulations and the Omega-EP experiment for target development a subsequent NIF experimental campaign is designed. The transition to NIF would allow for a larger target with a larger perturbation, meaning the RT instability would be nonlinear sooner in its evolution, thus allowing more time for the seeded magnetic field to have an effect. The NIF is the largest laser in the world with higher laser driver power and subsequently hotter temperatures. This stands to increase the magnetic Reynolds number to a degree where the damping effects of seeded magnetic fields, also larger on NIF, could be observed in the resistive-MHD case.

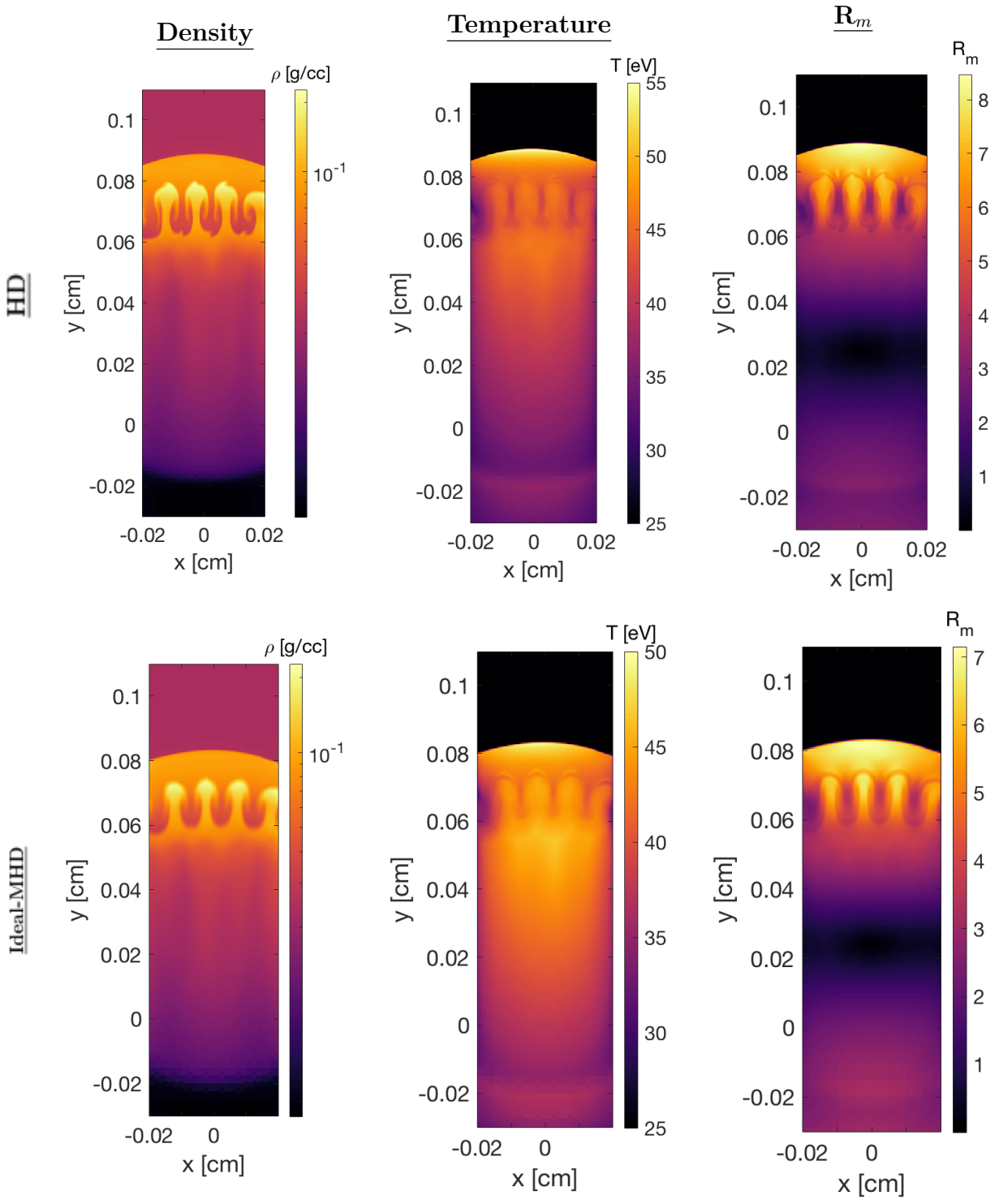

Figure 3.9: Density, temperature, and Magnetic Reynolds number of the benchmarked LDNI foam in HD and 12 T ideal-MHD at 7 ns, which is the time at which the x-ray radiograph is taken on Omega-Ep.

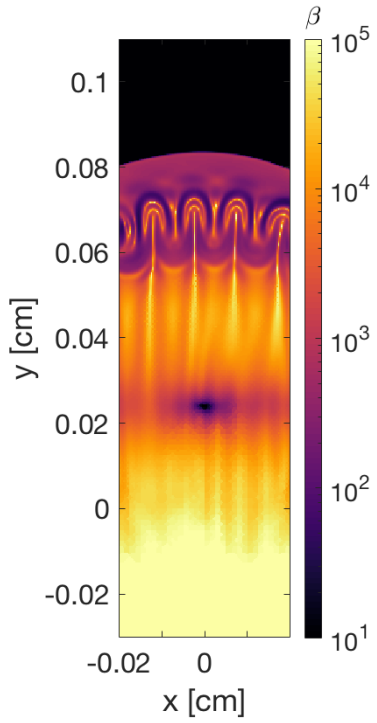

Figure 3.10: Plasma β plot of the benchmarked LDNI 12 T ideal-MHD at 7 ns, demonstrating the large β value indicative of the how the magnetic field would have little impact on the plasma.

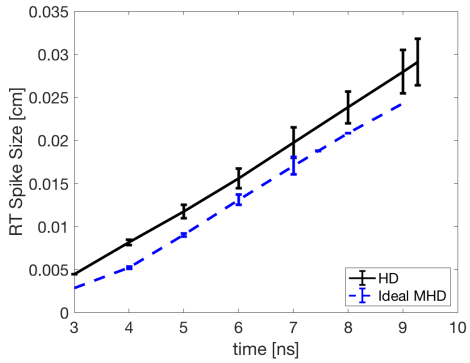

Figure 3.11: A measure of RT instability growth through the duration of the benchmarked LDNI HD(black line) and ideal-MHD(blue dashed line) cases.

3.3 Experimental Parameters for NIF

Given the results from the Omega-EP simulations, the subsequent experiment, and machining capabilities, the LDNI is selected as the best foam material to use going forward, with the same density of 215 mg/cm^3. The new target configuration for NIF consisted of a solid density, 1.0 g/cm^3, polystyrene ablator that is 30 μm thick, a 200 μm thick carbon foam of density 235 mg/cm^3, on which the 600 μm thick LDNI is positioned. Lastly, the low density target foam is 20 mg/cm^3. Due to this new configuration being built for experiments on NIF, the overall target package is built to be double sided, meaning a perturbation on the top and bottom that are driven together from either ends at slightly offset laser timings. This is

done in order to achieve two separate stages of growths of the same perturbation with the same X-ray radiograph. An example image of the overall NIF target package can be seen in Figure 3.12.

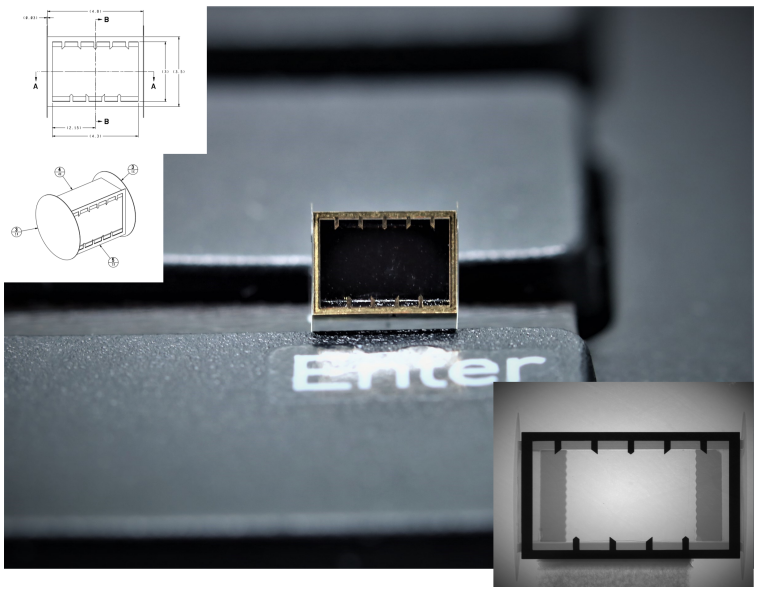

Figure 3.12: A general machining schematic, as well as baseline test of x-radiography, and a scaling image of the NIF physics package that is designed to measure deceleration stage RT instability growth.

The laser drive of this system is updated for the NIF consisting of a super Gaussian of 6.8, a Gaussian radius of 586 μm, a spot size of 1.3 mm and a laser intensity of 1.64×10^{15} W/cm^2 for a 3 ns pulse length. The perturbation has a wavelength of λ= 120 μm with an amplitude of 20 μm. The following simulations in HD, ideal-MHD, and resistive-MHD are run out until 16 ns, and the ideal-MHD and resistive-MHD cases are run with a seeded background magnetic field of 30 T. The results of these simulations are described in the following section.

3.4 Computational Results for NIF

The difference between HD and ideal-MHD is clear; however, unlike in a solid density cylindrical case the resistive-MHD scheme also presents a comparable difference to the RT instability growth in the HD case. This justifies the need for the computationally expensive resistive-MHD modeling of such a configuration. Figure 3.13, Figure 3.14, and Figure 3.15 show side-by-side comparisons of the three cases in density, temperature and magnetic Reynolds number at 13 ns into the implosion. The difference in RT instability morphology and growth is clearly distinguishable in Figure 3.13 between the ideal-MHD case and the HD case. Unlike the previously discussed Cartesian and cylindrical configurations, the resistive-MHD cases also presents a noticeable difference in the RT instability growth when compared to the HD and ideal-MHD case. The ideal-MHD case clearly depicts the most reduction in RT instability growth and the resistive-MHD case presents a quantifiable difference in RT instability growth when compared to the HD and ideal-MHD cases.

The temperature around the RT growth is on the order of 80 eV in HD, ideal-MHD, and resistive-MHD, and is consistent across all three cases, seen in Figure 3.14. Consequently, a magnetic Reynolds number of 40-50 is achieved in the HD and ideal-MHD verses 45-55 observed in resistive-MHD, seen in Figure 3.15. This strongly suggests that with sufficiently high temperatures and velocities, magnetic Reynolds numbers on the order of 50 can be achieved for experiments performed in this NIF-relevant parameter space. Based on these findings, resistive-MHD modeling will show noticeable differences and provide the equation system that most accurately represents the experimentally observable result. This measurable difference is demonstrated in the peak-to-valley measurements of the RT instability growth in Figure 3.16, where the divergence of the resistive-MHD growth, in the blue dotted line, from the HD growth, in the solid black, is possibly measurable in an experiment

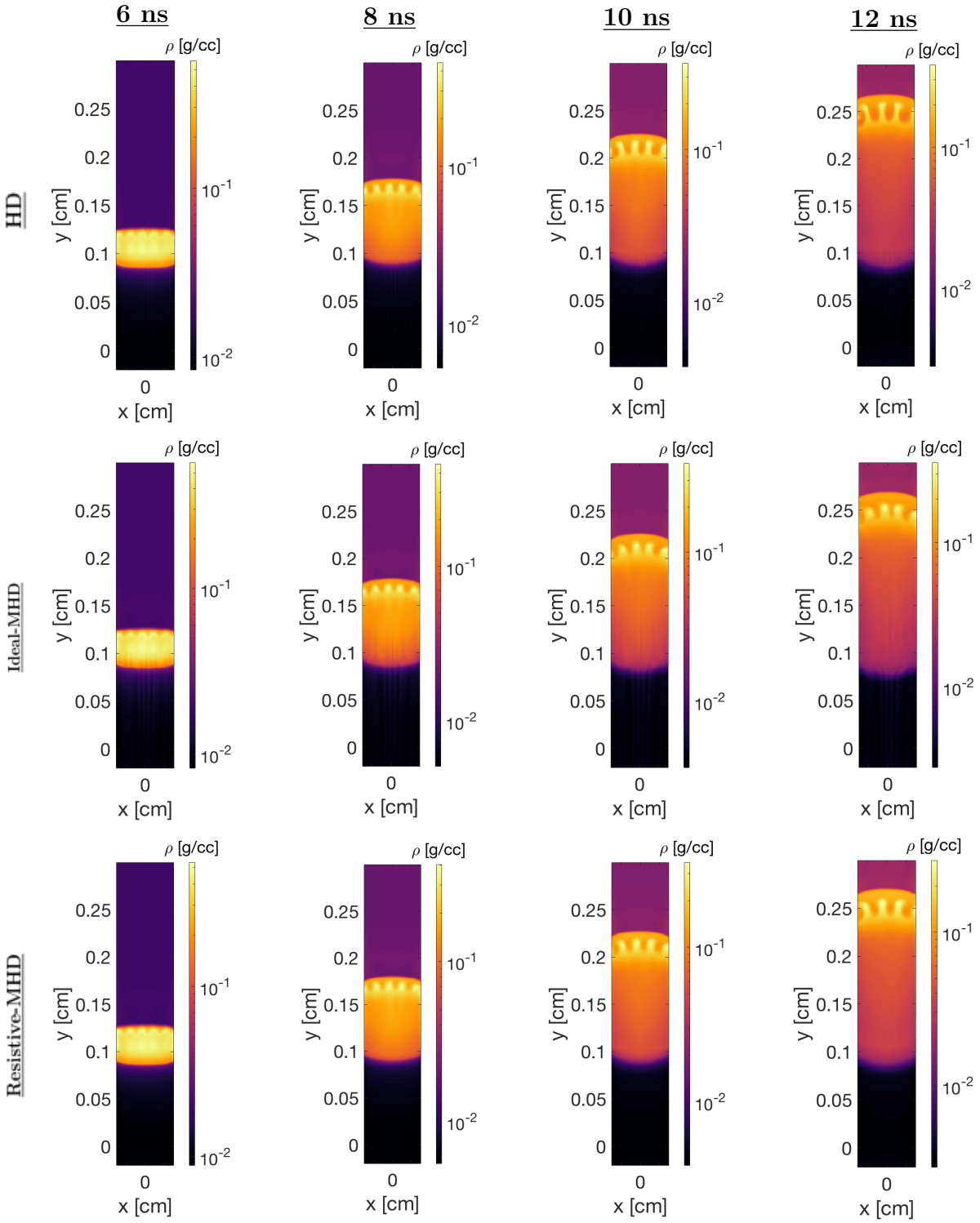

Figure 3.13: Density plots of RT instability growth at 6 ns, 8 ns, 10 ns, and 12 ns. This demonstrates the difference in RT growth and morphology during the course of the implosion.

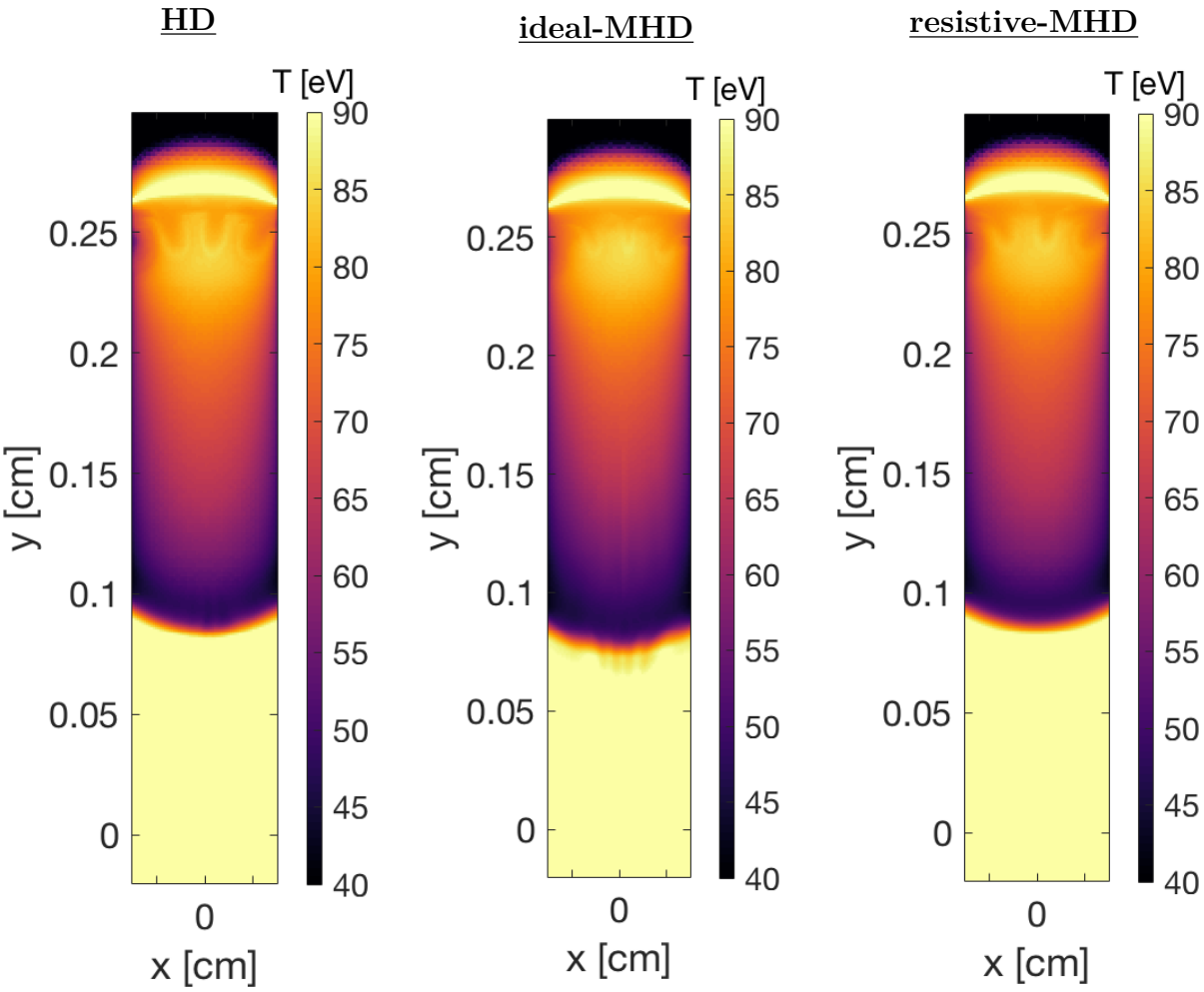

Figure 3.14: Temperature plots of RT instability growth during deceleration using Cartesian NIF experimental parameters, modeled in an HD, ideal-MHD and resistive-MHD, both with 30T background field, 13 ns into the implosion.

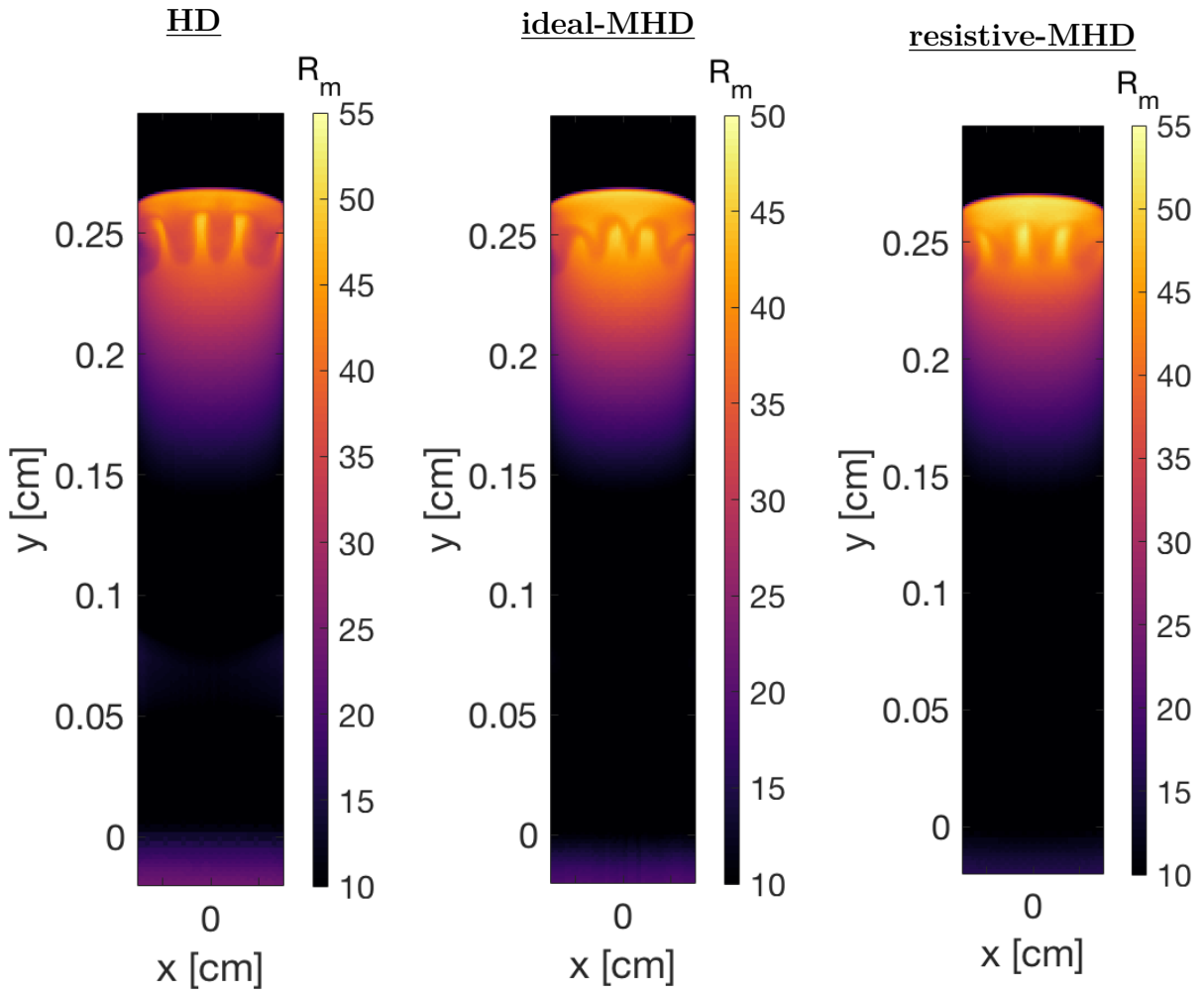

Figure 3.15: Magnetic Reynolds number plots of RT instability growth during deceleration using Cartesian NIF experimental parameters, modeled in an HD, ideal-MHD and resistive-MHD both with 30 T background field 13 ns into the implosion. The difference in RT spike height and morphology is distinguishable between simulation methods.

with present diagnostics. It trends towards convergence with the ideal-MHD RT instability growth seen in the blue dashed line.

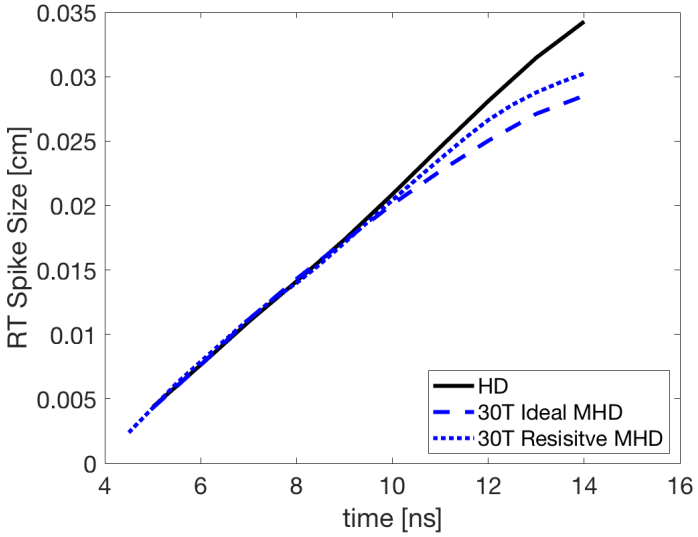

Figure 3.16: Measured growth of the Rayleigh-Taylor spike in HD, ideal MHD, and resistive MHD for a Cartesian NIF based experimental configurations. The HD RT growth is seen in black, while the 30 T ideal-MHD growth is the blue dashed line, and the 30 T resistive-MHD growth can be seen in the blue dotted line, a measurable difference in RT growth is notable after 10 ns.

Lastly, the plasma β in the ideal-MHD and resistive-MHD cases can be found in Figure 3.17. This shows that even in this high temperature, high velocity system that achieves a magnetic Reynolds number on the order of 50, the plasma β is still on the order of 10^3. Therefore, additional effects from terms in the extended-MHD equations, such as the Hall term, most likely will not play a significant role in impacting the RT instability growth. This is important to note given the diffusive effects of resistivity clearly damp the RT instability growth, and additional terms like Hall or Biermann battery could contribute to reduction of RT instability growth further under the right conditions.

The simulations presented demonstrate that without sufficient temperatures and magnetic Reynolds numbers being achieved in solid density HED configurations, ideal-MHD modeling

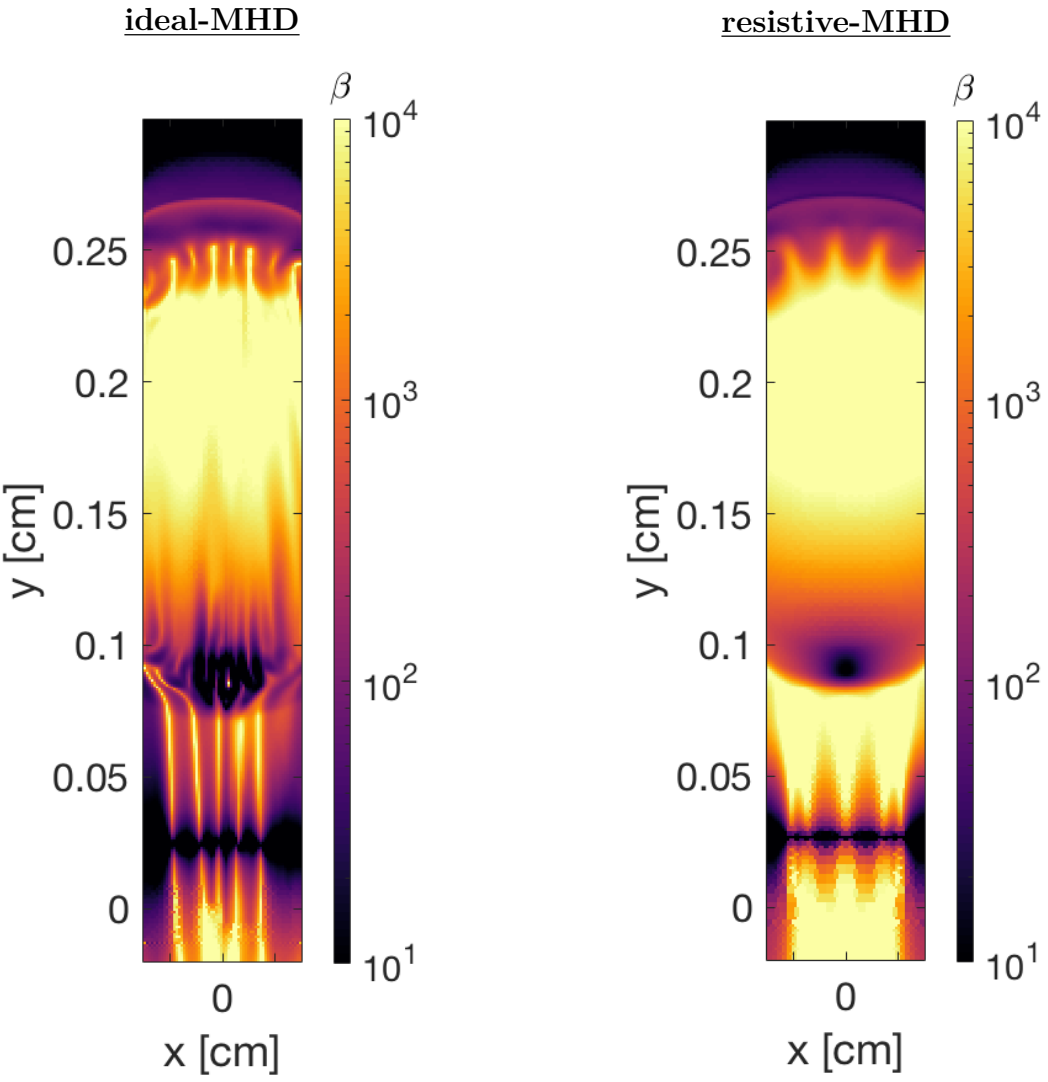

Figure 3.17: Plasma β plots of RT instability growth during deceleration using Cartesian NIF experimental parameters, modeled in ideal-MHD and resistive-MHD both with 30 T background field 13 ns into the implosion. The difference in RT spike height and morphology is distinguishable between simulation methods.

provides an overly optimistic inaccurate estimate of the effects of a seeded background magnetic fields on RT instability growth. Resistive-MHD is a computationally expensive model that does not achieve significant difference from the standard Eulerian HD model in these same solid density configurations. However, a transition to foam targets and higher laser driver powers found on the NIF, indicates a need to use resistive-MHD modeling in order to predict the mitigating impacts a background magnetic field will have on RT instability growth. Experiments validating such a measurable difference in RT growth are currently under way at the NIF.

Chapter 4

Thin-Layer Theory Rayleigh Taylor Growth

4.1 Single Feature Perturbations

Single-feature perturbations have been the topic of a recent resurgence of interest, particularly centered around the single-feature anomaly from the fill tube in ICF implosions. Several papers have illustrated the negative impacts of the presence of the fill-tube perturbation in ICF implosions, including Clark [8] and Hammel [4]. Recently, Weber et al. [7] showed that a surrogate perturbation, representing the fill tube, on the interior of a model ICF capsule produces comparable mixing and convergence reduction as a fully-modeled fill-tube feature. Figure 4.1 shows numerical results of the negative impacts caused by isolated, single-features, such as the fill tube and capsule tent, have on the implosion of an ICF capsule. Material mixing and convergence disruptions are observable in all fill tube configurations that have been modeled, including the recent reduced-size fill tube. Little exploration has been made into the potential mitigating effect of a background magnetic field on isolated, single-feature instability growth as Ott [9] described in the non-magnetized case. The following work will begin an exploration of using an isolated single-feature, in a magnetized, shock-tube platform for studying decelerating RT morphology in an experimental capacity.

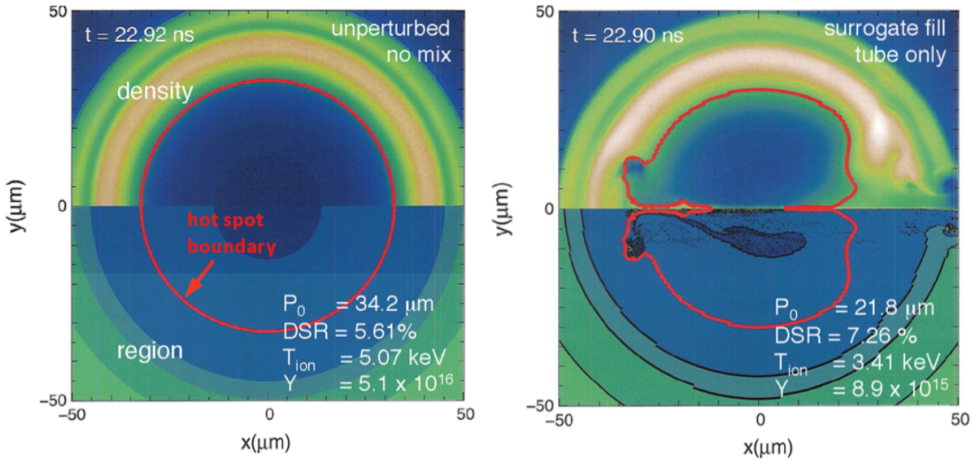

Figure 4.1: A reproduction figure from Clark et. al. [8] of density plot taken at bang time from 2D simulations of an ICF implosion. The isolated, surrogate fill tube feature is shown to cause a degradation in the ion temperature of 67% and a yield degradation of 17%.

4.2 Proposed Single Feature Experiment on Omega EP

Recent experiments on OMEGA EP have brought a level of clarity and understanding to the parameters that the proposed experimental design builds upon. The use of Ni-doped CRF-foam as a high-density pusher ($\sim$200 mg/cm^3) with a machined perturbation has been demonstrated and provides good absorption of $\sim$4.5 keV X-rays from a Ti back-lighter. By utilizing an unstable foam-foam interface in the target, as shown in Figure 4.2a, high magnetic Reynolds numbers ($\mathrm{Re}_m \gtrsim 40$) can be achieved during the instability growth. Short-pulse-driven X-ray radiography of a sinusoidal perturbation from the previous shot is used to benchmark the drive and timing in FLASH simulations for these foam-foam targets. However, short-pulse-driven background is too high; therefore, target alignment was an issue in studying detailed morphology. To mitigate these imaging and alignment issues, this proposed new platform design provides $\sim$1 degree perturbation alignment of the target and leverage the newly developed Fresnel Zone Plate (FZP) [3] [10] capability through a collaboration with Dr. Nilson at LLE. The FZP diagnostic is a new approach to imaging

using a zone plate and X-ray emissions from a backlighter.

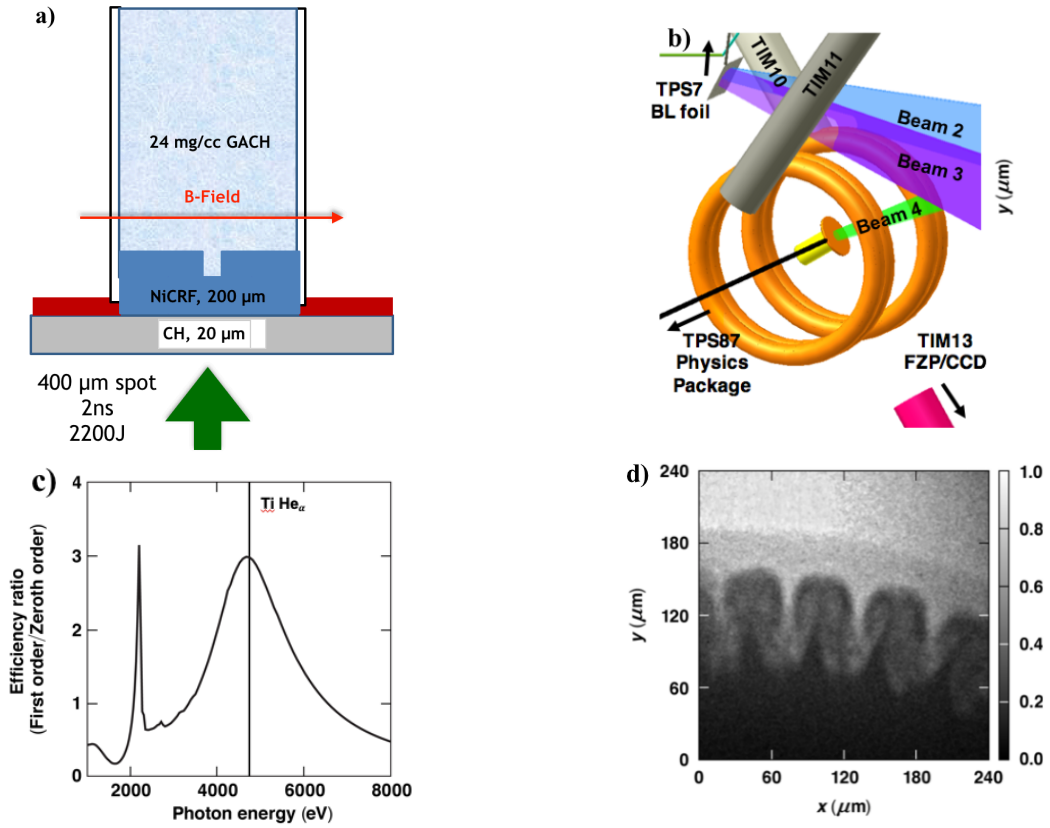

Figure 4.2: a) Target design for this proposal based on previously fabricated targets. b) Experimental setup utilizing 2 beams for the Ti back-lighter, and 1 beam to drive the physics package. Dual-MIFEDS provides a 25 T B-field. c) Efficiency ratio for a FZP with 467 zones, outer zone width of 107 nm, and Au zone thickness of 850nm. d) X-ray radiograph of RT evolution using these FZPs on Omega. [14].

The proposed experiment builds off prior Omega EP experiments, and is newly designed to study magnetic field effects on the nonlinear RT evolution of an isolated single-feature in accordance with the thin-layer RT analysis described by Ott [9]. The new design of this physics package consists of a fill-tube-adjacent isolated-feature of a 50 μm-wide divot set 100 μm into a 200 μm-thick Ni-CRF (C88Ni12) foam. The physics package is driven by one of Omega-EP's four beams, Beam 4, with a 2 ns square pulse containing 2200 J and implementing a 400 μm distributed phase plate (DPP), which creates a homogeneous intensity at the point of laser focus and providing an intensity of approximately 8×10^{14} W/cm^2. The

primary diagnostic is FZP-based X-ray radiography using a Ti He-α back-lighter and the FZP, described in Figure 4.2c, coupled to an X-ray CCD. The Ti area-back-lighter is driven by Beams 2 and 3, seen in Figure 4.2b, with 100 J/beam in 100 ps producing an intensity on the order of$\sim 4 \times 10^{14}$ W/cm^2. The imaging geometry places the FZP 84 mm from the physics package and 3.56 m from the X-ray CCD. This geometry has been shown to provide $\sim 3\,\mu$m spatial resolution of deceleration-phase RT instability, as shown in Figure 4.2d by RT growth of a sinusoidal perturbation on a solid-density pusher. The proposed work combines this diagnostic platform with dual-MIFEDS, the facility name for coils that provide a 25 T magnetic field, oriented perpendicular or parallel to the shock propagation direction, where the perpendicular configuration is shown in Figure 4.2b.

The experimental configuration calls for a 2 ns pulse of 2200 J of energy in a 400 μm spot, therefore the potential for hot electron generation is an issue that needs to be addressed. The generation of hot electrons occurs when the intensity of the laser on a small focal point heats electrons in the target material, this subsequently artificially heats the physics package before the implosion can propagate substantially inwards. The effect of electron preheat on the target is estimated by assuming 1% of the 2200 J is converted to hot electrons with a temperature of T_{hot}=50 keV, where higher T_{hot} tends to produce less preheat. The hot electron distribution is propagated through the target layers and energy deposition is calculated using estimated stopping powers [15]. The temperature differences are estimated by assuming nominal specific heats for each material and predicting a temperature increase of 1.1 eV, 1.5 eV, and 1.1 eV for the polystyrene ablator, Ni-CRF, and GACH foam, respectively. FLASH simulations using these initial temperatures are run to measure the difference between excluding and including the effect of the hot electron generation on the single-feature RT. Furthermore, tolerances are explored through simulations to ensure that the single-feature seeded RT growth is consistent across differently sized initial perturbations.

4.3 Estimated Single-Feature RT Growth

Utilizing the benchmarked FLASH deck, the experimental design is simulated and the estimated impact from the background magnetic field becomes observable. The RT growth for the isolated feature perturbation in a non-magnetized case as well as a 25 T ideal-MHD setup with the magnetic field oriented perpendicular and parallel to the divot are modeled. Figure 4.3 presents simulated X-ray radiographs of these cases. The simulated X-ray radiographs are created using the material opacity's converted to transmission and applying a Gaussian blur based on the group velocity to included the expected blur found in an experimental radiograph. Figure 4.3 shows that there is an significant plume growth from the single-feature perturbation, and as can be seen in the X-ray radiographs the presence and orientation of a externally applied magnetic field changes the plume growth and morphology. When the magnetic field is oriented perpendicular to the perturbation the RT instability growth is significantly reduced in size, and when oriented parallel the RT instability growth is has a kink and appears to be reduced in size to a lesser extent. This experimental configuration is well within the deceleration phase; the trajectory is parabolic with a deceleration of $\sim$8.5 μm/ns^2 and a nominal velocity of $\sim$20 μm/ns. Additionally, synthetic X-ray radiographs are created using the parameters pertaining to the proposed FZP and an asymmetric spatial Gaussian blur ($\sim$20 μm) is used to represent the temporal blur from the trajectory motion over 100 ps; this gives an underestimate of the expected contrast from the diagnostic. The estimated magnetic Reynolds number of the RT spike ranges from $>$50 to $\sim$30 during the RT growth suggesting that an ideal-MHD treatment is sufficient to describe the dynamics. Also, ideal-MHD simulations of these experiments predict that β $\sim$6 in the plasma surrounding the primary spike formation and within the RT instability growth itself, indicating the a high chance of seeing magnetic field mitigation on the growth.

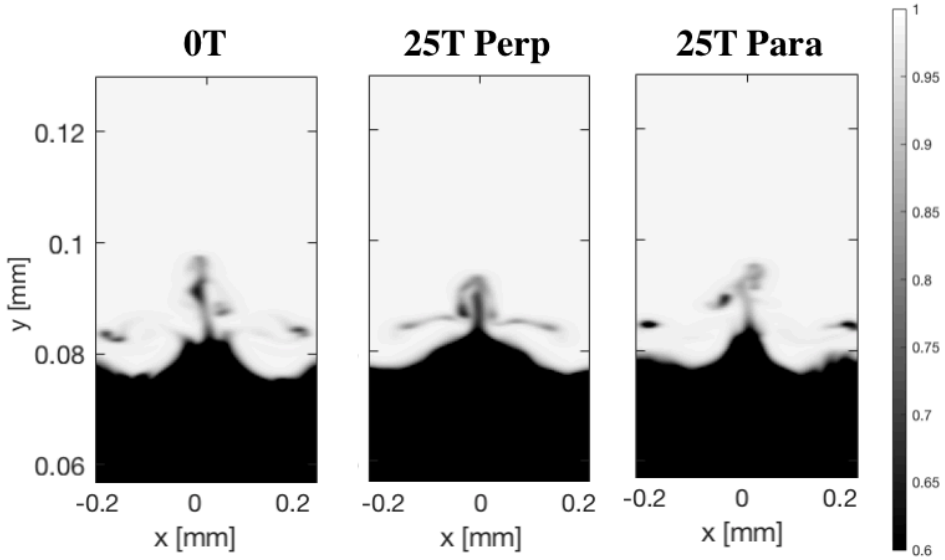

Figure 4.3: Simulated X-ray radiographs of the 50 μm by 100 μm divot isolated-feature experiment at 4.4 ns with B-fields of 0 T, 25 T perpendicular, and 25 T parallel cases. A y-skewed asymmetric spatial Gaussian blur is implemented to replicate the estimated temporal blur from the 100 ps temporal resolution.

A reduction in mix height from a single-feature perturbation is predicted when a 25 T B-field, oriented both parallel and perpendicular to shock propagation, is present, which is the direction of deceleration. Figure 4.4 illustrates these numerical results for the desired perturbation, 50 μm wide and 100 μm deep, as well as the two $\pm$20 μm tolerance cases. It is noted that a tolerance of +/- 20 μm can produce measurable differences in mix height of up to $\sim$50 to 100 μm. The physics package will be machined with tight tolerances ($\pm$5 μm) to ensure systematic consistency across multiple targets, as well as the individual metrology of all perturbations will be taken prior to the experiment. The final metrology will ensure accurate divot simulations can be run prior to the experiment.

FLASH simulations using the initial estimated pre-heat temperatures of 1.1 eV for the ablator, 1.5 eV for the NI-CRF, and 1.1 eV for the target foam, suggest the morphology of the spike differs slightly from the case without pre-heat, but still provides a measurable difference

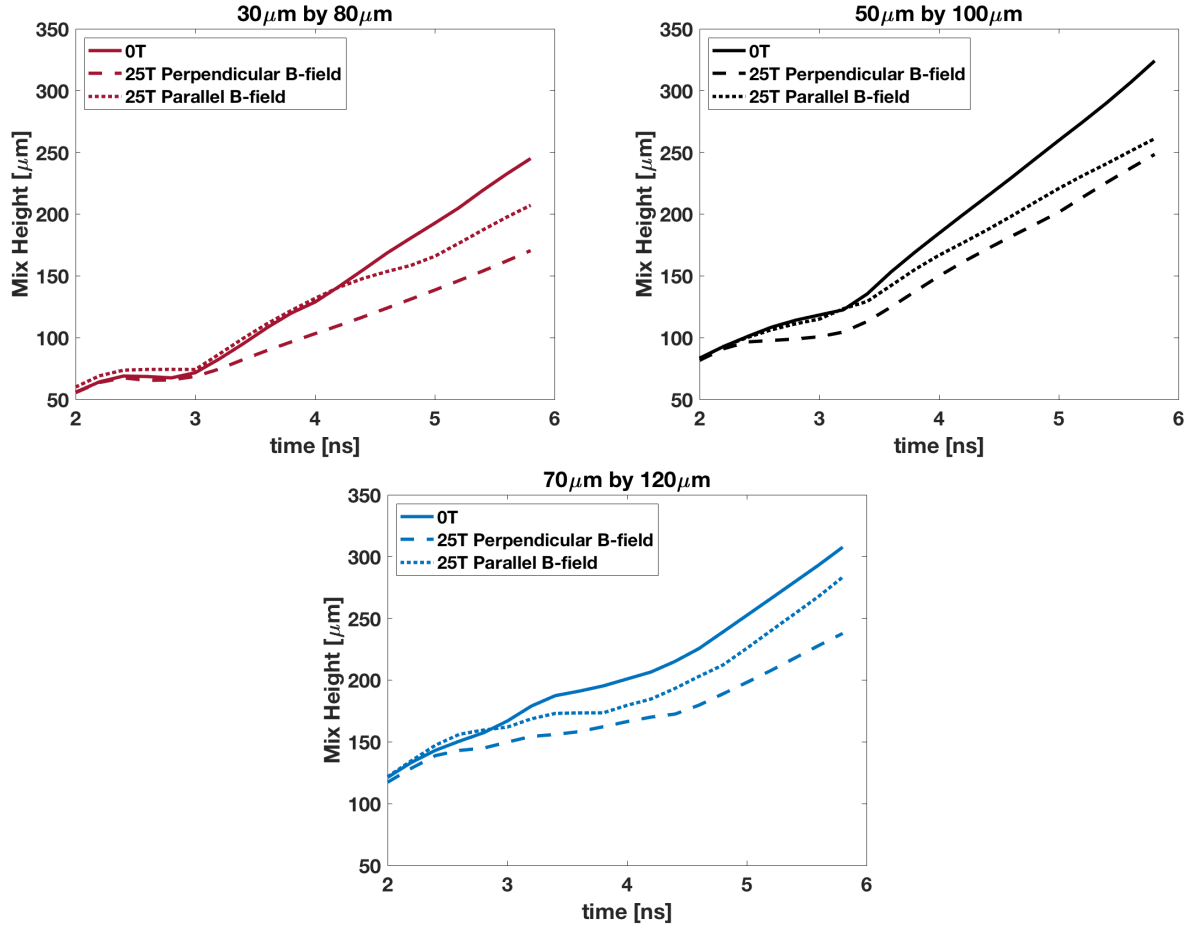

Figure 4.4: The mix height of three single-feature perturbations, described as "width" by "depth". The 50 μm by 100 μm divot is the nominal design proposed for this work. Numerical simulations show that deviations from nominal will still produce measurable differences from a 25 T B-field aligned perpendicular (dashed) and parallel (dotted) to shock propagation. This shows that a systematic shift from the nominal design during fabrication will still produce successful results.

in mix height between the 3 different cases: B=0 T, B=25 T perpendicular, and B=25 T parallel. Figure 4.5 illustrates the demonstrable change in morphology of the RT growth in the presence of the pre-heat, with the non-magnetized case developing an unexpected kink in the plume region, as well as a distinct reduction in mass in the plume region of the magnetized cases. This is characterized by the visible reduction in opacity. Furthermore, Figure 4.6 demonstrates that in the presence of the parallel 25 T B-field the mix-height is increased,

as opposed to the non-preheated cases where the non-magnetized configuration presents the largest mix-height. This is estimated to be an effect of the magnetic field lines being oriented in the same direction as the growth. The increase in mix height for the parallel 25 T magnetic field simulation with pre-heat compared to the 0 T magnetic field simulation with pre-heat is due to the RT instability experiencing a significant kinking for the pre-heated 0T case; however, this is unconfirmed and is a topic for future exploration. Yet despite these morphological differences, the magnetic Reynolds number sees little impact from the preheat and is consistently in the ∼30 to 50 range throughout the evolution.

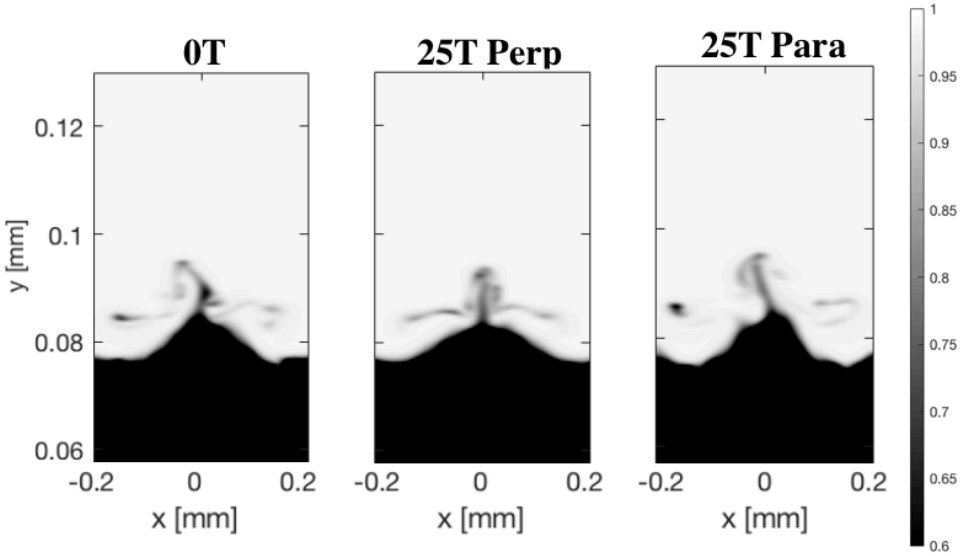

Figure 4.5: Simulated X-ray radiographs of the pre-heated 50 μm by 100 μm divot at 4.4 ns with B-fields of 0 T, 25 T perpendicular, and 25 T parallel cases. Again a y-skewed asymmetric spatial Gaussian blur is implemented to replicate the estimated temporal blur from the 100 ps temporal resolution of the FZP.

The high magnetic Reynolds numbers observed in both the pre-heated and non-heated configurations provide the means to amplify the seed magnetic field by ∼10x, thus supporting predictions from FLASH simulations of a reduction in nonlinear RT growth. The proposed experiment will aim to observe and measure the mitigating impact on the RT instability seeded from an isolated feature, thus providing supporting experimental evidence for numer-

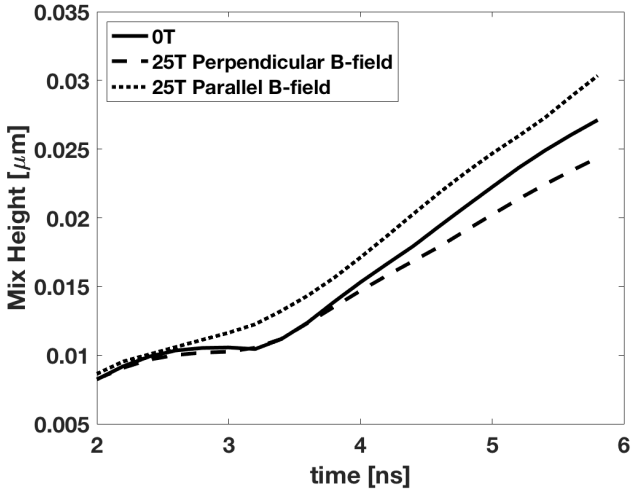

Figure 4.6: Mix-height of the RT instability growth in the proposed nominal 50 μm by 100 μm divot desgin with the applied pre-heat temperatures at the start of the simulation. Clearly there is the same predicted difference between the non magnetized, solid line, and perpendicular, dashed line as seen in the non pre-heat cases; however the parallel magnetized case demonstrates a distinctly larger RT instability growth than was seen in the non-heated cases previously described.

ical predictions presented in Srinivasan et al. [23] and Perkins et al. [16]. Moreover, this may present a new path forward to damp the negative impacts that fill tubes and isolated surface features may have on the convergence of ICF capsules.

Chapter 5

Conclusions

5.1 Conclusion and Future Work

The primary focus of this thesis is on the growth of the RT instability in the context of the deceleration stage of ICF relevant implosions, particularly the effect, or lack thereof, of a seeded magnetic field on the RT instability's growth during deceleration. Primarily a single mode is used to study the RT instability, and a multi-mode perturbation is explored in cylindrical coordinates. Preliminary studies of thin-layer-theory RT instability growth is also presented in Chapter 4, which explores how perturbations with wavelengths longer than the material is thick might develop RT instability growth. These RT instability configurations are studied using FLASH, solved first for the Euler equations and then extended to ideal-MHD in the presence of seed background magnetic fields of varying magnitudes and orientations. Finally, the addition of FLASH's Spitzer High Z resistivity model is added to several cases, extending the modeling to resistive-MHD regime. This introduces a diffusive effect, providing a more realistic representation of what would be observed in an experimental context.

Chapter 2 began with the validation of FLASH's HD code in comparison to Los Alamos National Laboratory's X-Rage Hydrodynamic code, and experimental data from the Omega laser. Additionally, it is demonstrated that transitioning from 1D to 2D in FLASH did not impact the shock dynamics, and neither did the extension of 2D FLASH HD to the ideal-

MHD or resistive-MHD scheme. The configurations run in the cylindrical coordinate system is a single mode and multi-mode solid density liner case driven with an 8 kJ laser. In both mode configurations the HD cases demonstrate notable RT instability growth on the interior interface during deceleration, and the addition of seed background magnetic fields 10 T, 25 T, and 50 T demonstrate a notable reduction in the RT instability growth in the ideal-MHD cases. However, in the presence of resistivity's diffusive effects, there is little observable impact on the RT instability growth regardless of the strength of the initial magnetic field. This is in part due to the low temperatures and subsequent magnetic Reynolds numbers that are reached during deceleration; therefore a similar configuration of the laser power and higher density would benefit little from the added effort of modeling in resistive-MHD when the HD system provides the same results with less computational cost.

Chapter 3 presents the platform development work for an on going blast-wave driven RT instability growth in Cartesian coordinates. Specifically, this work covers the exploration of shifting away from solid density targets to foam-foam targets, in which a higher density foam is driven by a laser pulse into a low density foam. These foam targets allow for higher Atwood numbers to be achieved, thus the RT instability is very nonlinear, and will experience the effects of a background magnetic field more quickly in its growth. Additionally, these foam targets are likely to reach higher temperatures, which can be seen even on the Omega laser parameter space, where in Figure 3.9 the temperatures achieved are on the order of 45 eV in the plasma around the RT instability growth. In the context of Omega, the magnetic Reynolds number did not reach 10, which is too small for the effects of a magnetic field to be observed on the RT instability growth. In the face of these low temperatures and magnetic Reynolds numbers, the campaign shifted to a NIF configuration in which a higher laser power and larger target are possible. In this configuration the damping effect of a 30 T magnetic field is observable within the RT instability growth for both the ideal-MHD

case and the resistive-MHD case. Temperatures on the order of 80-90 eV are observed and magnetic Reynolds numbers on the scale of 40-50 are seen in and around the RT instability growth. These results culminated in Figure 3.16, which demonstrates a measurable $\sim$500 μm difference in the RT instability spike growth. For configurations driven with sufficiently increased laser power to reach temperatures on the order of 80 eV and magnetic Reynolds numbers of 40, the use of resistive-MHD is imperative in accurately simulating the effect a magnetic field may have on the RT instability growth.

Finally, Chapter 4 describes the early steps in the exploration of thin-layer-theory RT instability growth. This is of particular relevance to ICF given the presence of single feature imperfections, or perturbations, such as fill-tubes in the ICF capsules. The potential for these types of perturbations to drive an RT instability growth during deceleration are simulated, and result in the presence of an extremely large and disruptive plume on the interior interface. This is consistent with the current research of the reduction in yield and increase in mix when a fill tube is modeled on an ICF capsule [7] [4] [8]. The addition of a 25 T background magnetic field is demonstrated to have a distinct damping effect on the mix-height of the growing RT instability even when the magnetic field is oriented perpendicular or parallel to the perturbation, seen in Figure 4.4. With the use of new diagnostics, the ability to resolve in great detail and measure the impact of such a experimental setup is greatly increased. Consequently, a preliminary experiment based on the simulations performed in this thesis has been developed, submitted to the National Laser Users' Facility (NLUF) proposal call, and is pending review.

Measuring the impact of background magnetic fields on the the growth of the RT instability is still being pursued in an experimental context to date. The NIF configuration described in Chapter 3 is scheduled to be shot on July 5th 2021, with the hope that the $\sim$500 μm RT instability growth height will be measurable in a non-magnetized and magnetized case.

Additionally, designing a foam NIF target for the cylindrical configuration is currently being explored. A cylindrical NIF target is based on a 4x scaling factor from Omega to NIF [19], from which the NIF power of 226 kJ is specifically incorporated, and is made up of a system that is comparable to the Cartesian configuration described. The cylindrical target for NIF will consist of a 30 μm solid density CH ablator, a 300 μm foam pusher made of nickel doped foam at 0.215 g/cm^3, and a target CH foam that is 20 g/cm^3 and 1.6 mm thick. A perturbation is added to the foam pusher target foam interface with a wavelength of 120 μm and an amplitude of 40 μm. This is being pursued in the hope that, as seen in the NIF scale Cartesian simulations, a measurable difference in the RT instability growth will be present in both the ideal-MHD and resistive-MHD cases. Lastly, the single-feature perturbation should be broadened to explore the impact of the perturbation size and shape, i.e. different types of fill tubes or single features found in ICF capsules. The potential for a magnetic field to impact RT instability growth seeded by such a perturbation would open a new avenue in which the reduction in mix and loss of fusion yield due to fill tubes could be explore and mitigated.

Bibliography

[1] *FLASH User's Guide*.

[2] Omega laser facility, 2021. URL https://www.lle.rochester.edu/index.php/omega-laser-facility-2/.

[3] Do A. et al. Two-channel high-resolution quasi-monochromatic x-ray imager for Al and Ti plasma. *Review of Scientific Instruments*, 89:113702, 2018.

[4] Hammel B.A. et al. High-mode Rayleigh-Taylor growth in NIF ignition capsules. *High Energy Density Physics*, 6:171–178, 2010.

[5] Shivamoggi B.K. Rayleigh-Taylor instability of a compressible plasma in a horizontal magnetic field. *Zeitschift fur Angewandte Mathematik und Physik (ZAMP)*, 33(5):693–697, 1982.

[6] F. F. Chen. *Introduction to Plasma Physics*. Springer, Switzerland, 2016. ISBN 978-3-319-22308-7.

[7] Weber C.R. et al. Mixing in ICF implosions on the Nation Ignition Facility caused by the fill-tube. *Physics of Plasmas*, 27:032703, 2020.

[8] Clark D.S. et al. Radiation hydrodynamics modeling of the highest compression inertial confinement fusion ignition experiment from the Nation Ignition Campaign. *Physics of Plasmas*, 22:022703, 2015.

[9] Ott E. Nonlinear evolution of the Rayleigh-Taylor instability of a thin layer. *Physical Review Letters*, 29(21):1429–1432, 1972.

[10] Marshall F.J. et al. High-resolution X-ray radiography with fresnel zone plates on the university of rochester's omega laser systems. *Review of Scientific Instruments*, 92: 033701, 2021.

[11] B. Fryxell, K. Olson, P. Ricker, F. X. Timmes, M. Zingale, D. Q. Lamb, P. MacNeice, R. Rosner, J. W. Truran, and H. Tufo. FLASH: An adaptive mesh hydrodynamics code for modeling astrophysical thermonuclear flashes. *The Astrophysical Journal Supplement Series*, 131(1):273–334, nov 2000. doi: 10.1086/317361. URL https://doi.org/10.1086/317361.

[12] Michael Gittings, Robert Weaver, Michael Clover, Thomas Betlach, Nelson Byrne, Robert Coker, Edward Dendy, Robert Hueckstaedt, Kim New, W Rob Oakes, Dale Ranta, and Ryan Stefan. The RAGE radiation-hydrodynamic code. *Computational Science & Discovery*, 1(1):015005, nov 2008. doi: 10.1088/1749-4699/1/1/015005. URL https://doi.org/10.1088/1749-4699/1/1/015005.

[13] M.L. Jun, B.I. Norman and J.M. Stone. A numerical study of Rayleigh-Taylor instability in magnetic fluids. *The Astrophysical Journal*, 453:332–349, 1995.

[14] Nilson P. Imaging of hydrodynamic perturbation evolution using a fresnel zone plate. DPP, 2020.

[15] Yaakoni P. et al. Fast-electron generation in long-scale-length plasmas. *Physics of Plasmas*, 19:012704, 2012.

[16] L.J Perkins et al. The potential of imposed magnetic fields for enhancing ignition probability and fusion energy yield in indirect-drive inertial confinement fusion. *Physics of plasmas*, 24(6):062708, 2017.

[17] S. Pfalzner. *An Introduction to inertial confinement fusion*. Taylor and Francis Group, LLC, Boca Raton, London and New York, 2009. ISBN 978-0-7503-0701-7.

[18] J. P. Sauppe, S. Palaniyappan, E. N. Loomis, J. L. Kline, K. A. Flippo, and B. Srinivasan. Using cylindrical implosions to investigate hydrodynamic instabilities in convergent geometry. *Matter and Radiation at Extremes*, 4(6):065403, 2019. doi: 10.1063/1.5090999. URL https://doi.org/10.1063/1.5090999.

[19] J. P. Sauppe, S. Palaniyappan, B. J. Tobias, J. L. Kline, K. A. Flippo, O. L. Landen, D. Shvarts, S. H. Batha, P. A. Bradley, E. N. Loomis, N. N. Vazirani, C. F. Kawaguchi, L. Kot, D. W. Schmidt, T. H. Day, A. B. Zylstra, and E. Malka. Demonstration of scale-invariant Rayleigh-Taylor instability growth in laser-driven cylindrical implosion experiments. *Phys. Rev. Lett.*, 124:185003, May 2020. doi: 10.1103/PhysRevLett.124.185003. URL https://link.aps.org/doi/10.1103/PhysRevLett.124.185003.

[20] Joshua Sauppe. Experimental and X-Rage data obtained through direct communication with Joshua Sauppe from Los Alamos National Laboratory.

[21] CE Seyler, Matthew R Martin, and ND Hamlin. Helical instability in MagLIF due to axial flux compression by low-density plasma. *Physics of Plasmas*, 25(6):062711, 2018.

[22] Lyman Spitzer. *Physics of fully ionized gases*. Interscience Publishers, New York, 1962. ISBN 978-0486449821.

[23] B. Srinivasan and Tang X.Z. The mitigating effect of magnetic fields on rayleigh-taylor unstable inertial confinement fusion plasmas. *Physics of plasmas*, 20(5):056307, 2013.

[24] B. Tobias, C.F. Kawaguchi, S. Palaniyappan, J.P. Sauppe, K.A. Flippo, and J.L. Kline. Bayesian inference of deceleration-phase Rayleigh-Taylor growth rates in laser-driven cylindrical implosions. *High Energy Density Physics*, 37:100879, 2020. ISSN 1574-1818.

doi: https://doi.org/10.1016/j.hedp.2020.100879. URL https://www.sciencedirect.com/science/article/pii/S1574181820301154.

[25] E.F. Toro, M. Spruce, and W. Speares. Restoration of the contact surface in the HLL-Riemann solver. *Shock Waves*, 4:25–34, 07 1994. doi: 10.1007/BF01414629.

[26] Bram van Leer. On the relation between the upwind-differencing schemes of godunov, engquist–osher and roe. *SIAM Journal on Scientific and Statistical Computing*, 5:1–20, 03 1984. doi: 10.1137/0905001.

[27] Bram van Leer. Upwind and high-resolution methods for compressible flow: From donor cell to residual-distribution schemes. *Communications in Computational Physics*, 1:192–206, 04 2006.

[28] Chang Y.P. et al. Fusion yield enhancement in magnetized laser-driven implosions. *Physical Review Letters*, 107:035006, 2011.

Appendices

Appendix A

First Appendix

A.1 Ideal-MHD FLASH par file

```
basenm = "NIF_1.6P_3ns_40mg_L120"
log_file = "NIF_1.6P_3ns_40mg_L120.log"
run_comment = "Simulation of Nasted Outflows Experiment"
#output_directory = "."

### Restart Options ###
restart = .false.
checkpointFileNumber = 0



#plotFileIntervalStep = 0
plotFileIntervalTime = 5.00000000e-10
plotFileNumber = 0

checkpointFileIntervalStep = 1000
checkpointFileIntervalTime = 1.0e-9
```

```
############################
#                          #
#     HYDRO PARAMETERS     #
#                          #
############################
useHydro = .true.

order = 2
prolMethod = "balsara_prol"
RiemannSolver = "hllc"
shockDetect = .true.
slopeLimiter = "mc"
eintSwitch = 1.00000000e-03
energyFix = .true.
entropy = .false.
use_flattening = .false.
use_hybridOrder = .true.
use_steepening = .false.
use_upwindTVD = .false.
ForceHydroLimit = .false.
LimitedSlopeBeta = 1.00000000e+00
charLimiting = .true.
cvisc = 1.00000000e-01
use_avisc = .true.
```

```
xl_boundary_type = "reflect"
xr_boundary_type = "reflect"
yl_boundary_type = "outflow"
yr_boundary_type = "outflow"
zl_boundary_type = "reflect"
zr_boundary_type = "reflect"

conserveAngField = .false.
conserveAngMom = .false.

############################
#                          #
#     MHD PARAMETERS       #
#                          #
############################

useMagneticResistivity = .false.
use_biermann = .false.
use_biermann1T = .false.
hy_biermannSource = .false.
killdivb = .true.
flux_correct = .true.
energyFix = .True.
UnitSystem = "CGS"

E_modification = .false.
```

```
############################
#                          #
#     TIME PARAMETERS      #
#                          #
############################

dt_diff_factor = 1.00000000e+00
dtinit = 5.00000000e-14
dtmax = 1.00000000e-09
dtmin = 1.00000000e-16
cfl = 3.00000000e-01
hx_dtFactor = 1.00000000e+100
nend = 10000000

tmax = 2.00000000e-08
tstep_change_factor = 1.05000000e+00

wall_clock_checkpoint = 3360
#wall_clock_time_limit = 345600

################################
#                              #
#     CONDUCTION PARAMETERS    #
#                              #
################################
```

```
useConductivity = .true.
useDiffuse = .true.
useDiffuseComputeDtMagnetic = .false.
useDiffuseComputeDtSpecies = .false.
useDiffuseComputeDtTherm = .false.
useDiffuseComputeDtVisc = .false.
addThermalFlux = .false.

diff_eleFlCoef = 6.00000000e-02
diff_eleFlMode = "fl_larsen"
diff_eleXlBoundaryType = "outflow"
diff_eleXrBoundaryType = "outflow"
diff_eleYlBoundaryType = "vacuum"
diff_eleYrBoundaryType = "outflow"
diff_eleZlBoundaryType = "outflow"
diff_eleZrBoundaryType = "outflow"
diff_thetaImplct = 1.00000000e+00
diff_useEleCond = .true.


#####################################
#                                   #
#     HEAT EXCHANGE PARAMETERS      #
#                                   #
#####################################
```

```
useHeatexchange = .true.

##########################
#                        #
#     EOS PARAMETERS     #
#                        #
##########################

eosMode = "dens_ie_gather"
eosModeInit = "dens_temp_gather"
eos_tolerance = 1.00000000e-05
eos_useLogTables = .false.
eos_maxNewton = 5000
eos_maxfactorup = 1.05000000e+00

eos_abltEosType = "eos_tab"
eos_abltSubType = "ionmix4"
eos_abltTableFile = "polystyrene-imx-eos-32g.cn4"

eos_vacuEosType = "eos_gam"

eos_chamEosType = "eos_gam"
#eos_chamSubType = "ionmix4"
#eos_chamTableFile = "xe-flashsvn-eos-1gr.cn4"
```

```
eos_foamEosType = "eos_tab"
eos_foamSubType = "ionmix4"
eos_foamTableFile = "polystyrene-imx-eos-32g.cn4"

eos_pushEosType = "eos_tab"
eos_pushSubType = "ionmix4"
eos_pushTableFile = "MarioC40.cn4"

eos_pertEosType = "eos_tab"
eos_pertSubType = "ionmix4"
eos_pertTableFile = "MarioC40.cn4"

eos_washEosType = "eos_tab"
eos_washSubType = "ionmix4"
eos_washTableFile = "polystyrene-imx-eos-32g.cn4"

smallt = 1.00000000e+00
smallx = 1.00000000e-99

irenorm = 1

############################
#                          #
#     MESH PARAMETERS      #
#                          #
############################
```

```
geometry = "cartesian"

xmax = 1.0000000e-01
xmin = -1.0000000e-01

ymax = 3.300000000e-01
ymin = -2.00000000e-02

nblockx = 4
nblocky = 7

refine_var_1 = "dens"
refine_var_2 = "tele"
refine_var_3 = "tion"
refine_var_4 = "pres"

lrefine_max = 7
lrefine_min = 1
lrefine_min_init = 7
meshCopyCount = 1


gr_pmrpCylindricalPm = .true.
gr_pmrpcurvilinearconserve = .true.
gr_pmrpdivergencefree = 1
```

```
gr_pmrpforceconsistency = .true.

##########################################
#                                        #
#     RADIATION/OPACITY PARAMETERS       #
#                                        #
##########################################

useOpacity = .true.
rt_useMGD = .true.

rt_dtFactor = 2.00000000e-02
rt_mgdBounds_1 = 1.00000000e+00
rt_mgdBounds_10 = 3.00000000e+02
rt_mgdBounds_11 = 3.25000000e+02
rt_mgdBounds_12 = 3.50000000e+02
rt_mgdBounds_13 = 3.75000000e+02
rt_mgdBounds_14 = 4.00000000e+02
rt_mgdBounds_15 = 5.00000000e+02
rt_mgdBounds_16 = 6.00000000e+02
rt_mgdBounds_17 = 7.00000000e+02
rt_mgdBounds_18 = 8.00000000e+02
rt_mgdBounds_19 = 9.00000000e+02
rt_mgdBounds_2 = 1.00000000e+01
rt_mgdBounds_20 = 1.00000000e+03
rt_mgdBounds_21 = 1.10000000e+03
```

```
rt_mgdBounds_22 = 1.20000000e+03
rt_mgdBounds_23 = 1.30000000e+03
rt_mgdBounds_24 = 1.40000000e+03
rt_mgdBounds_25 = 1.50000000e+03
rt_mgdBounds_26 = 2.00000000e+03
rt_mgdBounds_27 = 3.00000000e+03
rt_mgdBounds_28 = 4.00000000e+03
rt_mgdBounds_29 = 4.50000000e+03
rt_mgdBounds_3 = 2.00000000e+01
rt_mgdBounds_30 = 5.00000000e+03
rt_mgdBounds_31 = 5.10000000e+03
rt_mgdBounds_32 = 5.20000000e+03
rt_mgdBounds_33 = 5.30000000e+03
rt_mgdBounds_34 = 5.40000000e+03
rt_mgdBounds_35 = 5.50000000e+03
rt_mgdBounds_36 = 6.00000000e+03
rt_mgdBounds_37 = 7.00000000e+03
rt_mgdBounds_38 = 8.00000000e+03
rt_mgdBounds_39 = 1.10000000e+04
rt_mgdBounds_4 = 2.50000000e+01
rt_mgdBounds_40 = 1.50000000e+04
rt_mgdBounds_41 = 2.00000000e+04
rt_mgdBounds_5 = 3.50000000e+01
rt_mgdBounds_6 = 5.00000000e+01
rt_mgdBounds_7 = 1.00000000e+02
rt_mgdBounds_8 = 2.00000000e+02
```

```
rt_mgdBounds_9 = 2.50000000e+02
rt_mgdFlCoef = 1.00000000e+00
rt_mgdFlMode = "fl_harmonic"
rt_mgdNumGroups = 40
rt_mgdXlBoundaryType = "reflecting"
rt_mgdXrBoundaryType = "reflecting"
rt_mgdYlBoundaryType = "vacuum"
rt_mgdYrBoundaryType = "vacuum"
rt_mgdZlBoundaryType = "reflecting"
rt_mgdZrBoundaryType = "reflecting"



op_abltAbsorb = "op_tabpa"
op_abltEmiss = "op_tabpe"
op_abltFileName = "polystyrene-prp-40gr.cn4"
op_abltFileType = "ionmix4"
op_abltTrans = "op_tabro"

#op_chamAbsorb = "op_tabpa"
#op_chamEmiss = "op_tabpe"
#op_chamFileName = "Xe-prp-40gr.cn4"
#op_chamFileType = "ionmix4"
#op_chamTrans = "op_tabro"

op_chamAbsorb = "op_constant"
```

```
op_chamAbsorbConstant = 1.00000000e-05
op_chamEmiss = "op_constant"
op_chamEmissConstant = 1.00000000e-05
op_chamTrans = "op_constant"
op_chamTransConstant = 1.00000000e-05


op_foamAbsorb = "op_tabpa"
op_foamEmiss = "op_tabpe"
op_foamFileName = "polystyrene-prp-40gr.cn4"
op_foamFileType = "ionmix4"
op_foamTrans = "op_tabro"

op_obstAbsorb = "op_tabpa"
op_obstEmiss = "op_tabpe"
op_obstFileType = "ionmix4"
op_obstTrans = "op_tabro"

op_pushAbsorb = "op_tabpa"
op_pushEmiss = "op_tabpe"
op_pushFileName = "MarioC40.cn4"
op_pushFileType = "ionmix4"
op_pushTrans = "op_tabro"

op_pertAbsorb = "op_tabpa"
op_pertEmiss = "op_tabpe"
```

```
op_pertFileName = "MarioC40.cn4"
op_pertFileType = "ionmix4"
op_pertTrans = "op_tabro"

op_washAbsorb = "op_tabpa"
op_washEmiss = "op_tabpe"
op_washFileName = "polystyrene-prp-40gr.cn4"
op_washFileType = "ionmix4"
op_washTrans = "op_tabro"

op_shieAbsorb = "op_tabpa"
op_shieEmiss = "op_tabpe"
op_shieFileType = "ionmix4"
op_shieTrans = "op_tabro"

op_vacuAbsorb = "op_constant"
op_vacuAbsorbConstant = 1.00000000e-05
op_vacuEmiss = "op_constant"
op_vacuEmissConstant = 1.00000000e-05
op_vacuTrans = "op_constant"
op_vacuTransConstant = 1.00000000e-05




##############################
#                            #
```

```
#     INITIAL CONDITIONS     #
#                            #
##############################

### Ablator
sim_abltR = 1.250000000e-01
sim_abltThick = 3.00000000e-03

sim_conf_Foam = .true.
sim_decreaseMaxRefLvl1 = 2.00000000e-08
sim_externalMagx = 0.00000000e+00
sim_externalMagy = 0.00000000e+00
sim_fillCham = .false.
sim_foamThick = 3.50000000e-01
sim_gapThick = 0.00000000e+00



sim_plotFileIntervalTimeAt_1 = 0
sim_plotFileIntervalTimeAt_2 = 2.00000000e-09
sim_plotFileIntervalTimeAt_3 = 2.00000000e-08
sim_plotFileIntervalTimeAt_4 = 1.00000000e-07
sim_plotFileIntervalTimeVal_1 = 1.00000000e-10
sim_plotFileIntervalTimeVal_2 = 5.00000000e-10
sim_plotFileIntervalTimeVal_3 = 5.00000000e-10

### Pusher
```

```
sim_pushAmp = 2.00000000e-03
sim_pushPhase = 0.00000000e+00
sim_pushR = 1.250000000e-01
sim_pushThick = 2.00000000e-02
sim_pertR = 1.25000000e-01
sim_pertThick = 6.00000000e-02
sim_pushWL = 1.20000000e-02
sim_pertH = 6.000e-02

sim_rhoCham = 1.78400000e-03
sim_rhoablt = 1.00000000e+00
sim_rhocham = 5.20000000e-05
sim_rhofoam = 4.00000000e-02
sim_rhopush = 2.35000000e-01
sim_rhopert = 2.15000000e-01
sim_rhovacu = 1.00000000e-05
sim_rhowash = 1.04400000e+01

sim_teleVacu = 2.90113750e+02
sim_teleablt = 3.00000000e+02
sim_telecham = 3.00000000e+02
sim_telefoam = 3.00000000e+02
sim_telepush = 3.00000000e+02
sim_telepert = 3.00000000e+02
sim_televacu = 3.00000000e+02
sim_telewash = 3.00000000e+02
```

```
sim_tionVacu = 2.90113750e+02
sim_tionablt = 3.00000000e+02
sim_tioncham = 3.00000000e+02
sim_tionfoam = 3.00000000e+02
sim_tionpush = 3.00000000e+02
sim_tionpert = 3.00000000e+02
sim_tionvacu = 3.00000000e+02
sim_tionwash = 3.00000000e+02

sim_tradVacu = 2.90113750e+02
sim_tradablt = 3.00000000e+02
sim_tradcham = 3.00000000e+02
sim_tradfoam = 3.00000000e+02
sim_tradpush = 3.00000000e+02
sim_tradpert = 3.00000000e+02
sim_tradvacu = 3.00000000e+02
sim_tradwash = 3.00000000e+02

sim_washThick = 2.00000000e-03


ms_abltA = 6.50000000e+00
ms_abltZ = 3.50000000e+00
ms_abltZmin = 1.00000000e-01
```

```
ms_chamA = 1.31290000e+02
ms_chamZ = 54
ms_chamZmin = 1.00000000e-01

ms_foamA = 6.50000000e+00
ms_foamZ = 3.50000000e+00
ms_foamZmin = 1.00000000e-01

ms_pushA = 17.612624e+00
ms_pushZ = 8.6400000e+00
ms_pushZmin = 1.00000000e-01

ms_pertA = 17.612624e+00
ms_pertZ = 8.6400000e+00
ms_pertZmin = 1.00000000e-01

ms_targZMin = 1.00000000e-02

ms_vacuA = 1.00000000e+00
ms_vacuZ = 1.00000000e+00
ms_vacuZmin = 1.00000000e-01
ms_vacugamma = 1.15000000e+00

ms_washA = 6.50000000e+00
ms_washZ = 3.50000000e+00
ms_washZmin = 1.00000000e-01
```

```
##########################
#                        #
#     I/O PARAMETERS     #
#                        #
##########################


plot_var_1 = "dens"
plot_var_10 = "prad"
plot_var_11 = "pres"
plot_var_12 = "cond"
plot_var_13 = "gamc"
plot_var_14 = "game"
plot_var_15 = "eele"
plot_var_16 = "eion"
plot_var_17 = "erad"
plot_var_18 = "ener"
plot_var_19 = "velx"
plot_var_2 = "depo"
plot_var_20 = "vely"
plot_var_21 = "refc"
plot_var_22 = "ablt"
plot_var_23 = "push"
plot_var_24 = "foam"
```

```
plot_var_25 = "cham"
plot_var_26 = "vacu"
plot_var_27 = "wash"
plot_var_28 = "aref"
plot_var_29 = "bdry"
plot_var_3 = "tele"
plot_var_30 = "divb"
plot_var_31 = "magp"
plot_var_32 = "magx"
plot_var_33 = "magy"
plot_var_34 = "magz"
plot_var_35 = "mgdc"
plot_var_36 = "resi"
plot_var_37 = "r001"
plot_var_38 = "r002"
plot_var_39 = "r003"
plot_var_4 = "tion"
plot_var_40 = "r004"
plot_var_41 = "r005"
plot_var_42 = "r006"
plot_var_43 = "r007"
plot_var_44 = "r008"
plot_var_45 = "r009"
plot_var_46 = "r010"
plot_var_47 = "r011"
plot_var_48 = "r012"
```

```
plot_var_49 = "r013"
plot_var_5 = "trad"
plot_var_50 = "r014"
plot_var_51 = "r015"
plot_var_52 = "r016"
plot_var_53 = "r017"
plot_var_54 = "r018"
plot_var_55 = "r019"
plot_var_56 = "r020"
plot_var_57 = "r021"
plot_var_58 = "r022"
plot_var_59 = "r023"
plot_var_6 = "ye  "
plot_var_60 = "r024"
plot_var_61 = "r025"
plot_var_62 = "r026"
plot_var_63 = "r027"
plot_var_64 = "r028"
plot_var_65 = "r029"
plot_var_66 = "r030"
plot_var_67 = "r031"
plot_var_68 = "r032"
plot_var_69 = "r033"
plot_var_7 = "sumy"
plot_var_70 = "r034"
plot_var_71 = "r035"
```

```
plot_var_72 = "r036"
plot_var_73 = "r037"
plot_var_74 = "r038"
plot_var_75 = "r039"
plot_var_76 = "r040"
plot_var_77 = "pert"
plot_var_8 = "pele"
plot_var_9 = "pion"


#############################
#                           #
#     LASER PARAMETERS      #
#                           #
#############################

useEnergyDeposition = .true.

ed_adjustBeamsTargetIntensity = true

ed_pulseNumber_1 = 1
ed_computeGradNeleX = .true.
ed_computeGradNeleY = .true.
ed_crossSectionFunctionType_1 = "gaussian1D"
ed_gaussianExponent_1 = 3.4
ed_gaussianRadiusMajor_1 = 586.000000e-04
```

```
ed_gaussianRadiusMinor_1 = 586.000000e-04

ed_gradOrder = 2

ed_gridType_1 = "statistical1D"

ed_gridnRadialTics_1 = 687

ed_laser3Din2D = .false.

ed_laser3Din2DwedgeAngle = 1.00000000e-01

ed_laserIOMaxNumberOfPositions = 100000000

ed_laserIOMaxNumberOfRays = 128

ed_lensSemiAxisMajor_1 = 4.70000000e-02

ed_lensX_1 = 0.00000000e+00

ed_lensY_1 = -5.00000000e+02

ed_maxRayCount = 700000

ed_numberOfBeams = 1

ed_numberOfPulses = 1

ed_numberOfRays_1 = 600000

ed_numberOfSections_1 = 4

ed_useLaserIO = .false.

ed_wavelength_1 = 3.51000000e-01

ed_semiAxisMajorTorsionAngle_1 = 0.00000000e+00

ed_semiAxisMajorTorsionAxis_1 = "x"

ed_targetSemiAxisMajor_1 = 6.50000000e-02

ed_targetSemiAxisMinor_1 = 6.50000000e-02

ed_targetX_1 = 0.00000000e+00

ed_targetY_1 = 0.00000000e+00


#power
```

```
ed_power_1_1 = 0.0
ed_power_1_2 = 1.741448e+13
ed_power_1_3 = 1.741448e+13
ed_power_1_4 = 0.0

#Times
ed_time_1_1 = 0.00000000e+00
ed_time_1_2 = 0.1e-9
ed_time_1_3 = 2.9e-9
ed_time_1_4 = 3.0e-9
```

A.2 Resistive-MHD FLASH par file

```
basenm = "NIF_1.6P_3ns_40mg_L120"
log_file = "NIF_1.6P_3ns_40mg_L120.log"
run_comment = "Simulation of Nasted Outflows Experiment"
#output_directory = "."

### Restart Options ###
restart = .false.
checkpointFileNumber = 0



#plotFileIntervalStep = 0
plotFileIntervalTime = 5.00000000e-10
```

```
plotFileNumber = 0


checkpointFileIntervalStep = 1000
checkpointFileIntervalTime = 1.0e-9



##############################
#                            #
#     HYDRO PARAMETERS       #
#                            #
##############################
useHydro = .true.

order = 2
prolMethod = "balsara_prol"
RiemannSolver = "hllc"
shockDetect = .true.
slopeLimiter = "mc"
eintSwitch = 1.00000000e-03
energyFix = .true.
entropy = .false.
use_flattening = .false.
use_hybridOrder = .true.
use_steepening = .false.
use_upwindTVD = .false.
ForceHydroLimit = .false.
```

```
LimitedSlopeBeta = 1.00000000e+00
charLimiting = .true.
cvisc = 1.00000000e-01
use_avisc = .true.

xl_boundary_type = "reflect"
xr_boundary_type = "reflect"
yl_boundary_type = "outflow"
yr_boundary_type = "outflow"
zl_boundary_type = "reflect"
zr_boundary_type = "reflect"

conserveAngField = .false.
conserveAngMom = .false.

##############################
#                            #
#     MHD PARAMETERS         #
#                            #
##############################

useMagneticResistivity = .true.
use_biermann = .false.
use_biermann1T = .false.
hy_biermannSource = .false.
killdivb = .true.
```

```
flux_correct = .true.
energyFix = .True.
UnitSystem = "CGS"

E_modification = .false.

############################
#                          #
#     TIME PARAMETERS      #
#                          #
############################

dt_diff_factor = 0.3
dtinit = 5.00000000e-14
dtmax = 1.00000000e-09
dtmin = 1.00000000e-16
cfl = 3.00000000e-01
hx_dtFactor = 1.00000000e+100
nend = 10000000

tmax = 2.00000000e-08
tstep_change_factor = 1.05000000e+00

wall_clock_checkpoint = 3360

useSTS = .true.
```

```
nstepTotalSTS = 50
nuSTS = 0.001
useSTSforDiffusion = .true.
allowDtSTSDominate = .flase.

##################################
#                                #
#     CONDUCTION PARAMETERS      #
#                                #
##################################

useConductivity = .true.
useDiffuse = .true.
useDiffuseComputeDtMagnetic = .true.
useDiffuseComputeDtSpecies = .false.
useDiffuseComputeDtTherm = .false.
useDiffuseComputeDtVisc = .false.
addThermalFlux = .false.

diff_eleFlCoef = 6.00000000e-02
diff_eleFlMode = "fl_larsen"
diff_eleXlBoundaryType = "outflow"
diff_eleXrBoundaryType = "outflow"
diff_eleYlBoundaryType = "vacuum"
diff_eleYrBoundaryType = "outflow"
diff_eleZlBoundaryType = "outflow"
```

```
diff_eleZrBoundaryType = "outflow"
diff_thetaImplct = 1.00000000e+00
diff_useEleCond = .true.



####################################
#                                  #
#     HEAT EXCHANGE PARAMETERS     #
#                                  #
####################################

useHeatexchange = .true.

#########################
#                       #
#     EOS PARAMETERS    #
#                       #
#########################

eosMode = "dens_ie_gather"
eosModeInit = "dens_temp_gather"
eos_tolerance = 1.00000000e-05
eos_useLogTables = .false.
eos_maxNewton = 5000
eos_maxfactorup = 1.05000000e+00
```

```
eos_abltEosType = "eos_tab"
eos_abltSubType = "ionmix4"
eos_abltTableFile = "polystyrene-imx-eos-32g.cn4"

eos_vacuEosType = "eos_gam"

eos_chamEosType = "eos_gam"
#eos_chamSubType = "ionmix4"
#eos_chamTableFile = "xe-flashsvn-eos-1gr.cn4"

eos_foamEosType = "eos_tab"
eos_foamSubType = "ionmix4"
eos_foamTableFile = "polystyrene-imx-eos-32g.cn4"

eos_pushEosType = "eos_tab"
eos_pushSubType = "ionmix4"
eos_pushTableFile = "MarioC40.cn4"

eos_pertEosType = "eos_tab"
eos_pertSubType = "ionmix4"
eos_pertTableFile = "MarioC40.cn4"

eos_washEosType = "eos_tab"
eos_washSubType = "ionmix4"
eos_washTableFile = "polystyrene-imx-eos-32g.cn4"
```

```
smallt = 1.00000000e+00
smallx = 1.00000000e-99

irenorm = 1

############################
#                          #
#     MESH PARAMETERS      #
#                          #
############################

geometry = "cartesian"

xmax = 1.0000000e-01
xmin = -1.0000000e-01

ymax = 3.300000000e-01
ymin = -2.00000000e-02

nblockx = 4
nblocky = 7

refine_var_1 = "dens"
refine_var_2 = "tele"
refine_var_3 = "tion"
refine_var_4 = "pres"
```

```
lrefine_max = 7
lrefine_min = 1
lrefine_min_init = 7
meshCopyCount = 1


gr_pmrpCylindricalPm = .true.
gr_pmrpcurvilinearconserve = .true.
gr_pmrpdivergencefree = 1
gr_pmrpforceconsistency = .true.

########################################
#                                      #
#     RADIATION/OPACITY PARAMETERS     #
#                                      #
########################################

useOpacity = .true.
rt_useMGD = .true.

rt_dtFactor = 2.00000000e-02
rt_mgdBounds_1 = 1.00000000e+00
rt_mgdBounds_10 = 3.00000000e+02
rt_mgdBounds_11 = 3.25000000e+02
rt_mgdBounds_12 = 3.50000000e+02
```

```
rt_mgdBounds_13 = 3.75000000e+02
rt_mgdBounds_14 = 4.00000000e+02
rt_mgdBounds_15 = 5.00000000e+02
rt_mgdBounds_16 = 6.00000000e+02
rt_mgdBounds_17 = 7.00000000e+02
rt_mgdBounds_18 = 8.00000000e+02
rt_mgdBounds_19 = 9.00000000e+02
rt_mgdBounds_2 = 1.00000000e+01
rt_mgdBounds_20 = 1.00000000e+03
rt_mgdBounds_21 = 1.10000000e+03
rt_mgdBounds_22 = 1.20000000e+03
rt_mgdBounds_23 = 1.30000000e+03
rt_mgdBounds_24 = 1.40000000e+03
rt_mgdBounds_25 = 1.50000000e+03
rt_mgdBounds_26 = 2.00000000e+03
rt_mgdBounds_27 = 3.00000000e+03
rt_mgdBounds_28 = 4.00000000e+03
rt_mgdBounds_29 = 4.50000000e+03
rt_mgdBounds_3 = 2.00000000e+01
rt_mgdBounds_30 = 5.00000000e+03
rt_mgdBounds_31 = 5.10000000e+03
rt_mgdBounds_32 = 5.20000000e+03
rt_mgdBounds_33 = 5.30000000e+03
rt_mgdBounds_34 = 5.40000000e+03
rt_mgdBounds_35 = 5.50000000e+03
rt_mgdBounds_36 = 6.00000000e+03
```

```
rt_mgdBounds_37 = 7.00000000e+03
rt_mgdBounds_38 = 8.00000000e+03
rt_mgdBounds_39 = 1.10000000e+04
rt_mgdBounds_4 = 2.50000000e+01
rt_mgdBounds_40 = 1.50000000e+04
rt_mgdBounds_41 = 2.00000000e+04
rt_mgdBounds_5 = 3.50000000e+01
rt_mgdBounds_6 = 5.00000000e+01
rt_mgdBounds_7 = 1.00000000e+02
rt_mgdBounds_8 = 2.00000000e+02
rt_mgdBounds_9 = 2.50000000e+02
rt_mgdFlCoef = 1.00000000e+00
rt_mgdFlMode = "fl_harmonic"
rt_mgdNumGroups = 40
rt_mgdXlBoundaryType = "reflecting"
rt_mgdXrBoundaryType = "reflecting"
rt_mgdYlBoundaryType = "vacuum"
rt_mgdYrBoundaryType = "vacuum"
rt_mgdZlBoundaryType = "reflecting"
rt_mgdZrBoundaryType = "reflecting"



op_abltAbsorb = "op_tabpa"
op_abltEmiss = "op_tabpe"
op_abltFileName = "polystyrene-prp-40gr.cn4"
```

```
op_abltFileType = "ionmix4"
op_abltTrans = "op_tabro"

#op_chamAbsorb = "op_tabpa"
#op_chamEmiss = "op_tabpe"
#op_chamFileName = "Xe-prp-40gr.cn4"
#op_chamFileType = "ionmix4"
#op_chamTrans = "op_tabro"

op_chamAbsorb = "op_constant"
op_chamAbsorbConstant = 1.00000000e-05
op_chamEmiss = "op_constant"
op_chamEmissConstant = 1.00000000e-05
op_chamTrans = "op_constant"
op_chamTransConstant = 1.00000000e-05



op_foamAbsorb = "op_tabpa"
op_foamEmiss = "op_tabpe"
op_foamFileName = "polystyrene-prp-40gr.cn4"
op_foamFileType = "ionmix4"
op_foamTrans = "op_tabro"

op_obstAbsorb = "op_tabpa"
op_obstEmiss = "op_tabpe"
op_obstFileType = "ionmix4"
```

```
op_obstTrans = "op_tabro"


op_pushAbsorb = "op_tabpa"
op_pushEmiss = "op_tabpe"
op_pushFileName = "MarioC40.cn4"
op_pushFileType = "ionmix4"
op_pushTrans = "op_tabro"


op_pertAbsorb = "op_tabpa"
op_pertEmiss = "op_tabpe"
op_pertFileName = "MarioC40.cn4"
op_pertFileType = "ionmix4"
op_pertTrans = "op_tabro"


op_washAbsorb = "op_tabpa"
op_washEmiss = "op_tabpe"
op_washFileName = "polystyrene-prp-40gr.cn4"
op_washFileType = "ionmix4"
op_washTrans = "op_tabro"


op_shieAbsorb = "op_tabpa"
op_shieEmiss = "op_tabpe"
op_shieFileType = "ionmix4"
op_shieTrans = "op_tabro"


op_vacuAbsorb = "op_constant"
```

```
op_vacuAbsorbConstant = 1.00000000e-05
op_vacuEmiss = "op_constant"
op_vacuEmissConstant = 1.00000000e-05
op_vacuTrans = "op_constant"
op_vacuTransConstant = 1.00000000e-05



################################
#                              #
#     INITIAL CONDITIONS       #
#                              #
################################

### Ablator
sim_abltR = 1.250000000e-01
sim_abltThick = 3.00000000e-03

sim_conf_Foam = .true.
sim_decreaseMaxRefLvl1 = 2.00000000e-08
sim_externalMagx = 30.00000000e+04
sim_externalMagy = 0.00000000e+00
sim_fillCham = .false.
sim_foamThick = 3.50000000e-01
sim_gapThick = 0.00000000e+00
```

```
sim_plotFileIntervalTimeAt_1 = 0
sim_plotFileIntervalTimeAt_2 = 2.00000000e-09
sim_plotFileIntervalTimeAt_3 = 2.00000000e-08
sim_plotFileIntervalTimeAt_4 = 1.00000000e-07
sim_plotFileIntervalTimeVal_1 = 1.00000000e-10
sim_plotFileIntervalTimeVal_2 = 5.00000000e-10
sim_plotFileIntervalTimeVal_3 = 5.00000000e-10

### Pusher
sim_pushAmp = 2.00000000e-03
sim_pushPhase = 0.00000000e+00
sim_pushR = 1.250000000e-01
sim_pushThick = 2.00000000e-02
sim_pertR = 1.25000000e-01
sim_pertThick = 6.00000000e-02
sim_pushWL = 1.20000000e-02
sim_pertH = 6.000e-02

sim_rhoCham = 1.78400000e-03
sim_rhoablt = 1.00000000e+00
sim_rhocham = 5.20000000e-05
sim_rhofoam = 4.00000000e-02
sim_rhopush = 2.35000000e-01
sim_rhopert = 2.15000000e-01
sim_rhovacu = 1.00000000e-05
```

```
sim_rhowash = 1.04400000e+01

sim_teleVacu = 2.90113750e+02
sim_teleablt = 3.00000000e+02
sim_telecham = 3.00000000e+02
sim_telefoam = 3.00000000e+02
sim_telepush = 3.00000000e+02
sim_telepert = 3.00000000e+02
sim_televacu = 3.00000000e+02
sim_telewash = 3.00000000e+02

sim_tionVacu = 2.90113750e+02
sim_tionablt = 3.00000000e+02
sim_tioncham = 3.00000000e+02
sim_tionfoam = 3.00000000e+02
sim_tionpush = 3.00000000e+02
sim_tionpert = 3.00000000e+02
sim_tionvacu = 3.00000000e+02
sim_tionwash = 3.00000000e+02

sim_tradVacu = 2.90113750e+02
sim_tradablt = 3.00000000e+02
sim_tradcham = 3.00000000e+02
sim_tradfoam = 3.00000000e+02
sim_tradpush = 3.00000000e+02
sim_tradpert = 3.00000000e+02
```

```
sim_tradvacu = 3.00000000e+02
sim_tradwash = 3.00000000e+02

sim_washThick = 2.00000000e-03



ms_abltA = 6.50000000e+00
ms_abltZ = 3.50000000e+00
ms_abltZmin = 1.00000000e-01

ms_chamA = 1.31290000e+02
ms_chamZ = 54
ms_chamZmin = 1.00000000e-01

ms_foamA = 6.50000000e+00
ms_foamZ = 3.50000000e+00
ms_foamZmin = 1.00000000e-01

ms_pushA = 17.612624e+00
ms_pushZ = 8.6400000e+00
ms_pushZmin = 1.00000000e-01

ms_pertA = 17.612624e+00
ms_pertZ = 8.6400000e+00
ms_pertZmin = 1.00000000e-01
```

```
ms_targZMin = 1.00000000e-02

ms_vacuA = 1.00000000e+00
ms_vacuZ = 1.00000000e+00
ms_vacuZmin = 1.00000000e-01
ms_vacugamma = 1.15000000e+00

ms_washA = 6.50000000e+00
ms_washZ = 3.50000000e+00
ms_washZmin = 1.00000000e-01


##########################
#                        #
#     I/O PARAMETERS     #
#                        #
##########################


plot_var_1 = "dens"
plot_var_10 = "prad"
plot_var_11 = "pres"
plot_var_12 = "cond"
plot_var_13 = "gamc"
plot_var_14 = "game"
plot_var_15 = "eele"
```

```
plot_var_16 = "eion"
plot_var_17 = "erad"
plot_var_18 = "ener"
plot_var_19 = "velx"
plot_var_2 = "depo"
plot_var_20 = "vely"
plot_var_21 = "refc"
plot_var_22 = "ablt"
plot_var_23 = "push"
plot_var_24 = "foam"
plot_var_25 = "cham"
plot_var_26 = "vacu"
plot_var_27 = "wash"
plot_var_28 = "aref"
plot_var_29 = "bdry"
plot_var_3 = "tele"
plot_var_30 = "divb"
plot_var_31 = "magp"
plot_var_32 = "magx"
plot_var_33 = "magy"
plot_var_34 = "magz"
plot_var_35 = "mgdc"
plot_var_36 = "resi"
plot_var_37 = "r001"
plot_var_38 = "r002"
plot_var_39 = "r003"
```

```
plot_var_4 = "tion"
plot_var_40 = "r004"
plot_var_41 = "r005"
plot_var_42 = "r006"
plot_var_43 = "r007"
plot_var_44 = "r008"
plot_var_45 = "r009"
plot_var_46 = "r010"
plot_var_47 = "r011"
plot_var_48 = "r012"
plot_var_49 = "r013"
plot_var_5 = "trad"
plot_var_50 = "r014"
plot_var_51 = "r015"
plot_var_52 = "r016"
plot_var_53 = "r017"
plot_var_54 = "r018"
plot_var_55 = "r019"
plot_var_56 = "r020"
plot_var_57 = "r021"
plot_var_58 = "r022"
plot_var_59 = "r023"
plot_var_6 = "ye  "
plot_var_60 = "r024"
plot_var_61 = "r025"
plot_var_62 = "r026"
```

```
plot_var_63 = "r027"
plot_var_64 = "r028"
plot_var_65 = "r029"
plot_var_66 = "r030"
plot_var_67 = "r031"
plot_var_68 = "r032"
plot_var_69 = "r033"
plot_var_7 = "sumy"
plot_var_70 = "r034"
plot_var_71 = "r035"
plot_var_72 = "r036"
plot_var_73 = "r037"
plot_var_74 = "r038"
plot_var_75 = "r039"
plot_var_76 = "r040"
plot_var_77 = "pert"
plot_var_8 = "pele"
plot_var_9 = "pion"



##############################
#                            #
#     LASER PARAMETERS       #
#                            #
##############################
```

```
useEnergyDeposition = .true.


ed_adjustBeamsTargetIntensity = true


ed_pulseNumber_1 = 1
ed_computeGradNeleX = .true.
ed_computeGradNeleY = .true.
ed_crossSectionFunctionType_1 = "gaussian1D"
ed_gaussianExponent_1 = 3.4
ed_gaussianRadiusMajor_1 = 586.000000e-04
ed_gaussianRadiusMinor_1 = 586.000000e-04
ed_gradOrder = 2
ed_gridType_1 = "statistical1D"
ed_gridnRadialTics_1 = 687
ed_laser3Din2D = .false.
ed_laser3Din2DwedgeAngle = 1.00000000e-01
ed_laserIOMaxNumberOfPositions = 100000000
ed_laserIOMaxNumberOfRays = 128
ed_lensSemiAxisMajor_1 = 4.70000000e-02
ed_lensX_1 = 0.00000000e+00
ed_lensY_1 = -5.00000000e+02
ed_maxRayCount = 700000
ed_numberOfBeams = 1
ed_numberOfPulses = 1
ed_numberOfRays_1 = 600000
ed_numberOfSections_1 = 4
```

```
ed_useLaserIO = .false.
ed_wavelength_1 = 3.51000000e-01
ed_semiAxisMajorTorsionAngle_1 = 0.00000000e+00
ed_semiAxisMajorTorsionAxis_1 = "x"
ed_targetSemiAxisMajor_1 = 6.50000000e-02
ed_targetSemiAxisMinor_1 = 6.50000000e-02
ed_targetX_1 = 0.00000000e+00
ed_targetY_1 = 0.00000000e+00

#power
ed_power_1_1 = 0.0
ed_power_1_2 = 1.741448e+13
ed_power_1_3 = 1.741448e+13
ed_power_1_4 = 0.0

#Times
ed_time_1_1 = 0.00000000e+00
ed_time_1_2 = 0.1e-9
ed_time_1_3 = 2.9e-9
ed_time_1_4 = 3.0e-9
```